Laser-Induced Modulation, Vaporization, and Plasma Formation of Free-Flying Liquid Tin Sheets

Hermann Karl Schubert

Ph.D. thesis, Vrije Universiteit Amsterdam, 2025
Laser-Induced Modulation, Vaporization, and Plasma Formation of Free-Flying Liquid Tin Sheets
Hermann Karl Schubert

Printing: Ridderprint | www.ridderprint.nl.
ISBN: 978-94-6522-908-9

An electronic version of this dissertation is available at: `research.vu.nl`

VRIJE UNIVERSITEIT

Laser-Induced Modulation, Vaporization, and Plasma Formation of Free-Flying Liquid Tin Sheets

ACADEMISCH PROEFSCHRIFT

ter verkrijging van de graad van Doctor of Philosophy
aan de Vrije Universiteit Amsterdam,
op gezag van de rector magnificus
prof.dr. J.J.G. Geurts,
volgens besluit van de decaan
van de Faculteit der Bètawetenschappen
in het openbaar te verdedigen
op dinsdag 9 december 2025 om 11.45 uur
in de universiteit

door

Hermann Karl Schubert

geboren te Dresden, Duitsland

promotor: prof.dr. O. O. Versolato
copromotoren: prof.dr. W.M.G. Ubachs
dr. J. Sheil

promotiecommissie: prof.dr. H.L. Bethlem
prof.dr.ir. U. Ebert
prof.dr. G. O'Sullivan
prof.dr. A.A. Darhuber
dr. M. Jalaal

The work described in this thesis was conducted at the Advanced Research Center for Nanolithography (ARCNL), a public-private partnership between, the Vrije Universiteit Amsterdam (VU), Rijksuniversiteit Groningen (UG), the Dutch Research Council (NWO), the University of Amsterdam (UvA), and the semiconductor equipment manufacturer ASML.

Contents

List of Symbols & Abbreviations

CE	**C**onversion **E**fficiency *of laser light into EUV light (*2 % *bandwidth around* 13.5 nm*)*
EUV	**E**xtreme-**u**ltra**v**iolet light λ =13.5 nm, E =91.84 eV
PP	**P**re**p**ulse
VP	**V**aporization **p**ulse
MP	**M**ain **p**ulse
SP	**S**hadowgraphy **p**ulse
NA	**N**umerical **a**perture
LPP	**L**aser-**p**roduced **p**lasma

Chapter 1

Introduction

1.1 Accelerating technological revolutions

Ray Kurzweil[1]

> *"Technological change is exponential, contrary to the common sense 'intuitive linear' view."*

Technological revolutions have consistently accelerated human progress, with each new era building upon the last at an increasingly rapid pace. Ray Kurzweil's Law of Accelerating Returns [1] describes this phenomenon, highlighting how technological breakthroughs occur exponentially faster over time. For a logarithmic representation of the major human revolutions, see Fig. 1.1.

Around ∼2.5 million years ago, multiple early human species emerged, with *Homo habilis* commonly recognized as one of the earliest known representatives [2]. Anatomically modern humans (*Homo sapiens*) evolved approximately 200.000 to 300.000 years ago in Africa [3]. The Cognitive Revolution, hypothesized to have occurred around 70.000 years ago, is associated with the emergence of complex language, enabling advanced knowledge transfer [4–6]. This development laid the foundation for the Agricultural Revolution (around 12.000 years ago), which introduced farming, permanent settlements, and specialized labor. The Scientific Revolution (∼ 500 years ago) marked a shift toward systematic observation and experimentation, laying the groundwork for modern science. It was followed by the Industrial Revolution (∼ 250 years ago), which brought mechanized production, steam engines, and factory systems. From the late 20th century onward, particularly during the 1990s, the Information and Digital Revolution introduced advances in semiconductors, computers, and the Internet. Today, we are witnessing the Biotechnological & AI Revolution, characterized by breakthroughs in genetic engineering and artificial intelligence (AI).

A critical force behind the Biotechnological & AI Revolution is exponential growth in computing power, often described by Moore's law. It is an observational statement that the number of transistors on a microchip tends to double approximately every two years [7]. From timeframes that span thousands of years to changes unfolding in just a few seconds, each technological

---

[1] Ray Kurzweil, *The Singularity Is Near: When Humans Transcend Biology* (Viking Press, 2005).

revolution has accelerated innovation and reshaped civilization faster than ever before.

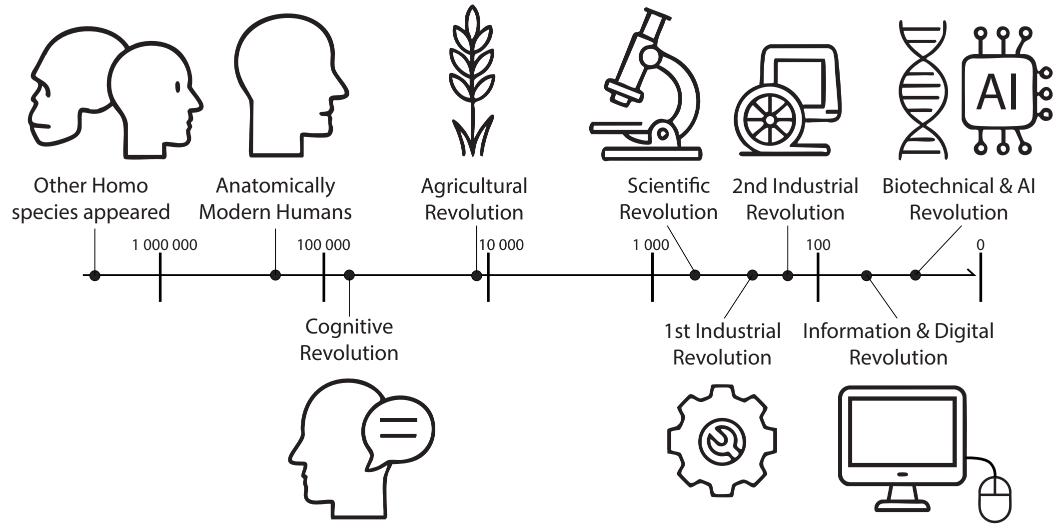

FIGURE 1.1: Illustration of major human, societal, and technological revolutions on a *logarithmic* timescale, from occurrence of early *Homo* species to the Biotechnical & AI Revolution. Based on a draft by the author, improved by Iliya Cerjak (AMOLF).

1.2 Semiconductor scaling

Photolithography is a first step in semiconductor manufacturing [7, 8] as it determines how densely electronic components, such as transistors, resistors, and capacitors, can be packed onto microchips. Reducing the size of these components directly increases computational power, efficiency, and device miniaturization. Photolithography uses light to transfer nanoscale patterns onto a light-sensitive resist coated on a substrate using a mask. These patterns determine the placement of electronic components, such as transistors, resistors, and capacitors, on microchips. The closer arrangement of these components results in faster, smaller, and more energy-efficient chips [7].

The wavelength of light (λ) directly determines the smallest detail that a photolithography system can reliably print on a chip and therefore limits how small transistors can be. The Abbe resolution limit describes this limitation:

$$d = k_1 \cdot \frac{\lambda}{2NA},$$

where k_1 is a parameter correlated with the process of lithography, d is the minimum feature size, λ is the wavelength of light, and NA (Numerical aperture) represents the system's ability to collect and focus light. The semiconductor industry has continuously reduced λ and increased NA to enable the production of smaller and more densely packed transistors.

Photolithography, which used wavelengths of 248 nm and later 193 nm, along with immersion lithography, enabled the fabrication of submicrometer transistors [9]. In late 2018, extreme-ultraviolet (EUV) nanolithography at 13.5 nm enabled the production of sub-7 nm chips [9, 10], with high-NA EUV expected to push transistor scaling toward atomic dimensions [11].

As transistor miniaturization approaches its physical limits, innovations such as chiplet architectures, 3-D stacking, and quantum computing are being explored as new paradigms to sustain computational progress [12].

John Archibald Wheeler

> *"In the middle of difficulty lies opportunity."*

The Biotechnological & AI revolution faces challenges that go beyond the limits of silicon-based scaling. Even if physical limitations can be bypassed by leveraging current AI capabilities to tackle key problems, three main hurdles remain: limited availability of training data, energy consumption, and financial cost. *Limited training data*: Techniques such as AI-supervised learning and synthetic data generation have reduced dependence on large labeled datasets [13], yet the demand for high-quality data persists. *Energy consumption*: Despite advances in computational efficiency and sustainable infrastructure [14], the growing energy demands of AI remain a critical concern. *Financial costs*: Although the cost per transistor continues to decrease, Moore's second law indicates that semiconductor manufacturing costs double approximately every four years [15], posing a significant economic barrier. These challenges also act as catalysts for innovation and the emergence of new paradigms in global collaboration and technological progress.

Neil deGrasse Tyson[2]

> *"The explorer wants to understand it; the soldier wants to dominate it."*

However, technological progress is not dictated by science alone. History shows that governance, economic interests, and geopolitical tensions play a decisive role in shaping innovation trajectories. Weak regulations, power struggles, and fragmented global cooperation can slow or even derail advances [16]. Understanding these global dynamics is crucial, as they influence not only the pace of technological breakthroughs but also their ethical and societal implications.

Within this broader context, EUV nanolithography has emerged as a key enabler of continued transistor scaling. However, as EUV technology approaches its physical and engineering limits, questions arise: How much further can it be pushed, and what innovations are needed to sustain progress?

This thesis contributes to answering these questions by exploring the laser-induced dynamics of liquid tin in state-of-the-art EUV nanolithography machines. These processes are fundamental to the generation of EUV light and

---

[2] From *Cosmos: A Spacetime Odyssey*, Episode 12: "The World Set Free" (2014).

directly impact the efficiency and scalability of the technology. By deepening our understanding of these dynamics, we aim to support the continued advancement of semiconductor manufacturing.

1.3 Microdroplet-tin LPP source for EUV nanolithography

State-of-the-art EUV nanolithography machines utilize 13.5 nm light, generated through laser-produced plasma (LPP). This is achieved by directing a high-power CO_2 laser onto a precisely delivered liquid tin microdroplet, converting it into a plasma that emits the required radiation for advanced semiconductor fabrication.

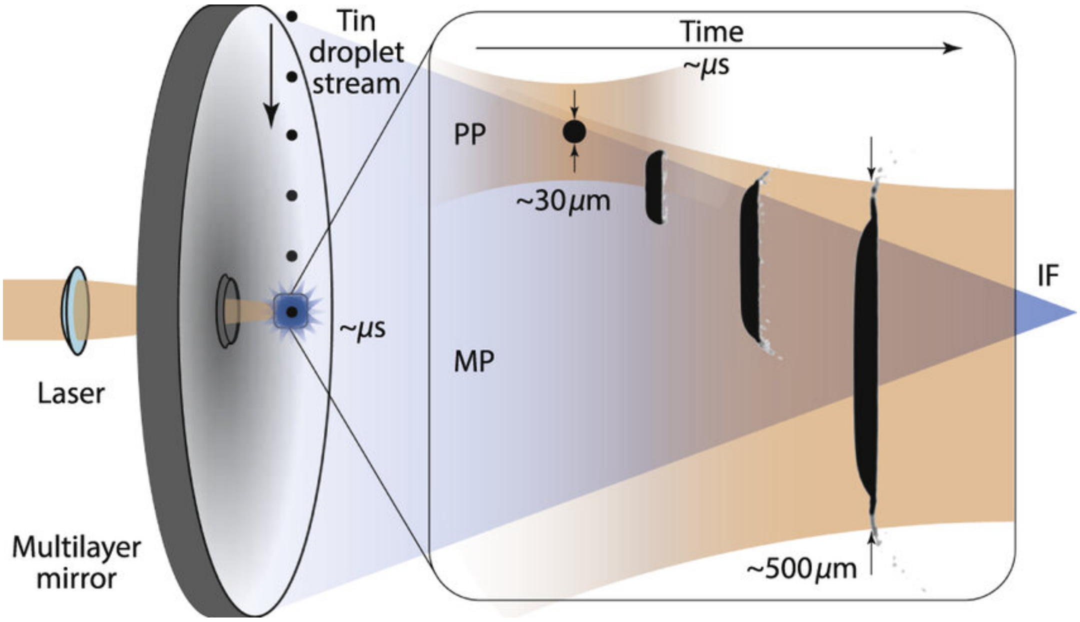

FIGURE 1.2: Simplified schematic of the laser-droplet interaction in a typical industrial EUV light source module. Side-view shadowgraphs showing the transformation of a liquid tin microdroplet (tens of μm in diameter) by a prepulse (PP) into a thin disk, which serves as the target for the main pulse (MP) that generates EUV-emitting plasma, collected and focused toward the intermediate focus (IF). Adapted from [17].

A stream of liquid tin microdroplets, typically several 10 μm in diameter, is first irradiated by a prepulse laser at $t = 0$. For a nanosecond-long prepulse, the droplet deforms into an axisymmetric sheet, as visualized by side- and front-view shadowgraphy images.

The tin plasma emission is collected and directed toward the lithography scanner by a collector mirror, which is a specialized multilayer mirror typically positioned near the laser-droplet interaction region [17]. The CO_2 laser is chosen for its commercial availability at the required high output power and high conversion efficiency (CE). CE is defined as the fraction of in-band

EUV light, emitted within a 2% bandwidth centered at 13.5 nm, that is captured within the half-sphere covered by the collector mirror, relative to the input energy of the drive laser.

1.3.1 Prepulse-induced droplet dynamics

To achieve sufficient in-band EUV power at CE a separate laser pulse, known as the prepulse (PP), was introduced. This laser pulse interacts with the tin droplet prior to the arrival of the main pulse (MP).

The operating principle of this two-step scheme is illustrated in Fig. 1.2. The PP modifies the target geometry, expanding its lateral size and altering its morphology and tin distribution to create a more favorable interaction with the main pulse, thus improving the EUV yield [17–19]. The target geometry is influenced by the PP laser parameters such as the intensity, temporal, and spatial profile [20, 21]. Industrial implementations currently derive the PP from the same CO_2 laser system as the main pulse. However, employing a separate Nd:YAG (1064 nm) solid-state laser as the PP source would offer comparable capabilities while providing improved control over both spatial and temporal pulse shaping.

When a liquid tin microdroplet is irradiated with a nanosecond-long PP, a plasma cloud forms on the droplet's surface facing the incident laser beam. The rapid expansion of this plasma cloud generates a nearly instantaneous recoil pressure of the order of 100 kbar on the droplet surface within the timescale of the PP duration. This sudden force causes the droplet to undergo an impulsive acceleration $\left(a \sim 10^{10}\,\mathrm{m\,s^{-2}}\right)$, leading to its radial expansion to a diameter of the order of 100 µm and its transformation into a thin axisymmetric sheet with a thickness on the order of 100 nm, featuring a micrometer thick central region and an extended rim. [22–26]. This radial expansion, at a velocity on the order of $100\,\mathrm{m\,s^{-1}}$, results in a target diameter of several hundred micrometers within a few microseconds, optimally matching the MP's beam size. At these µs timescales, the redistribution of liquid tin is driven by hydrodynamic motion arising from the interplay between inertial and surface tension forces.

Various hydrodynamic instabilities, i.e., disturbances in the fluid flow that grow over time, can develop on such rapidly expanding liquid sheets. These instabilities play a critical role in determining how the sheet breaks up into droplets, which directly impacts the efficiency of EUV light generation. Uncontrolled breakup can reduce EUV yield and produce excess tin debris, which poses challenges for both optical performance and machine cleanliness [21].

Fast-moving debris not only reduces the available tin mass for EUV generation, but also contaminates the collector mirror, impacting system efficiency and longevity. Thus, accurate characterization of sheet instabilities is essential for improving debris mitigation strategies and extending the operational lifetime of EUV lithography sources.

1.3.2 Advanced target shaping

Previous studies have shown that advanced target-shaping approaches can enhance the conversion efficiency of MP laser photons to EUV photons in laser-produced plasma (LPP) [17]. One such approach involves reducing the volumetric density of tin in liquid tin sheets or generating a preplasma in front of them [17, 27, 28]. These techniques can be implemented by combining a nanosecond prepulse (PP) with a successive low-fluence vaporization pulse (VP), which disperses the tin material over a larger volume, potentially optimizing plasma conditions for EUV generation.

This thesis explores the interaction between the VP and liquid tin sheets, produced by irradiating liquid tin droplets with a PP. Furthermore, it focuses on surface phenomena that occur during droplet deformation.

1.4 Thesis Outline & Summary

In this thesis, we address fundamental questions arising from experiments on laser-propelled tin, motivated by advancements in extreme-ultraviolet (EUV) nanolithography. Driven by scientific curiosity, our investigations have led to the identification of two critical research questions, represented in Fig. 1.3.

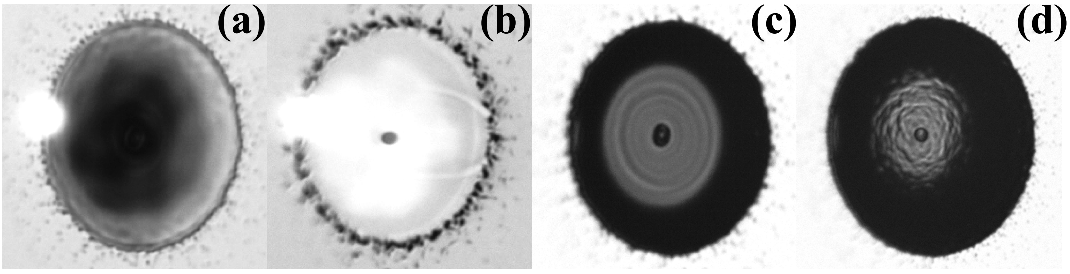

FIGURE 1.3: Sequential snapshots of liquid tin sheets under various laser conditions: (a) vaporization induced by low-intensity VP irradiation, (b) plasma formation under high-intensity VP irradiation, (c) reflection-mode imaging following a low-intensity prepulse (PP), and (d) reflection-mode imaging following high-intensity PP. Note that the small bright circular spots in panels (a) and (b) originate from PP-induced plasma captured during imaging.

Research Question 1: What are the governing mechanisms in the interaction between a nanosecond laser pulse and a free-flying liquid tin sheet?

Understanding this interaction is essential for developing precise target--shaping techniques in which laser pulses form liquid tin into optimal targets for the subsequent main pulse irradiation.

- In **Chapter 2**, we investigate the scaling behavior of laser-induced rarefaction of a liquid tin sheet under varying intensities. A representative shadowgraph that captures a rarefaction state is shown in Fig. 1.3(a).
- In **Chapter 3**, we study the dynamics of plasma formation on liquid tin sheets at higher laser intensities. The analysis provides insight into the transition from vaporization to plasma formation. An illustrative shadowgraph is shown in Fig. 1.3(b).

Research Question 2: What causes the surface modulations observed on expanding free-flying liquid tin sheets?

Unraveling the origin of these modulations improves our understanding of instability-driven sheet dynamics and supports control over target morphology in laser-driven applications.

- In **Chapter 4**, we report experimental observations of axisymmetric (concentric) surface modulations that reproducibly appear under relatively low prepulse laser intensities on expanding liquid tin sheets. This behavior is illustrated in Fig. 1.3(c).
- In **Chapter 5**, we explore the evolution of these patterns with increasing prepulse laser intensity. At higher intensities, azimuthal modulations emerge on top of the concentric surface modulations, as shown in Fig. 1.3(d).

We conclude the thesis with **Chapter 6**, where we reflect on the answers to the above research questions and present an outlook that includes preliminary simulation results addressing open questions.

2

Chapter 2

Scaling Relations in Laser-Induced Vaporization of Thin Free-Flying Liquid Metal Sheets

H. K. Schubert*, D. J. Engels*, R. A. Meijer, B. Liu, O. O. Versolato

Phys. Rev. Research **6**, 023182 (2024)

We experimentally study the vaporization of free-flying liquid tin sheets when exposed to a $100\,\mathrm{ns}$ laser pulse with an intensity ranging from 0.2 to $4.0\times10^{7}\,\mathrm{Wcm^{-2}}$, a case inspired by current developments around 'advanced target shaping' in industrial laser-produced plasma sources for extreme ultraviolet (EUV) nanolithography machines. Our findings reveal a gradual vaporization and a linear relationship between the average vaporization rate and laser pulse intensity $\left(\sim 1.0(3)10^{-7}\,\mathrm{ms^{-1}}/\mathrm{Wcm^{-2}}\right)$, for various targets ranging 20 to $200\,\mathrm{nm}$ in thickness. We introduce a numerical 1-D heating and vaporization model based on Hertz-Knudsen evaporation and find excellent agreement between simulations and experimental data. We furthermore demonstrate that the amount of vaporization of liquid tin targets in the investigated laser intensity range is governed solely by the deposited fluence, and collapse all data onto a single non-dimensional curve, enabling the accurate prediction of vaporization dynamics in applications in future development of EUV sources.

2.1 Introduction

Improvements in semiconductor devices are driven by advances in state-of-the-art nanolithography machines that generate and utilize extreme-ultraviolet (EUV) light. This EUV light is produced by the irradiation of 'mass-limited' liquid tin microdroplets with a double laser pulse scheme [17–19]. First, thin liquid tin sheets ('targets') are produced from droplets using a ns laser 'prepulse' (PP) [21–23, 25, 29–31]. Picosecond prepulses have also been explored in this context previously [18, 19, 32]. This first step enhances EUV light generation in a second step where an energetic 'main pulse' (MP) produces a plasma [17, 19]. Further efficiency gains in the conversion of main pulse laser photons into relevant EUV photons in laser-produced plasma could potentially be obtained by using 'advanced' target shaping approaches [17]. Such

---

* Shared first authorship: Karl Schubert led the experimental measurements and data analysis, whereas Dion Engels developed the Hertz-Knudsen evaporation model in Python.

approaches may include using, e.g., a laser-generated ‘pre-plasma’ as suggested in Refs. [27, 28].

Inspired by such concepts, Liu *et al.* [24] and Engels *et al.* [33] investigated ns laser-vaporization of tin sheet targets with some direct relevance to the industrial use case. More specifically, Liu *et al.* [24] used laser-induced vaporization to uncover previously invisible but important features of the target, such as the center mass and the rim bounding the sheet [21], and proposed scaling relations (relating, e.g., vaporization times to local sheet thickness) in the underlying dynamics. However, no mechanism was identified and no direct experimental evidence was yet provided in support of the scaling relations. There is a range of literature for metals that are subject to ns laser pulses, where three relevant processes can be been identified, namely (a) boiling, (b) vaporization, and (c) phase explosion [34–37]. Normal boiling (heterogeneous nucleation), perhaps the most intuitive and well-known response of a hot liquid, can be ruled out because of the (µs) long time scales involved in the diffusion of vapor bubbles to the surface [35, 36], leaving only vaporization (described by the Hertz-Knudsen equation) and phase explosion (also known as explosive boiling or homogeneous nucleation) as viable options. The work of Engels *et al.* [33] focused on spectroscopic analysis of vapor that was laser-produced from tin targets. The vapor was found to have a homogeneous temperature distribution averaging approximately 3000 K and to contain both atomic and nanoparticulate tin. The observation of the rather low-temperature vapor (near the 2875 K boiling point to tin) may fit a gradual Hertz-Knudsen-type vaporization mechanism and could tentatively be interpreted to rule out phase explosion as a mechanism [33]. However, the authors indicated that the presence of nanoparticles could in fact perhaps best be explained by explosive boiling, thus leaving the vaporization mechanism as an open question.

The prior recent works by Liu *et al.* [24] and Engels *et al.* [33] provide a strong basis but leave significant gaps in the understanding of the vaporization dynamics in qualitative (i.e. the vaporization mechanism) and quantitative (i.e. the scaling relations) terms. Addressing these gaps will benefit and steer ongoing developments in improving laser-produced plasma EUV sources. In this study, we address these gaps in understanding by employing two distinct methods to quantify the vaporization process initiated by an auxiliary laser pulse following a PP, for a range of intensities ($0.2 \times 10^7\,\mathrm{Wcm^{-2}}$ to $4 \times 10^7\,\mathrm{Wcm^{-2}}$) and a range of target types and thicknesses (20 nm to 200 nm). Our approach involves using a long (100 ns) auxiliary vaporization pulse (VP) with a temporal and spatial box pulse profile. We image the vaporization during this long pulse stroboscopically using a ‘shadowgraphy’ technique with 5 ns temporal resolution. The obtained data is employed to demonstrate that the sheet gradually vaporizes (following Hertz-Knudsen evaporation) and to quantitatively study scaling relations to enable predictive modeling of the dynamics.

2.2 Experimental setup

Our experimental setup has previously been described in detail [22, 24, 38]. Here, we present a summary. In the experiment (Fig. 2.1) a kHz train of liquid tin droplets (temperature 270 °C in the current experiments) set to a diameter $D_0 \approx 27$ or 35 µm is vertically dispensed in a vacuum environment (10^{-7} mbar) by a droplet generator. These droplets pass with a speed of the order of 10 m/s through a horizontal sheet of light that is produced by a continuous-wave HeNe laser and positioned a few mm above the center of the vacuum chamber and thus above the laser-droplet interaction point. This light is scattered by the droplets and detected by a photomultiplier tube. Subsequently, the kHz signal is down-sampled to 10 Hz and serves as a trigger for the start of the experiment.

Figs. 2.1(a–d) present a schematic of the laser pulse scheme. First, a droplet is hit by the prepulse [$\lambda = 1064$ nm, circularly polarized]; Fig. 2.1(a) shows the typical response of the droplet to such PP impact. The PP is generated from a seeded Nd:YAG laser system (Continuum Surelight III) that emits temporally Gaussian intensity pulses with a duration of about 10 ns at full width at half-maximum (FWHM). The PP is focused to a Gaussian spot size of approximately 100 µm (FWHM) at the droplet location (at the center of the vacuum chamber). The PP creates a plasma on the droplet, exerting pressure on the remaining liquid tin, which rapidly propels and expands on the order of several 100 m/s to a thin axisymmetric sheet [22, 31]. The propulsion, with a velocity U, is oriented along the propagation direction of the laser, while the orthogonal radial expansion starts with an initial velocity $\dot{R}_0$ at $t = 0$ that is subsequently reduced until it leads to sheet contraction due to the surface tension that is exerted on the edge of the sheet [22, 23, 39]. The timescales that set both accelerations are similar to the duration of the laser pulse (ns) and are much shorter than the timescale of the subsequent fluid dynamic deformation (µs) [22, 23].

Following Klein *et al.* [26] and Liu *et al.* [25] we obtain the initial radial expansion speed $\dot{R}_0$ by fitting a linear function through the first three tracked data points of the liquid tin sheet radius, avoiding shadowgraphs with a strong imaging influence of the PP plasma. A higher E_{PP} causes a higher $\dot{R}_0$, hence less time is required to obtain a certain sheet size D_{s} [25].

Inspired by previous work [24], we start our studies on a liquid tin target that provides thickness ranges between 20 nm and 30 nm (according to semi-empirical thickness model predictions following [25] for a 25 mJ PP on a 27 µm diameter droplet) and refer to it as target $\mathrm{B_{II}}$ consistent with Ref. [24] (for more information about the targets used see Tab. 2.1). Note that the variation in sheet size is very small, with the relative standard deviation of the $\mathrm{B_{II}}$ target size being approximately 1 %. We continue our study on a thicker target for the same conditions (i.e., using the same PP and droplet size) but 1 µs prior to the target $\mathrm{B_{II}}$ and call it for consistency $\mathrm{B_I}$. This target $\mathrm{B_I}$ carries more mass than $\mathrm{B_{II}}$ given the continuous mass loss during expansion [25, 40]. It also exhibits a stronger thickness gradient along the radial coordinate

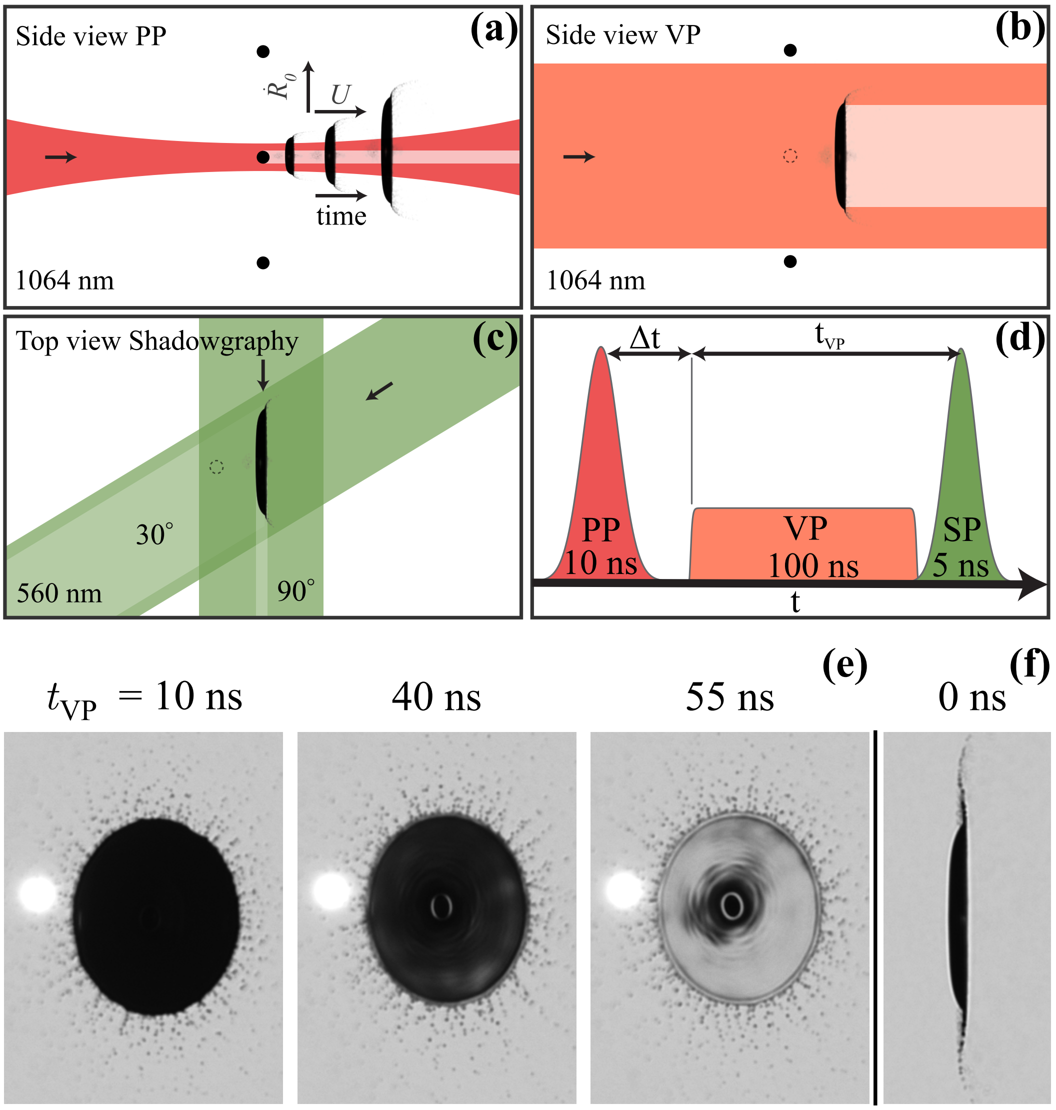

FIGURE 2.1: (a-d) Illustration of the laser pulse schemes with their irradiation geometries. (a) Side-view schematic of the prepulse (PP) including the tin droplet dynamics of propulsion and expansion resulting from the interaction of PP and the spherical liquid tin drop. (b) Side-view schematic of the vaporization pulse (VP) that irradiates a liquid tin target. (c) Top-view schematic of the shadowgraphy illumination pulses. Arrows indicate the viewing angle. (d) Laser pulse scheme in time, starting with the PP that is followed by the VP after Δt. At time $t = 0$ the PP initiates the droplet deformation process. The time $t_{\mathrm{VP}} = 0$ indicates the onset of the VP. The shadowgraphy pulse (SP) is scanned in time over the ongoing VP irradiation of the liquid tin target to capture the vaporization dynamics. (e) A series of front-view green shadowgraphs (at 560 nm) of the thinnest target ($\mathrm{B_{II}}$, see Tab. 2.1) during irradiation by the VP for different t_{VP} with a VP energy $E_{\mathrm{VP}} = 2.5\,\mathrm{mJ}$. The bright spot visible on the left-hand side in the shadowgraphs is due to the PP-induced plasma, the intense radiation of which causes saturation of the CCD chip. (f) Green side-view shadowgraph before irradiation with the VP. PP and VP impact from the left.

compared to B_{II}, providing a thickness range between 20–50 nm [25]. By increasing the PP energy (E_{PP} = 56 mJ) we extend our study to a thicker target, achieving a similar D_s but thicker target at even earlier times (Δt = 1.2 µs). This target is labeled target A [24] with a 50 nm to 150 nm thickness range. Lastly, we shoot a significantly stronger PP (E_{PP} = 100 mJ) at a larger 35 µm diameter droplet and thus create a target 'C' with an approximate 70-250 nm thickness range [25]. Tab. 2.1 also provides non-dimensional times $\Delta t/t_c$ using the capillary time $t_c = \sqrt{(\rho D_0^3)/(6\sigma)}$ which sets the typical time scale for expansion and subsequent retraction, with as input ρ from Tab. 2.2 and $\sigma = 0.54\,\mathrm{N/m}$. The non-dimensional apex time for liquid tin droplets is approximately $\Delta t/t_c \sim 0.4$ [39]. This means that only target B_{II} has passed its expansion apex.

Target	D_0[um]	E_{PP}[mJ]	$\dot{R}_0$[m/s]	Δt[us]	$\Delta t/t_c$	D_s[um]
A	27	56	227	1.2	0.19	396
B_I	27	25	171	2	0.31	382
B_{II}	27	25	171	3	0.46	391
C	35	100	208	1.2	0.13	449

TABLE 2.1: Table of targets used in the experiments with columns of their initial droplet diameter D_0, prepulse energy E_{PP}, initial expansion speed $\dot{R}_0$, time in expansion trajectory Δt, non-dimensional time $\Delta t/t_c$ (see the main text), and the column for their sheet diameter D_s.

In summary, we create different targets to access profiles of different thicknesses (see Tab. 2.1 above, and Fig. 2.7 in the Appendix for more details) enabling the study of the vaporization dynamics over approximately an order of magnitude in thickness.

We next irradiate these targets with a vaporization pulse with a duration of 100 ns [$\lambda = 1064$ nm, circularly polarized, see Fig. 2.1(b)]. The VP is produced by a laser system with arbitrary sub-nanosecond pulse shaping capabilities [41]. The VP laser system generates temporal box-shape pulses of approximately 100 ns and is imaged to a spatial top-hat shape at the center of the vacuum chamber with a size of approximately 820 µm × 820 µm. We use photodiodes (PDs, DET025AL/M) to monitor the VP before entering the measurement chamber, and after transmitting through the chamber. Both laser pulses (PP, VP) are collinearly aligned onto the droplet.

To observe the interaction of the liquid tin sheet with the VP, an imaging setup is used, which is described in detail in Ref. [38]. Briefly, it consists of a dye-based illumination source and CCD cameras that are coupled to long-distance microscopes, yielding a spatial resolution of approximately 5 µm. The illumination source produces pulses with a duration of 5 ns (FWHM) and a spectral bandwidth of 12 nm (FWHM) at 560 nm. We use two synchronous shadowgraphy pulses (SP) for backlight illumination of the front- and side-view acquisitions [at 30° and 90° concerning the laser axis, respectively, see Fig. 2.1(c)] to capture the liquid tin sheet dynamics. Fig. 2.1(d) depicts the time sequence of the aforementioned pulses, highlighting the fact that the SP is scanned (in delay steps) over the ongoing VP ($t_{\mathrm{VP}} = 0$ marks the start of the VP); the VP itself impacts at a time Δt after PP. During each delay step, we record 20 frames in a stroboscopic manner, each representing a different laser-droplet interaction event. This allows us to apply post-filtering techniques, e.g., for selecting sufficiently good laser-to-droplet alignment. The excellent reproducibility of the experiment (showcased, e.g., in the small variation in target sheet size) allows the majority of the collected frames to be used for averaging in the following. Fig. 2.1(e) presents front-view shadowgraphs during VP-induced vaporization with $E_{\mathrm{VP}} = 2.5\,\mathrm{mJ}$, at various t_{VP}. The shadowgraphs clearly show the presence of the sheet's main features: center mass, bounding rim, ligaments, and fragments [25]. We observe gradual mass removal from the sheet with increasing t_{VP} through the increase in transparency of the sheet to shadowgraphy backlight illumination (see Ref. [24]). Fig. 2.1(f) shows the side-view shadowgraphy of the same target before VP impact at $t_{\mathrm{VP}} = 0$.

2.3 Results

First, we investigate the vaporization dynamics of the thinnest target B_{II} using its partial transparency to the green shadowgraphy backlighting (Section 2.3.1). We introduce a 1-D vaporization model based on the Hertz-Knudsen equation. Next, we characterize also the thicker targets (Section 2.3.2). Lastly, we combine and generalize observations of all targets (Section 2.3.3).

2.3.1 Partial transparency

FIGURE 2.2: (a) Heatmap of background light transmission constructed from vertical lineouts through the center of the liquid tin target B_{II} from front-view shadowgraphs, as a function of t_{VP} using $E_{\mathrm{VP}} = 2.5\,\mathrm{mJ}$. (b) Front-view shadowgraph with digitally enhanced contrast at $t_{\mathrm{VP}} = 36\,\mathrm{ns}$. (c) Average target transmission values $\bar{T}$ (on a logarithmic scale) during the vaporization of the target $B_{\mathrm{II}}$for energies E_{VP} = 1.2 (blue data), 2.5 (green), 4.2 (red), and 8.2 mJ (brown). Shaded areas represent the uncertainty (see the main text). Bold and dashed lines show simulation results using the refractive index with the highest temperature in the literature available (1373.15 K [42]) and an extrapolated refractive index for the expected temperature for each energy case, respectively. (d) Average target thickness values $\bar{h}$ during the vaporization, obtained by applying the transmissivity method to the average transmission values shown in the upper graph. The bold lines show the simulation results. Inset (e) shows average vaporization rates $\dot{h}$ over VP intensity and the result of a linear fit to the data yielding a 1.1(3) proportionality factor. (f) Average target thickness values $\bar{h}$ as a function of deposited fluence.

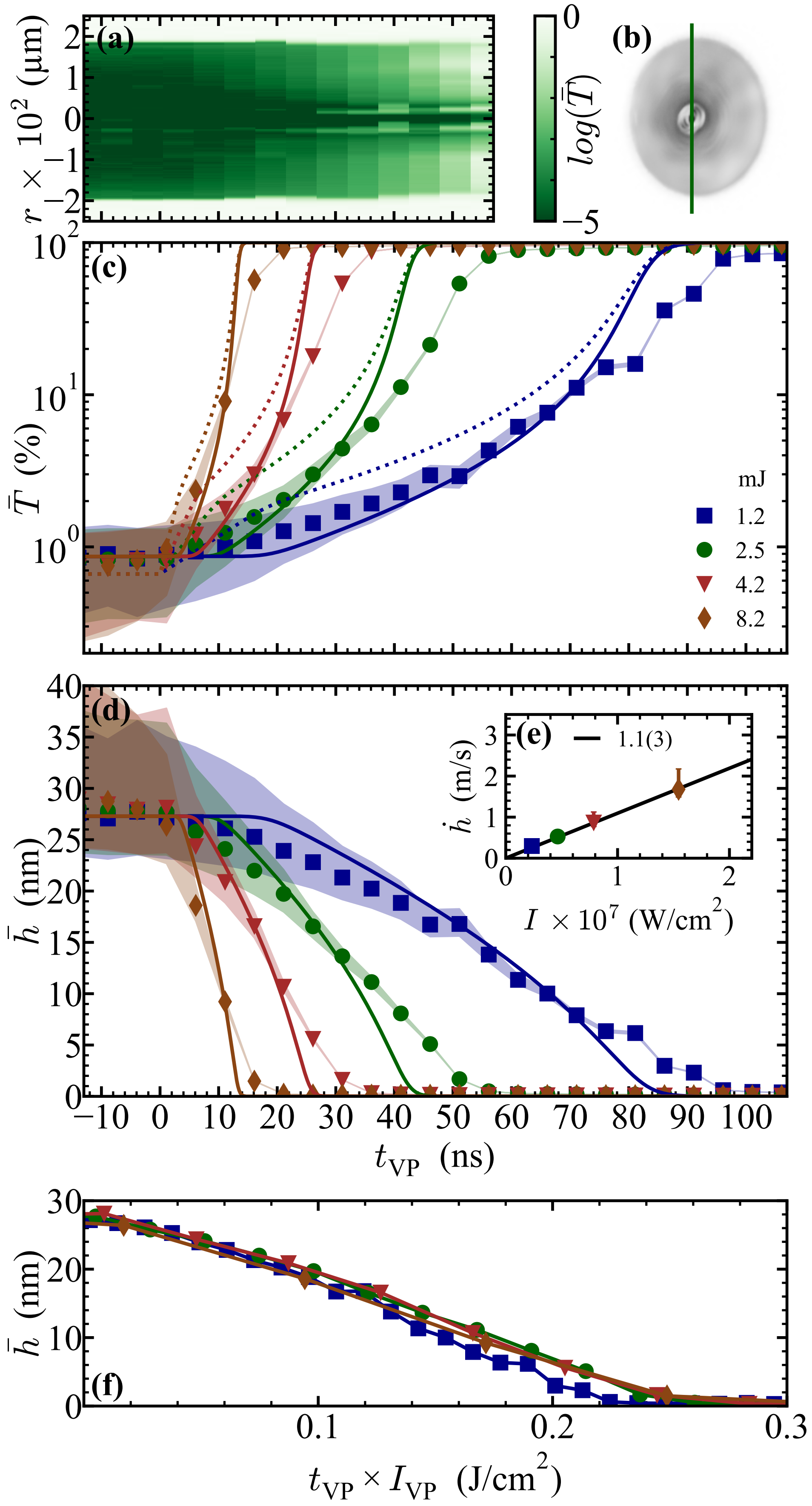
(a)
r × 10² (μm)
2
1
0
−1
−2
0
log(T̄)
−5
(b)
(c)
T̄ (%)
10²
10¹
10⁰
mJ
■ 1.2
● 2.5
▼ 4.2
◆ 8.2
(d)
h̄ (nm)
40
35
30
25
20
15
10
5
0
(e)
ḣ (m/s)
— 1.1(3)
0
1
2
3
I × 10⁷ (W/cm²)
−10
0
10
20
30
40
50
60
70
80
90
100
t_VP (ns)
(f)
h̄ (nm)
30
20
10
0
0.1
0.2
0.3
t_VP × I_VP (J/cm²)

In Figure 2.2(a), a heat map is presented that shows the transmission of background light through the target B_{II} for E_{VP} = 2.5 mJ. This heat map illustrates the variation in transmissivity as a function of t_{VP}, here taken along a vertical lineout passing through the center of the target [cf. Fig. 2.2(b)]. These lineouts are aligned and averaged per delay step. The heatmap shows that as t_{VP} increases, the target gradually becomes more transparent, indicating a gradual thinning process. The choice of a logarithmic scale is motivated by the near-exponential scaling of the absorption of shadowgraphy light with the thickness of the liquid tin target. We note that the central mass feature (see Refs. [21, 25]) appears to remain unvaporized. The halo-like, high transmissivity region observed around the center suggests that the connecting sheet part is particularly thin between the sheet and the central mass feature. Figure 2.2(b) displays a front-view shadowgraph, shown with artificially enhanced contrast, taken at t_{VP} = 36 ns. At this specific time point, the sheet exhibits significant transparency, illustrating the ongoing gradual reduction in thickness.

In Figure 2.2(c), we present averaged transmission values as a function of t_{VP} for various E_{VP}. These curves provide a quantitative representation of how transmission values evolve with t_{VP} across the dynamic range of our 12-bit acquisition. To obtain these values, we average transmission values between 100 and 155 µm radius on both sides of the vertically centered sheet lineout. This selected radial range deliberately excludes the center mass and rim features, focusing on regions of this target with approximately uniform thickness (cf. Ref. [25]). The shaded areas surrounding the plotted data points represent the uncertainty range (see discussion below).

We determine the target thickness using a method that utilizes its partial transparency to green backlighting. This approach follows the methods previously outlined by Vernay [43], further developed for liquid tin targets by Liu *et al.* [25]. We employ the `tmm` [44] Python package to establish a connection between optical target transmission and target thickness. This general transfer-matrix method optics package is used for calculating the reflection, transmission, and absorption of multilayer films. Our more versatile method here slightly deviates from the method outlined in [25, 45], but does not lead to significant numerical differences. We extract, pixel-wise, raw optical target transmission values, denoted P_{ij} with i and j representing pixel indices. Before linking the local transmission with thickness, we preprocess the shadowgraphs to account for backlight intensity fluctuations and ‘dark’ value. The parameter P_0 characterizes this overall dark value, including imaging glare sources such as PP plasma, VP scattering, target emission, SP, and electrical noise, all of which contribute to camera exposure. We employ the formula $T_{ij} = (P_{ij} - P_0)/(P_b - P_0)$, with P_b as the mean background value determined from the shadowgraph bin count. To determine P_0, we average the values of a 9x9 pixel area centered around the center of mass in front-view shadowgraphs, which corresponds to the thickest (and thus darkest) part of the sheet [21]. We separately obtain P_0 values for each VP energy, using frames where the SP arrives before the VP, thus enabling accounting for any potential scattering of the VP onto the imaging system. After establishing the relationship between T_{ij} and thickness h (using the `tmm` package), we correct for the 30° acquisition angle via $\bar{h} = \bar{h}_{30} \cdot \cos(30°)$. In Fig. 2.2(d), average sheet thickness values, obtained using the data from Figure 2.2(c), are presented. The curves demonstrate a continuous decrease in average sheet thickness with increasing t_{VP}. The shaded areas indicate uncertainty ranges resulting from error propagation, dominated by uncertainties in establishing the dark value at $0.046(5)$, which incorporates a ±10% uncertainty in its determination [this uncertainty also gives rise to the uncertainty region shown in Fig. 2.2(c)]. We note that the uncertainty, also in a relative sense, increases sharply with increasing thickness, limiting the application range of the current method to sheet thicknesses below approximately 25 nm. As a consequence, a different quantification method is required for studying thicker sheets. The gradual reduction in sheet thickness over time due to vaporization, as depicted in Figure 2.2(d), displays a nearly linear behavior. This motivates us to extract a (averaged) rate or, a recession *speed*, of vaporization. To calculate the vaporization rates, we determine the time required for the sheet to reduce from its original thickness to approximately 2 nm, using the data from Figure 2.2(d).

Figure 2.2(e) presents the resulting vaporization rates for the various VP intensities. The data reveal a linear dependence of vaporization rate on VP intensity, in line with the claims of Liu *et al.* [24]. By applying a linear fit to these vaporization rates for all intensities, we determine a proportionality factor $d\dot{h}/dI_{\mathrm{VP}}$ of $1.2(2)\,10^{-7}\,\mathrm{ms}^{-1}/\mathrm{Wcm}^{-2}$, linking vaporization rate to VP intensity. This scaling factor enables us to predict average vaporization rates for a given VP intensity. The observed linear dependence of vaporization rate on VP intensity motivates plotting the sheet thickness as a function of deposited laser fluence $t_{\mathrm{VP}} \times I_{\mathrm{VP}}$, as shown in Figure 2.2(f). This approach results in the collapse of the full dataset, supporting the linear scaling of vaporization rate with intensity and indicating that the thinning is solely a function of the deposited laser pulse energy.

We next use an energy balance model to explain the apparent linear scaling of vaporization rate with VP intensity. The energy required to vaporize a unit volume of tin is $\rho H/M$ (J/m^3), where ρ is the density, H is the latent heat and M is the molar mass. This energy will be supplied by the laser, which deposits per unit area a power aI (J/m^{2}s), where a is the absorptivity of the metal, and I is the intensity of the laser. Balancing these energy terms out gives a rate (m s^{-1})

$$\dot{h} = \frac{aI}{\rho H/M} \tag{2.1}$$

Filling in typical values (see Appendix 2.4 for these values) and assuming 20 % absorptivity (typical for ∼25 nm thick tin films according to multilayer optical calculations [44]) gives a predicted dependency of $\dot{h}$ on intensity of $1.2\,10^{-7}\,\mathrm{ms}^{-1}/\mathrm{Wcm}^{-2}$.

Inspired by the close match of the simple energy balance argument with the experimental observation, we create a numerical 1-D heat diffusion and vaporization solver to model and gain insight into the vaporization dynamics. The 1-D space is divided into individual cells with typical cell lengths of 100 pm. For each cell, the temperature is the key variable. Four steps are performed for each time step in the code.

(i) A surface recession speed (v, also one-sided vaporization rate) is calculated based on Hertz-Knudsen evaporation [46] for the front and back surfaces. For the pressure, the vapor pressure following the Antoine equation is used, resulting in

$$v = \frac{10^{A-[B/(T+C)]}}{\sqrt{2\pi MRT}}\frac{M}{\rho}, \tag{2.2}$$

where T is the surface temperature, M the molar mass, and R the gas constant. The parameters A, B, and C are 6.60, 16 867, and 15.47 respectively [47, 48]. A cell is considered vaporized when the surface recession (along the surface normal) has passed through the entire cell size. At that moment, it is removed from the simulation domain and no longer interacts with the remaining liquid via heat diffusion.

(ii) Recession of the surface causes a reduction in temperature in the cells where vaporization occurs, which are the first and last active cells. This is due to the latent heat required to transform the liquid atoms into gas, and thus to recess the surface. We can obtain a temperature reduction in the cell by balancing the energy input (heat capacity) and output (vaporization)

$$c_p \Delta x \Delta T = H v \Delta t \rightarrow \Delta T = \frac{H}{c_p \Delta x} v \Delta t, \tag{2.3}$$

where c_p is the molar heat capacity (with units [J/(mol K)]), Δx the cell size, and ΔT the temperature change, giving the input. The output is given by the latent heat H, and the size of the vaporized part, which is given by v, the recession speed, multiplied with Δt, the time step. This temperature reduction (and the recession) is calculated at every time step, not only when the entire cell is vaporized; this makes the temperature reduction and thickness reduction 'continuous' (with fs time steps) while the cell deactivation is discrete (a few hundred cells).

(iii) The first active cell is heated by the incident laser light. The absorptivity of the laser light is continuously updated based on the current remaining thickness of the tin. The absorptivity is calculated using the `tmm` [44] Python package. The refractive index used is the highest temperature data available for tin [42]. Thus, an energy balance for the laser heating, where absorbed energy is equated to a change in temperature, can be used to obtain a temperature change of the front cell

$$aI\Delta t = (c_p/M)\rho \Delta x \Delta T \rightarrow \Delta T = a\frac{I\Delta t}{(c_p/M)\rho\Delta x}. \tag{2.4}$$

(iv) The heat is diffused through the active cells. Fourier's law is discretized using a forward Euler method, resulting in

$$T_i^{t+1} = T_i^{t-1} + \frac{\alpha \Delta t}{\Delta x^2}\left(T_{i-1}^t - 2T_i^t + T_{i+1}^t\right), \tag{2.5}$$

where i indicates the different cells, and α is the thermal diffusivity. The prefactor needs to satisfy $\alpha\Delta t/\Delta x^2 < 0.5$ to ensure stability of the forward Euler method and sets the maximum time step to typically 10 fs for our 100 pm discretization.

The sole inputs of the code are the starting thickness and the laser intensity, after which the model calculates the thickness and temperature of the 1-D tin slice over time and saves this in output files. Appendix 2.4 includes some detail on the sensitivity of the model to the input parameters, and provides an overview of the input parameters used in the simulation. Within the model, the vaporization time t_{vap} is defined as the moment when only 2 nm of liquid tin is left, just as in the experiment. A $\dot{h}$ consistent with the experimental definitions can also be defined by dividing the initial thickness by the time period t_{vap}. To complete the comparison with the experimental observable, the transmission of the 1-D liquid slice is calculated using the same `tmm` package. We also account for the change in the refractive index of tin as it heats and the 30 deg observation angle of incidence when calculating the transmission via the 1-D model.

Fig. 2.3 shows detailed outputs from the code for the $E_{\mathrm{VP}} = 2.5\,\mathrm{mJ}$ case in Fig. 2.2. Initially, the tin is heated rapidly. As the temperature increases, so does the surface recession velocity, as it strongly depends on T. At a certain point, the energy loss to vaporization starts to dominate and even completely stops any heating, perfectly balancing out the input energy by the laser. The final temperature is around the temperature found (approximately 3000 K) in experimentally produced tin vapors [33], underwriting the validity of our approach. We only show the temperature on the laser side since thermal diffusion keeps both sides of the 1-D domain at the same temperature within a few Kelvin. This equality aligns with expectation, given the typical thermal diffusion timescale that can be obtained from Fourier's law

$$\Delta t \approx \frac{h^2}{\alpha}, \tag{2.6}$$

where α is the thermal diffusivity. Taking a conservative value of $\alpha = 16.5\,\mathrm{mm^2/s}$ at a low temperature of 505 K [49] and a typical $h = 25\,\mathrm{nm}$ results in a timescale of $\sim$40 ps, much shorter than the relevant vaporization dynamics. We also note that the rapid heating induces a refractive index change and thus adds uncertainty to the transmissivity method because this heating cannot be experimentally observed.

The right axis of Fig. 2.3 also shows an energy balance of the calculations. The energy balance highlights the points mentioned above: an initial heating phase is present before the energy loss to vaporization balances out with the

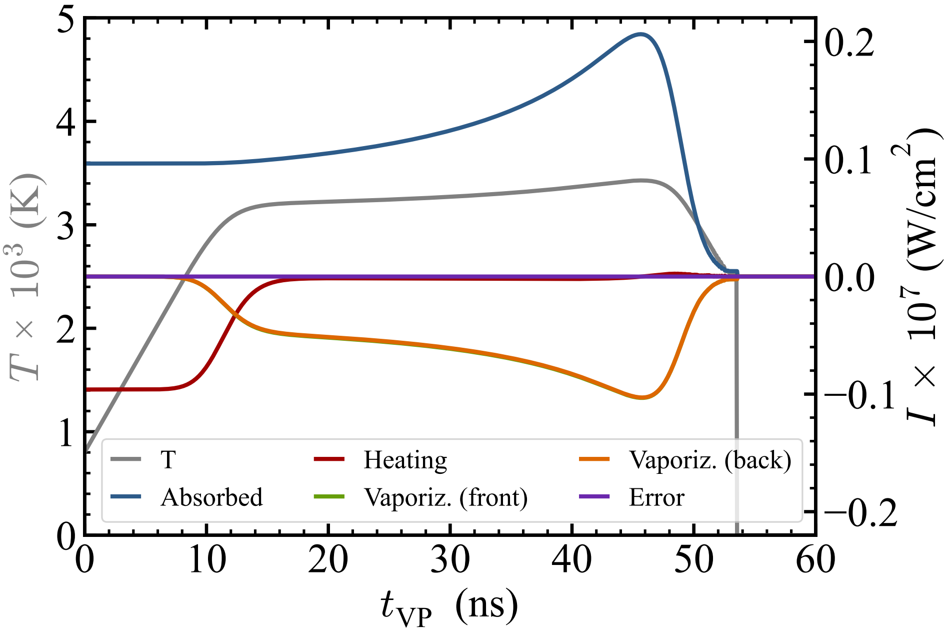

FIGURE 2.3: Example time-resolved output from the 1-D numerical code (aligning with the $E_{\mathrm{VP}} = 2.5\,\mathrm{mJ}$ case from Fig. 2.2). The left axis shows the temperature at the laser side over time. The right axis shows the code's internal energy balance, split in absorbed laser energy, heating of the liquid (which is an energy sink and thus negative, even though the temperature in the liquid goes up), vaporization on the front and back surfaces (which are indistinguishable), and an internal energy 'error,' being the difference between absorbed energy and the energy loss mechanisms.

laser input, stabilizing the temperature of the liquid. The absorbed energy peaks when the 1-D slice is around 4 nm thick as the absorptivity increases as the sheet thins, increasing the temperature with it and thus speeding up the surface recession. The absorptivity of the liquid reduces strongly at even lower thicknesses, causing a rapid temperature drop at the end of the vaporization process.

The resulting thicknesses, as a function of t_{VP}, for the different cases are shown in Fig. 2.2(d). The simulated curves overall show good agreement with the experimental data given the absence of any free-fit parameters. We note that the experimental data points appear to lack the clear plateau that is present in the simulations due to the heating phase. We hypothesize two reasons for this discrepancy. First, the initial temperature of the liquid in the simulation (set to 800 K based on radiation hydrodynamic simulations [50, 51]) could be too low, increasing the heating period in the simulation. However, much higher values are not supported by the radiation hydrodynamic simulations. Second, the differences may be due to changes in the refractive index due to heating, causing the experimental method to misinterpret the measured transmissivity. The experimental method cannot distinguish the transmission changing through thinning or heating, and thus will interpret any refractive index change as a thickness change. To investigate the impact of heating on the transmissivity method more, we show two transmission curves (solid and dotted) in Fig. 2.2(c) that we obtain by applying the (inverse) transmissivity method to the thickness prediction curves from the 1-D heat simulation. These curves correspond to two refractive index cases, with the solid line corresponding to the highest temperature for which there is literature data available, $n_{1373.15\mathrm{K}} = 3.93 + 7.87j$ [42], and the dotted line using a linear extrapolation of the literature data to the actual temperature (as predicted by the 1-D simulations). The results show that the observed transmission falls between the two lines, indicating that the lack of a plateau in the experiment may be due to the changing refractive index — although our linear extrapolation most likely strongly exaggerates the change in refractive index. A second deviation between the simulation and experiment is the lack of increased vaporization rate at very low thicknesses in the experimental data. As mentioned, this accelerated vaporization is a simple consequence of the Fresnel equations, as discussed in detail in [52]. We speculate that the vapor surrounding the liquid (which absorbs a small amount of light and thus skews the transmissivity measured) obstructs the observation, or that the finite 5 ns length of the illuminating pulse blurs out the effect. Overall, besides these minor differences, we find excellent agreement between simulation and observational experimental data, indicating that the model reliably describes the vaporization process. Our experimental observations, combined with this agreement between simulation and experiment, validate the view of the vaporization process as a gradual process according to Herz-Knudsen, rather than as violent explosive boiling.

2.3.2 Edge tracking

After gaining an understanding of the vaporization mechanism for the thinnest sheet in our studies (approximately 25 nm for B_{II}), we now extend our studies to much thicker targets, reaching up to approximately 200 nm in thickness. For these large thicknesses, the transmission method cannot be used to track the thinning over the full vaporization of the sheet. These thicker sheets are expected to exhibit a larger spatial thickness gradient (see Appendix A, Fig. 2.7). The presence of such a steep thickness gradient enables us to define and track the edge of the vaporizing sheet, which effectively represents a nearly discrete transition between the fully vaporized and remaining liquid regions. The two regions are characterized by very different contrast levels. This contrast difference is due to the green backlight being able to penetrate through the tin vapor while being extinguished by the remaining liquid sheet part. We refer to the method of tracking the discrete transition as 'edge tracking'. We explain the method in detail in Appendix 2.4. This method relies on PD data of the VP exiting the vacuum chamber.

FIGURE 2.4: (a) Side- and front-view shadowgraphs of target B_I, A, and C before VP irradiation. The bright spots are due to the plasma emission caused by the PP. (b) Front-view shadowgraphs of target A visualizing the vaporization process at times t_{VP} for E_{VP} = 8.4 mJ. (c,d, and e) Inner sheet radii during vaporization for targets B_I, A, and C, respectively. The inset numbers indicate the used VP energy and the dashed lines are corresponding simulation results (see the main text).

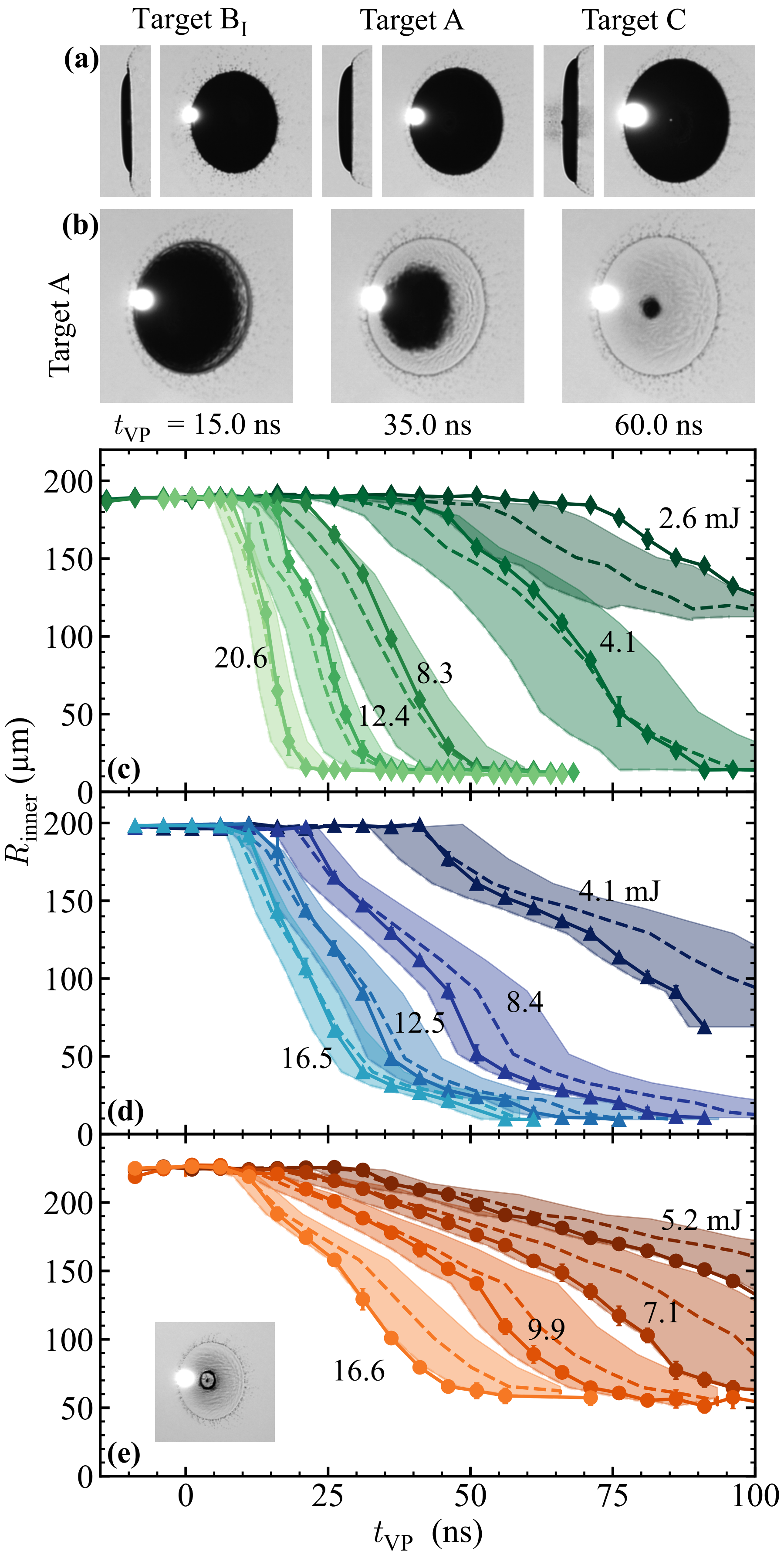
Target B_I
Target A
Target C
(a)
(b)
Target A
t_{VP} = 15.0 ns
35.0 ns
60.0 ns
2.6 mJ
4.1
8.3
12.4
20.6
(c)
4.1 mJ
8.4
12.5
16.5
(d)
5.2 mJ
7.1
9.9
16.6
(e)
R_{inner} (μm)
0
50
100
150
200
0
25
50
75
100
t_{VP} (ns)

Fig. 2.4(a) displays shadowgraphs of the liquid tin target $\mathrm{B_I}$, A, and C before VP irradiation in front and side view, allowing a qualitative comparison of the target morphology. Fig. 2.4(b) shows front-view shadowgraphs of the target A for three times t_{VP} for an $E_{\mathrm{VP}} = 8.4\,\mathrm{mJ}$, clearly showcasing the recession of the inner sheet due to vaporization. We observe that the outer and thinner sections of the sheet become transparent earlier than the inner and thicker regions, leaving behind an identifiable inner remaining sheet. This inner radius $R_{\mathrm{inner}}(t_{\mathrm{VP}})$ is tracked, following the edge-tracking method introduced above. At $t_{\mathrm{VP}} = 60\,\mathrm{ns}$, Fig. 2.4(b) shows that the rim, ligaments, fragments, and center mass do not fully vaporize. This can be understood from their considerably larger, micrometer-scale thickness [21]. Vaporization of these thick features is only observed when there is a significant increase in VP energy.

Figs. 2.4(c, d, and e) show the edge-tracking results for the inner sheet radii results for targets $\mathrm{B_I}$, A, and C, respectively. Fig. 2.4(c), shows that the inner sheet radii decrease as t_{VP} increases and that this reduction is sped up at higher VP energies. This observation aligns with our observations shown in Fig. 2.2 for a much thinner target. The reduction of the inner sheet of the target $\mathrm{B_I}$ [Fig. 2.4(c)] with time highlights certain differences in target morphology when compared to A and C [Fig. 2.4(d,e)]. In the case of target A [Fig. 2.4(d)], we observe that the rate of reduction of R_{inner} slows down significantly for radii below 50 µm. This suggests the presence of a thicker center region. The edge-tracking analysis of target C [Fig. 2.4(e)] reveals even more pronounced differences around the center, with its inner radii converging to approximately 50 µm after which the vaporization process seems to end. As shown in the shadowgraph inset, the converging radius is not due to a thicker center region but, rather, a thick rim surrounding a center mass. See Appendix A, Fig. 2.8 for further detailed shadowgraphs showing this specific feature. The occurrence of such peculiar center mass features is yet not fully understood. In previous work, such features were hypothesized to be attributable to compressible flow effects, specifically to a collapsed cavity generated by the PP [21]. In the current study, we focus on the sheet vaporization dynamics away from any such compressible flow artifacts.

To relate the inner sheet radii to a local thickness, with the final goal of studying the local vaporization rates, we next employ the semi-empirical thickness model introduced by Liu *et al.* [25] for laser-shaped tin targets such as ours. This model is based on a self-similar solution derived from the model by Wang *et al.* [53]. It assumes an inviscid radially outward flow in the expanding sheet, neglecting curvature-induced radial pressure gradients and sheet features such as the center mass. A solution to the non-dimensionalized equation governing the sheet expansion can be found in the form [53]

$$h^* t^{*2} = f\left(\frac{r^*}{t^*}\right), \tag{2.7}$$

with the self-similar variables denoted as $r^* = r/D_0$, $t^* = \dot{R}_0 t/D_0$, and $h^* = h/D_0$. Any actual (dimensional) thickness profiles $h(r, t, \dot{R}_0, D_0)$ can be collapsed onto a single self-similar curve $y = f(x)$. Conversely, given any set of experimental inputs (such as droplet radius, time after impact, etc.), the local thickness can be obtained if $f(x)$ is known. Precisely this function was previously obtained by Liu *et al.* [25] as

$$f(x) = \frac{1}{a_0 + a_1 x + a_2 x^2}, \tag{2.8}$$

with $a_0 = 1.65(2)$, $a_1 = 6.9(3)$, and $a_2 = -2.4(8)$ as parameters that were determined by fitting the proposed $f(x)$ to the available experimental data [25], thus yielding a semi-empirical thickness model

$$h(r, t, \dot{R}_0, D_0) = \frac{D_0^3}{a_0 \dot{R}_0^2 t^2 + a_1 \dot{R}_0 t r + a_2 r^2}. \tag{2.9}$$

Here, $\dot{R}_0$ is input from the measured initial droplet expansion speed (following Ref. [24] in contrast with the choice of using propulsion U of the original Ref. [25]), D_0 is the initial droplet diameter, and t, r represent time and radial coordinates, respectively. This semi-empirical model allows us to effectively characterize the used targets (see Fig. 2.7 in the Appendix).

Before using this model, we note that target C exhibits a prominent and peculiar inner center rim surrounding the center mass. This feature along with a center mass is not predicted by the model. Consequently, we may expect that the mass that is assumed to be available to produce the sheet is overestimated. We first seek to correct target C for the additional mass loss channels. According to findings from Ref. [21], between 5 and 20 % of the mass is concentrated in a center mass remnant, with no obvious predictive scaling available. Given that we observe both a prominent center mass and an additional ring-like feature, we conservatively take the upper limit (20 %) as an estimate for the mass lost to such compressible flow features. Furthermore, given the large PP energy, we also should correct for the amount of mass that is lost through the ablation process that sets in motion the dynamics. From prior simulations in Ref. [21], and the heuristic scaling law provided therein, we may estimate such ablation losses to account for an additional 20 % mass loss. Thus, in the following, we take target C to have approximately 40 % less mass available on the sheet as would be expected from the initial large droplet size (cf. Fig. 2.7 in the Appendix).

Next, we return to the vaporization model of the previous Section 2.3.1. The model requires as input h, here obtained from the semi-empirical thickness model, which enables converting the measured R_{inner} (cf. Fig. 2.4) to a local thickness h. Taking this local thickness h for each R_{inner} as input, the simulation results in a t_{vap}, which is plotted in Figs. 2.4(c-e) as the dotted curves. The colored bands depict uncertainty estimates based on a 15% uncertainty on the actual thickness. Overall, good agreement is found between simulations and experimental data, well within the uncertainty estimates. The agreement is most striking for target B_I aside from the lowest energy case (2.6 mJ). This minor discrepancy may in part be attributed to uncertainty in the energy calibration. Target A also shows good agreement but a systematic offset towards later t_{VP} can be tentatively identified. Such an offset may be attributed to the fact that mass is also lost on target A, given that ablation and compressible flow also feature here if less strongly than for target C. Target C shows the same systematic offset towards later t_{VP} which may indicate that the applied compressible flow (or ablation) correction still underestimates the true value. Still, there is full agreement between simulation and experimental data within the stated uncertainty estimates over both approximately an order of magnitude in thickness and vaporization laser intensity.

To enable accurate prediction of vaporization dynamics given a certain laser intensity, we next turn to averaged vaporization rates — reducing the data in Fig. 2.4 effectively to a single key parameter, $\dot{h}$. This parameter is obtained by minimizing the difference between (h, r) and $(\dot{h}t_{\mathrm{VP}}, r)$ curves with $\dot{h}$ a free fit factor, a method that is inspired by the approach of Liu *et al.* [24]. We perform the fit in the region of the sheet, well away from the rim and center mass features. The values (h, r) are obtained from Eq. (2.9) at R_{inner} at $t = \Delta t$ [cf. Table 2.1].

Fig. 2.5 depicts a linear correlation between the thus obtained vaporization rates ($\dot{h}$) and VP intensity for all targets within the investigated vaporization laser intensity range of approximately 1 W/cm^2 to 5×10^7 W/cm^2.

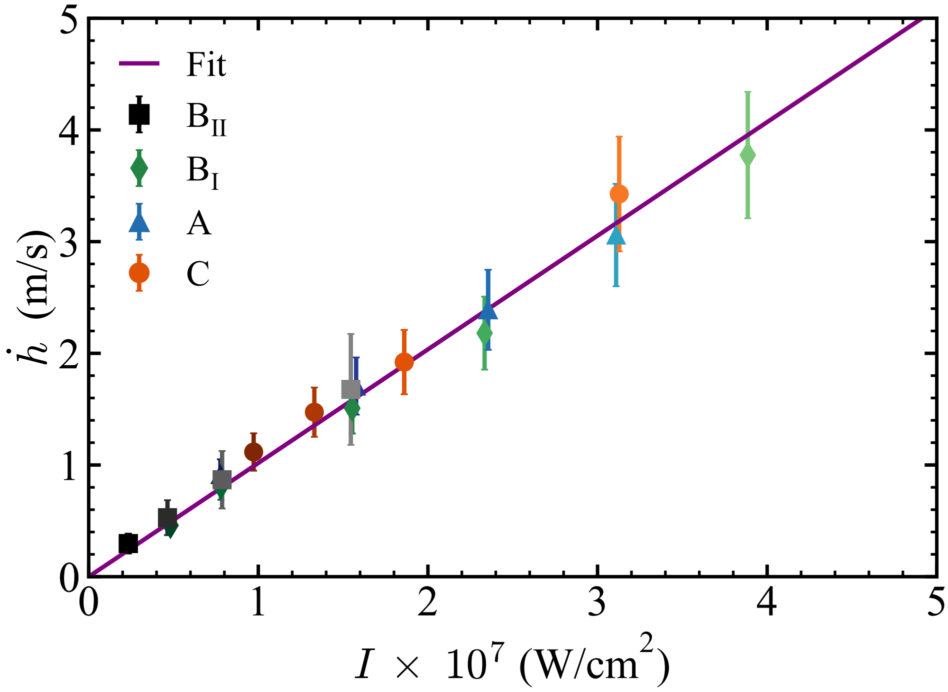

FIGURE 2.5: Average vaporization rates of the targets B_{II}, B_I, A, and C as a function of VP intensity. The purple line shows the result of a linear fit to the concatenated data. The shaded area indicates the fit uncertainty.

The rate values for target B_{II} are directly taken from Fig. 2.2(e). For all other targets (B_I, A, C), the vaporization rates ($\dot{h}$) are the result of the comparison between t_{VP} and the thickness prediction obtained from the semi-empirical thickness model as explained above (cf. Fig. 2.7). For target B_{II}, the uncertainty arising from the initial target thickness was taken into consideration with ± 15 % (from the dark value correction), and for all other targets (B_I, A, C), a standard deviation of ± 15 % was assumed as an uncertainty measure (dominated by the uncertainty in available mass). The observed increase in uncertainty with the VP intensity (cf. Fig. 2.5) is a direct result of the constant delay step size when scanning the SP over the VP, for all measurements, leading to fewer steps during the VP for higher intensities. Finally, we perform a linear fit to the merged dataset of average vaporization rates and obtain a $d\dot{h}/dI_{\mathrm{VP}}$ of $1.0(3)\,10^{-7}\,\mathrm{ms}^{-1}/\mathrm{Wcm}^{-2}$, in agreement with and extending the linear scaling of Section 2.3.1 over an order of magnitude in both thickness and laser intensity. The vaporization rate is thus observed to linearly scale with intensity, *independently* from both initial and instantaneous thickness; the time t_{vap} required to vaporize a sheet of thickness h will scale as $t_{\mathrm{vap}} \propto h I_{\mathrm{VP}}^{-1}$ with the $\dot{h}$ at every instant scaling as $\dot{h} \propto I_{\mathrm{VP}}$.

We note that a previous study [24] reported a vaporization rate of 4.4 m/s for a ∼0.7 J/cm^2 fluence laser pulse, 50 ns in duration (yielding an intensity of approximately $1.4\times10^7\,\mathrm{Wcm}^{-2}$) which is a faster rate than would be expected from our observations. However, the authors of Ref. [24] acknowledge an error in a double correction of the vacuum window transmissivity (upscaling the input I_{VP}). Additionally, we have improved the edge tracking method by benchmarking it to the photodiode data, which also causes a slightly different result. Accounting for both differences brings the previous data again in agreement (at ∼3 m/s at $2.2\times10^7\,\mathrm{Wcm}^{-2}$) with the present more accurate observations.

2.3.3 Self-similarities and generalization

We next revisit all experimental data and further study two key findings of this work, namely that $t_{\mathrm{vap}} \propto h I_{\mathrm{VP}}^{-1}$ and $\dot{h} \propto I_{\mathrm{VP}}$ which can be transformed into each other $\dot{h} \propto h/t_{\mathrm{vap}} \propto I_{\mathrm{VP}}$. Fig. 2.6(a) shows the result of multiplying the t_{VP} time axis by the VP intensity I_{VP} to arrive at a local fluence $t_{\mathrm{VP}} \times I_{\mathrm{VP}}$ previously presented only as an Ansatz in Ref. [24]. It demonstrates that the vaporization of liquid tin targets in the investigated laser intensity range $0.4\times10^7\,\mathrm{Wcm}^{-2}$ to $4\times10^7\,\mathrm{Wcm}^{-2}$ is solely a function of the deposited fluence, across all individual targets. This underpins the first key finding that $t_{\mathrm{vap}} \propto I_{\mathrm{VP}}^{-1}$.

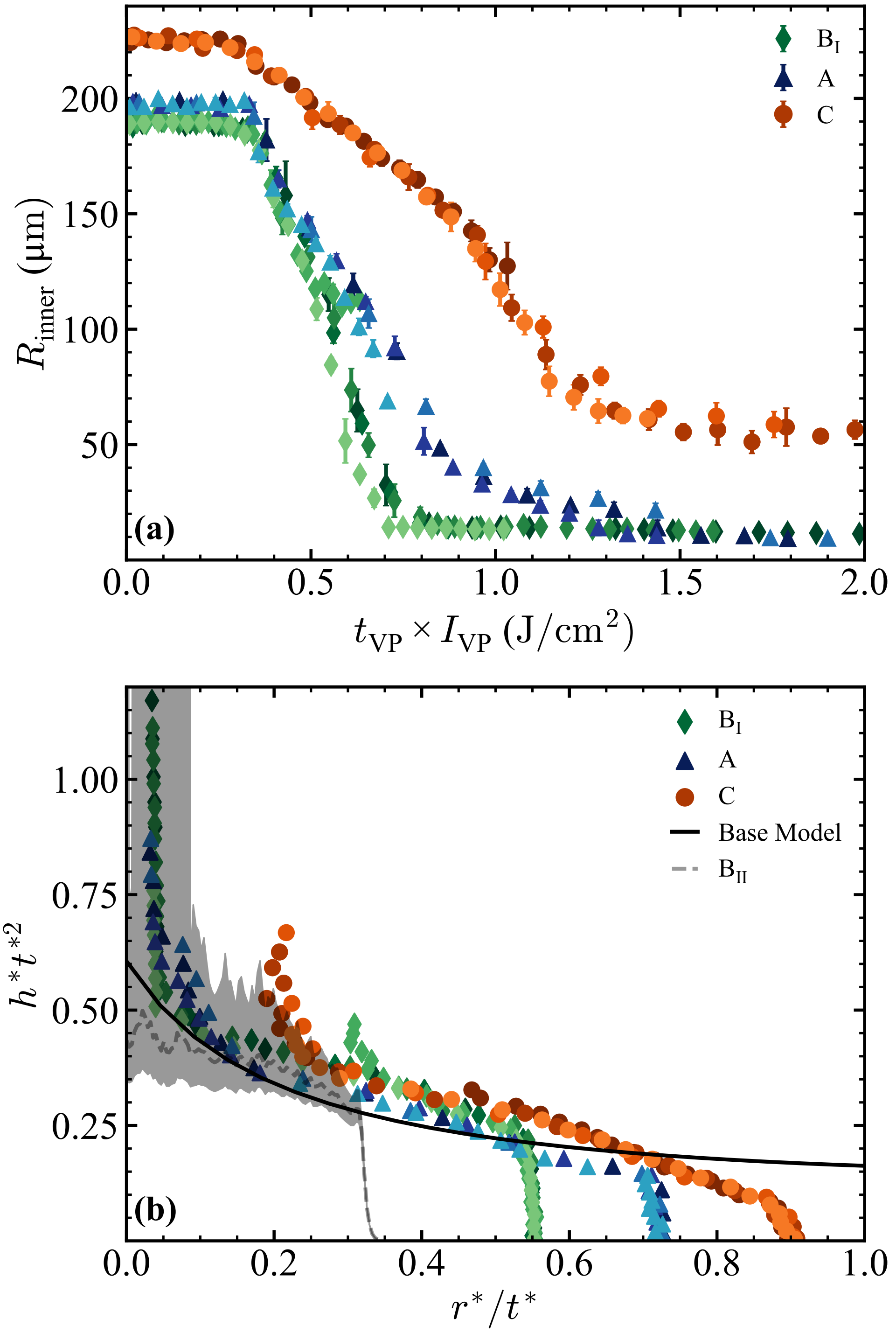

FIGURE 2.6: (a) ‘Collapse’ of the edge-tracking data for $R_{\text{inner}}$for targets B_I, A, and C [cf. Fig.2.4(c-e)] when plotted as a function of fluence $t_{\text{VP}} \times I_{\text{VP}}$. (b) Global collapse of the edge-tracking data (targets B_I, A, and C) and B_{II}data (gray data; includes an uncertainty band) in dimensionless units (see the main text). The solid black line indicates the semi-empirical thickness model of Ref. [25].

Fig. 2.6(b) presents all experimental data (including that of target B_{II} obtained using the transmission method) in non-dimensional units ($h^* t^{*2}, r^*/t^*$; cf. Section 2.3.2), with $h = t_{VP} \cdot I_{VP} \cdot d\dot{h}/dI_{VP}$ taking $d\dot{h}/dI_{VP} =$1.0(3) $10^{-7}\,\mathrm{ms}^{-1}/\mathrm{Wcm}^{-2}$. All data is found to collapse on a single curve, which underlines the validity of our approach in invoking the self-similar model in Section 2.3.2 and in the mutual agreement of the (transmission vs. edge tracking) methods employed. We may further compare our findings directly with Eq. (2.9), depicted as a black solid line in the same figure. The edge tracking curves show reasonable agreement with the self-similar solution that represents a thickness profile, indicating that the edge tracking data is a good measure to quantify the vaporization process. The collapsed data tend to lie slightly above the self-similar curve, at early times, which may indicate an overall overestimation of the mass available for the sheet (see discussion above). Alternatively, it may point towards a small overestimation of the overall vaporization rate, well within the error bars of Fig. 2.5. More noticeable deviations occur at the smallest r^*/t^* values, where the experimental data seems to vertically diverge. These deviations are due to the center mass features. Also at the largest r^*/t^* values deviations appear to occur but here we note that the self-similar model contains no edge and does not end where the sheet does. Further deviation at the larger r^*/t^* values may be attributed to finite curvature of the targets, the investigation whereof is left for future work.

2.4 Conclusion

We examine how a liquid tin target vaporizes when exposed to a 100 ns laser pulse (box-shaped in space and time). Our observations are based on stroboscopic acquisitions using an illumination pulse enabling 5 ns time resolution and 5 µm spatial resolution while scanning systematically throughout the 100 ns laser pulse. For thin (∼25 nm) and flat sheets, the absolute thickness can be obtained from the finite transmission of the backlighting through the sheet, following Liu *et al.* [25]. Our findings reveal gradual vaporization characteristics and a linear relationship between the average vaporization rate with the laser pulse intensity, i.e. $\dot{h} \propto I_{VP}$. Inspired by the fact that the observed scaling relation may be explained from simple energy balance, we construct a numerical 1-D heat and vaporization solver based on the Hertz-Knudsen equation and find excellent agreement between simulations and experimental data. A gradual vaporization mechanism would signal that nanoparticles, as observed in similarly prepared tin vapor targets [33], originate from post-vaporization clustering of atomic species. We next extend our investigations to thicker (up to approximately ∼200 nm) targets, improving on an edge-tracking method previously established by Liu *et al.* [24] in tandem with a semi-empirical sheet thickness model [25] to further quantify the vaporization dynamics. Also here the 1-D simulations are in excellent agreement with the experimental data after accounting for additional mass-loss channels. By combining the vaporization rate data from all experiments, we confirm the linearity $\dot{h} \propto I_{VP}$ with a prefactor of 1.0(3) $10^{-7}\,\mathrm{ms}^{-1}/\mathrm{Wcm}^{-2}$

over the full investigated intensity range ($0.2 \times 10^7\,\mathrm{Wcm}^{-2}$ to $4 \times 10^7\,\mathrm{Wcm}^{-2}$). We furthermore demonstrate that the amount of vaporization of liquid tin targets in the investigated laser intensity range is governed solely by the deposited fluence, across all individual targets and that the time required for vaporization follows $t_{\mathrm{vap}} \propto hI_{\mathrm{VP}}^{-1}$, validating the Ansatz proposed in Liu *et al.* [24]. Lastly, we collapse all suitably non-dimensionalized data onto the self-similar solution proposed in Ref. [25].

We thus identify the mechanism of laser-induced vaporization (as agradual vaporization governed by the Hertz-Knudsen equation) at low intensities as may be found in future advanced target preparation schemes for more efficient generation of extreme-ultraviolet light. Furthermore, we provide an accurate prediction of the vaporization rates as a function of laser intensity over an order of magnitude around $10^7\,\mathrm{Wcm}^{-2}$, which is shown to hold for all target thicknesses in a range of approximately 20 nm to 200 nm. Our work may guide and find application in the development of future EUV sources.

Acknowledgements

This work has been carried out at the Advanced Research Center for Nanolithography (ARCNL). ARCNL is a public-private partnership with founding partners UvA, VU, NWO-I, and ASML, and associate partner RUG. This research was funded by the European Research Council (ERC StG 802648). The authors thank Diko Hemminga for valuable insights into the droplet temperature after prepulse impact, and John Sheil, Michael Purvis, and Haining Wang for valuable discussions. We would also like to thank Henk-Jan Boluijt and Laurens van Buuren for their work on the experimental setup.

Appendix A: Expected target thickness profiles

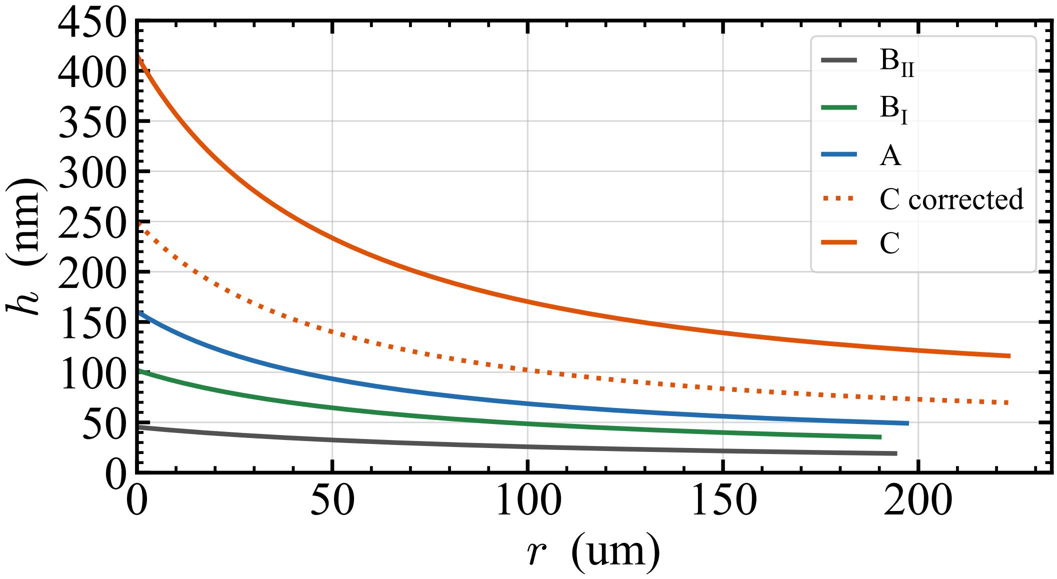

FIGURE 2.7: Thickness profiles according to semi-empirical thickness model Eq. (2.9) for the used targets, with input from Tab. 2.1 in the main text.

Fig. 2.7 depicts thickness profiles of the various tin sheet targets used in the paper, as obtained from the semi-empirical thickness model Eq. (2.9) with the required input taken from Table 2.1 in the main text. The dashed line for target C thus shows a mass correction of the target by 40 % (see the main text).

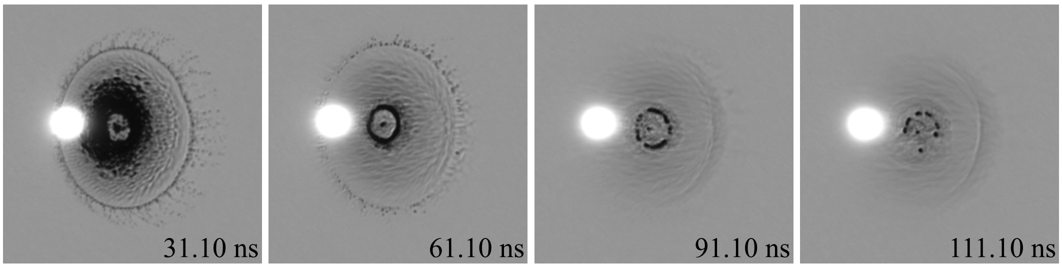

FIGURE 2.8: Shadowgraphs of target C showcasing the observed feature (see the main text) around its center mass at different stages of vaporization.

Fig. 2.8 displays target C at various stages of vaporization, highlighting an additional feature around its center mass. It shows that this feature is significantly thicker than the sheet and even the rim and center mass given that it is not vaporized even after the 100 ns-long VP. For more information about the center mass feature in general see Ref. [21].

Appendix B: Input parameters in 1-D numerical code

Table 2.2 shows the used input parameters for the 1-D numerical simulation. The initial liquid temperature of 800 K is estimated from the temperature after the end of the laser pulse in RALEF-2D radiation hydrodynamic simulations such as performed by Poirier *et al.*[51]. A sensitivity study of the model predictions is performed for all input parameters. It is found that t_{vap} is most strongly influenced by the latent heat, which also follows directly out of the energy balance (see the main text). However, the uncertainty on the latent heat is below 0.1 % according to literature, so this has a negligible effect on the simulation [54].

Parameter	Value	Source
Refractive index	3.93 + 7.87j	Highest T value of [42]
Conductivity (κ)	$43.6\,\mathrm{W/(m\,K)}$	Highest T value of [55]
Initial T	800 K	RALEF simulations
Density	$6787\,\mathrm{kg/m^3}$	Density at 800 K according to [56]
Molar mass	$0.118\,71\,\mathrm{kg/mol}$	[48]
Molar heat capacity (c_p)	$27.2\,\mathrm{J/(mol\,K)}$	Value at highest T available [57, 58]
Latent heat	$301 \times 10^3\,\mathrm{J/mol}$	[54]
Diffusivity (α)	$28.0\,\mathrm{mm^2/s}$	Calculated from $\frac{\kappa}{\rho(c_p/M)}$

TABLE 2.2: Table of input parameters used in the 1-D numerical simulation.

The next strongest sensitivity of t_{vap} is density, and thus also initial temperature, which influences the density. Again, this can be seen in the energy balance in the main text. The uncertainty on ρ itself is only ∼1 % according to a review of thirteen papers[56]. Thus, the initial temperature, and its indirect effect on ρ gives the largest uncertainty on t_{vap}. We estimate the uncertainty in the initial temperature to be approximately ∼100 K due to uncertainties in the influence of the prepulse, translating to a 3 % effect on the predicted t_{vap}. This uncertainty is significantly smaller than the uncertainty originating from the thickness estimation. Thus, the model predicted t_{vap} may considered to be rather insensitive to the input parameters. The temperature during the vaporization predicted by the model is even less sensitive to changes in the input parameters. This originates from the exponential dependence on the temperature for the vapor pressure (nominator in Eq. 2.2), meaning that only small changes in temperature are required to respond to changes in the input parameters such as ρ or latent heat. Thus, the change in temperature stays below 1 %, even for conservatively large (10 %) changes in used input parameters.

Appendix C: Edge tracking method

The edge tracking method relies on PD data of the VP exiting the vacuum chamber. Here, we assume that the geometrical obstruction created by the target, as identified via the 560 nm shadowgraphy, applies directly also to the 1064 nm VP laser light. Separately, we note that neither VP nor SP laser light is absorbed by the vapor (also see Ref. [33]). We establish a correlation between the VP laser light transmitted along the sheet (S, as measured by a PD after the chamber) and our observations of inner sheet radius (R_{inner}), which we extract from the shadowgraphs. This correlation is based on the Ansatz that the VP is spatially blocked by the remaining liquid and that the increase of the PD signal S is directly proportional to the decrease in sheet area

$$(1 - S(t_{\text{VP}})) \propto (R_{\text{inner}}(t_{\text{VP}}))^2. \tag{2.10}$$

Note that both quantities (S and R_{inner}) are normalized. Next, to define a sheet edge, a suitable threshold (T) needs to be defined. For this purpose, we perform a Gaussian fit to the background distribution counts, individually for all shadowgraphs, which allows us to determine its mean value (P_{val}) and width (P_{width}). We determine the benchmarked threshold using the relation $T = P_{\text{val}} - B_{\text{level}} \cdot P_{\text{width}}$ where we subtract a value $B_{\text{level}} \cdot P_{\text{width}}$ from P_{val} that is proportional to the background distribution width with prefactor (B_{level}). This approach enables us to effectively deal with intensity-induced speckle broadening in the illumination. Subsequently, we iteratively adjust the parameter B_{level} and, consequently, the threshold T. With each adjustment, we obtain a threshold-specific inner sheet $R_{\text{inner}}(t_{\text{VP}})$. The optimal value for B_{level} is then found by minimizing the differences between the left- and right-hand side of Eq. (2.10). In summary, we obtain a threshold such that the obtained R_{inner} best matches the transmitted VP signal.

3

Chapter 3

Laser-Induced Plasma Formation on Free-Flying Liquid Tin Sheets

H. K. Schubert, R. A. Meijer, B. Liu, D. J. Engels, O. O. Versolato

Submitted.

We investigate the spatial and temporal dynamics of plasma formed on liquid tin sheets when irradiated with a $5\,\mathrm{ns}$ laser pulse at an intensity I of several $10^8\,\mathrm{W/cm^2}$. From temporally integrated shadowgraph images of plasma emission, we deduce that there must be an intensity-specific minimum thickness at which plasma formation still occurs. Time-resolved detection of the laser light transmitted through and along the sheet reveals fast dynamics in the competition between vaporization and plasma formation. The overall dynamics are well captured in models combining preexisting scaling laws for the time to full vaporization ($\sim I^{-1}$) and the time to plasma onset ($\sim I^{-2}$). These findings are particularly relevant for target preparation and metrology in plasma light sources utilizing tin targets to produce extreme-ultraviolet (EUV) light for nanolithography applications, including metrology.

3.1 Introduction

Laser-induced plasma plays a key role in applications such as thin-film deposition and spectroscopic analysis. In pulsed laser deposition (PLD) [59, 60], high-energy laser pulses ablate a target material, generating a plasma plume that enables precise thin-film growth, critical for electronic and optical devices. Laser-induced breakdown spectroscopy (LIBS) provides real-time elemental analysis in fields ranging from geochemistry and space exploration to industrial quality control [61]. Recent advances in plasma monitoring, dual pulse laser techniques, and AI-driven diagnostics continue to refine the capabilities of laser-induced plasma technologies [62, 63]. This study investigates the plasma-formation threshold and spatial plasma dynamics on liquid tin sheets under nanosecond laser irradiation, contributing to the development of extreme ultraviolet (EUV) light sources for nanolithography. In these sources, mass-limited tin droplets serve as targets in a multipulse laser scheme [17, 18, 64, 65]. First, a nanosecond-duration prepulse (PP) accelerates the droplet to a center-of-mass speed U on the order of $100\,\mathrm{m/s}$. It simultaneously initiates a radial expansion of the droplet, forming a thin sheet with a radius on the order of 100 µm that improves the overall coupling with the following main pulse, which generates the EUV-emitting plasma.

In this work, we focus on the interaction between a vaporization pulse (VP) and the liquid tin sheets for laser intensities $I_{\mathrm{VP}} > 1 \times 10^7\,\mathrm{Wcm}^{-2}$. Previous studies have examined laser-induced vaporization of liquid tin sheets at lower laser intensities ($\sim 5 \times 10^7\,\mathrm{W/cm}^2$), below the plasma formation threshold. Such controlled laser-induced vaporization of liquid tin sheets has been shown to facilitate the formation of a low-density vapor while simultaneously revealing key features of the evolving sheet, such as a characteristic center mass and a bounding rim [24, 66, 67]. In this regime, the evaporation process is dominated by gradual Hertz–Knudsen evaporation [24, 66, 67], and the resulting low-density vapor primarily consists of atomic tin at approximately 3000 K, accompanied by nanoparticles [66]. With increasing laser intensity, plasma formation first emerges on the thicker regions of the sheet, causing a sharp increase in vapor temperature to as high as 8000 K [68]. Here, plasma formation is hypothesized to suppress nanoparticle formation, resulting in a vapor composed entirely of free atoms [68]. In addition, previous work on liquid tin microdroplets has revealed an inverse square dependence of the plasma onset time on laser intensity, when irradiated with nanosecond laser pulses for laser intensities spanning from 4×10^7 to $4 \times 10^8\,\mathrm{W/cm}^2$ [69]. This behavior has been attributed to one-dimensional heat diffusion during the irradiation process relevant for a bulk medium. No study has specifically investigated the laser-induced plasma-onset time and the spatiotemporal dynamics of plasma formation using thin sheets, where vaporization and plasma phases may coexist. This is especially interesting given that (liquid) thin sheets serve as targets for laser-produced plasma that generates EUV light in state-of-the-art nanolithography. Experimental studies on vapor-plasma phase transitions are essential for refining laser-droplet interaction models, with direct relevance to EUV source development in droplet shaping, debris mitigation, and metrology.

We investigate the spatial and temporal dynamics of plasma formation on liquid tin sheets by irradiating them during the droplet deformation process with a 5 ns laser pulse at intensities near the threshold of plasma formation. We employ an imaging system (combining bright field with shadowgraphy) to detect plasma emission and photodiodes to measure laser pulse transmission. From the imaging we observe that the extent of the sheet plasma does not continuously follow the sheet boundary throughout the deformation process, but instead reflects an intensity-specific thickness at which plasma formation occurs, before vaporization of the sheet (see Sec. 3.3.1). Photodiode traces reveal that the laser transmission exhibits a reproducible inflection point in time, dependent on laser pulse intensity and droplet deformation time (see Sec. 3.3.2). We attribute the observed inflection point to the moment when the vapor and plasma phases intersect, at a threshold thickness that is a function of laser intensity. Finally, we produce a vapor-plasma phase map using all experimental inflection time and thickness data and show agreement with a model that combines pre-existing vaporization and plasma onset scaling laws.

3.2 Experimental methods

Our experimental setup, previously described in [24, 67], employs a droplet generator to produce a kHz stream of liquid tin microdroplets traveling at a temperature of 270 °C in a vacuum environment at a base pressure of 1×10^{-7} mbar with approximately $10\,\mathrm{m\,s^{-1}}$ through a HeNe laser light sheet. The scattered HeNe signal, detected via a photomultiplier tube and downsampled to 10 Hz, triggers the experiment and synchronizes all lasers. Figure 3.1(a-c) illustrates the laser pulse scheme. We utilize a pre-pulse [PP, $\lambda = 1064\,\mathrm{nm}$, circularly polarized] to generate plasma upon interaction with the initial microdroplet, inducing an impulsive acceleration of approximately $10^{10}\,\mathrm{m/s^2}$. This rapid acceleration launches the droplet to velocities of several 100 m s, initiating a strong radial expansion and leading to the formation of a thin sheet [70]. The initial radial expansion velocity ($\dot{R}_0$, measured over the first three frames where R_0 stands for droplet radius) decreases over the capillary timescale $\tau_c = \sqrt{\rho D_0^3/6\sigma}$ due to surface tension driven sheet contraction, while the propulsion velocity (U) remains constant [22, 23, 39]. Here, $\rho = 7000\,\mathrm{kg/m^3}$ and $\sigma = 0.55\,\mathrm{N\,m^{-1}}$ represent the density and surface tension of the liquid tin, respectively, while D_0 is the initial droplet diameter. The vaporization pulse [VP, $\lambda = 1064\,\mathrm{nm}$, circularly polarized], as shown in Fig. 3.1(a), is a 5 ns Nd:YAG pulse imaged to a top-hat spot with a FWHM of 822 µm, which vaporizes the sheet and initiates plasma formation at intensities of the order $10^8\,\mathrm{W/cm^2}$. We tune I_{VP} by means of a half-wave plate followed by a polarization beam-splitting cube, positioned in front of the chamber. Spatially, the VP beam profile exhibits a standard deviation of approximately 6 % across its cross-sectional area. Temporally, the beam intensity varies with a standard deviation of less than 3 % over the pulse duration t_{VP}. The VP is larger than the sheets we probe at any time t/τ_c during droplet deformation, allowing us to analyze the VP transmission signal using photodiodes (DET025AL/M), which we installed at the entrance and exit of our measurement setup. For spectroscopic imaging, we use a dye-based illumination source (5 ns, 560 nm, temporally and spatially incoherent) in combination with CCD cameras (Manta G-145B NIR PoE) and long-distance microscopes, providing a spatial resolution of 5 µm in both front and back views [Fig. 3.1(b)]. Both cameras are equipped with a 560 nm narrow-band filter. The illumination is fixed at 100 ns after the VP [Fig. 3.1(c)] to allow some separation between the imaging of the VP-induced plasma and the liquid remnant while limiting hydrodynamic evolution (including fragmentation). Both the laser-induced plasma emission and the liquid tin remnants are captured because the camera exposure time is significantly longer (on the order of µs) than the 100 ns separation between VP and SP. The VP is scanned in $\Delta t = 60\,\mathrm{ns}$ steps with respect to the PP. At each delay step, 20 frames are captured using stroboscopic imaging. We attribute visible light emission

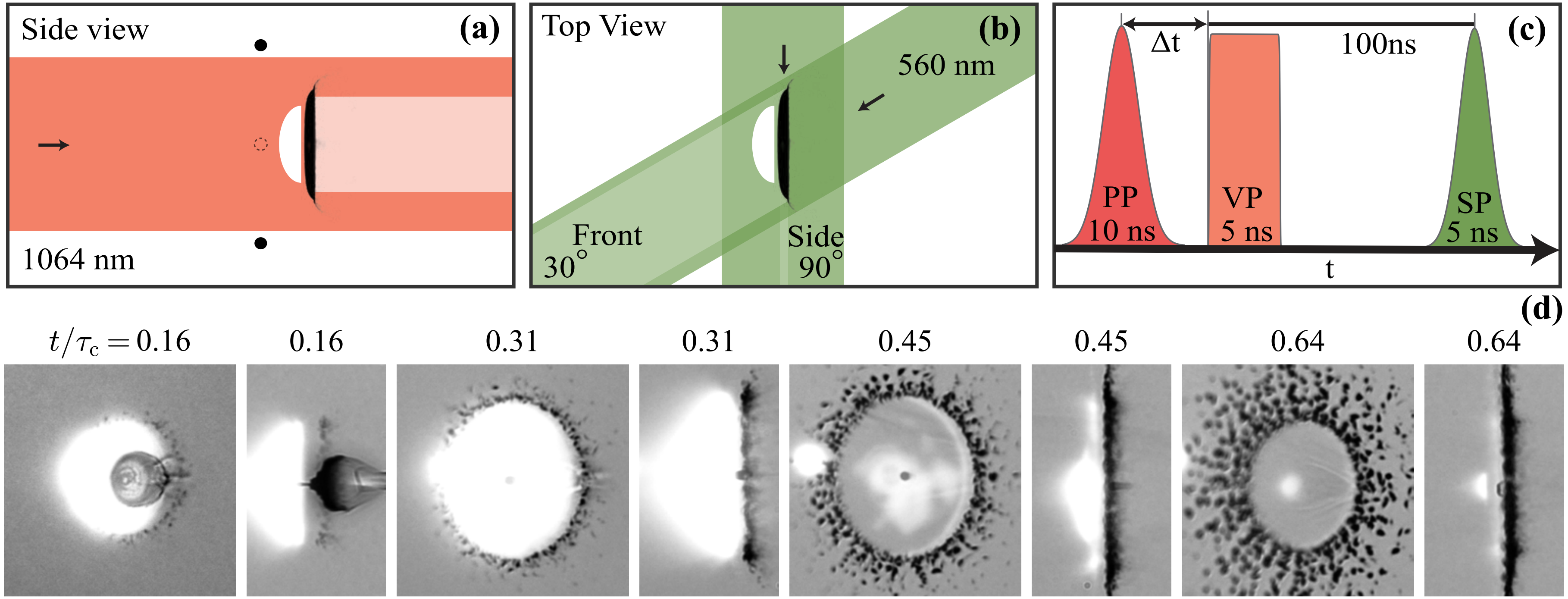

FIGURE 3.1: (a-c) Schematic of the experiments, laser pulse schemes with irradiation geometries and timings shown. (a) Side-view schematic of the vaporization pulse (VP) irradiating the liquid tin sheet. (b) Top-view schematic of the illumination setup. (c) Timing of the shadowgraphy pulse (SP). The VP is scanned in time after Δt, with the SP follows the VP at 100 ns. (d) Series of shadowgraphs showing alternating views of sheet residue and laser-induced plasma emission in front-view (left) and side-view (right) at various times t/τ_c during droplet deformation following VP irradiation with $I_{VP} = 4.7 \times 10^7\,\mathrm{W cm^{-2}}$. The small bright spot on the left side of the front-view image, especially visible at $t/\tau_c = 0.45$, originates from PP plasma emission.

as the primary indicator for plasma formation, consistent with prior studies [69], and refer to it in the following simply as *plasma*.

To quantify the radial extent of the sheet plasma, we define a threshold to binarize the image accordingly. A plasma pixel is defined as a pixel within the top percentile of all pixel values between the maximum pixel value and the mean of the background. The threshold is individually set for each I_{VP} scan to best capture the sheet plasma extent during the expansion phase, which closely follows the evolution of the liquid sheet. In addition, we apply image-processing techniques to distinctively track the radius of sheet plasma and not the rim plasma (see Measurements). The shadowgraphs, shown alternately in front and side-views [Fig. 3.1(d)], capture the sheet and its plasma at various stages of droplet deformation. The front-view shadowgraphs highlight that minor (aforementioned 6 % standard deviation) spatial imperfections in the beam profile translate to visible differences in plasma light emission, highlighting the non-linear behavior at plasma threshold. In contrast, side-view shadowgraphs are less sensitive to beam profile imperfections as a result of their line-of-sight integration over a larger portion of the beam. For radial quantification, we exclusively use side-view shadowgraphs, which offer longer plasma columns and higher brightness compared to the front view; the corresponding results are discussed in Sec. 3.3.1. Furthermore, we measure VP transmission using photodiodes, which provide a radially integrated signal that is largely insensitive to minor beam inhomogeneities; these results are presented in Sect. 3.3.2.

3.3 Measurements

3.3.1 Imaging of plasma emission

From the shadowgraphs in Fig. 3.1(d), we observe that the laser-induced sheet does not always form over the full sheet during the target deformation process. We note that the sheet expansion has been studied in detail previously (e.g. see Refs. [23, 25, 53]), and in the current work we solely focus on the plasma produced from the sheets. For the given I_{VP}, the radial extent of the sheet plasma initially follows the sheet's expansion, as seen for $t/\tau_c \leq 0.31$. In this early phase, plasma spans the entire sheet, which we define as the *bulk* regime. Here, the sheet is sufficiently thick that irradiation by the VP leads to plasma formation, consistent with observations in previous laser-droplet interaction studies [69]. At later times ($t/\tau_c = 0.64$), plasma formation becomes confined to the sheet's thicker center and rim of the sheets, whereas the remainder of the sheet vaporizes without producing visible laser-produced plasma. We refer to this condition as the *thin film* regime, as studied in Ref. [24, 67]. Between these two regimes, there is the *intermediate* regime, illustrated by the shadowgraph at $t/\tau_c = 0.44$ in Fig. 3.1(d). In this regime, plasma emission is partially observed around the sheet center and the rim of the sheet, whereas the outer, thinner sheet regions atomize without contributing to plasma formation.

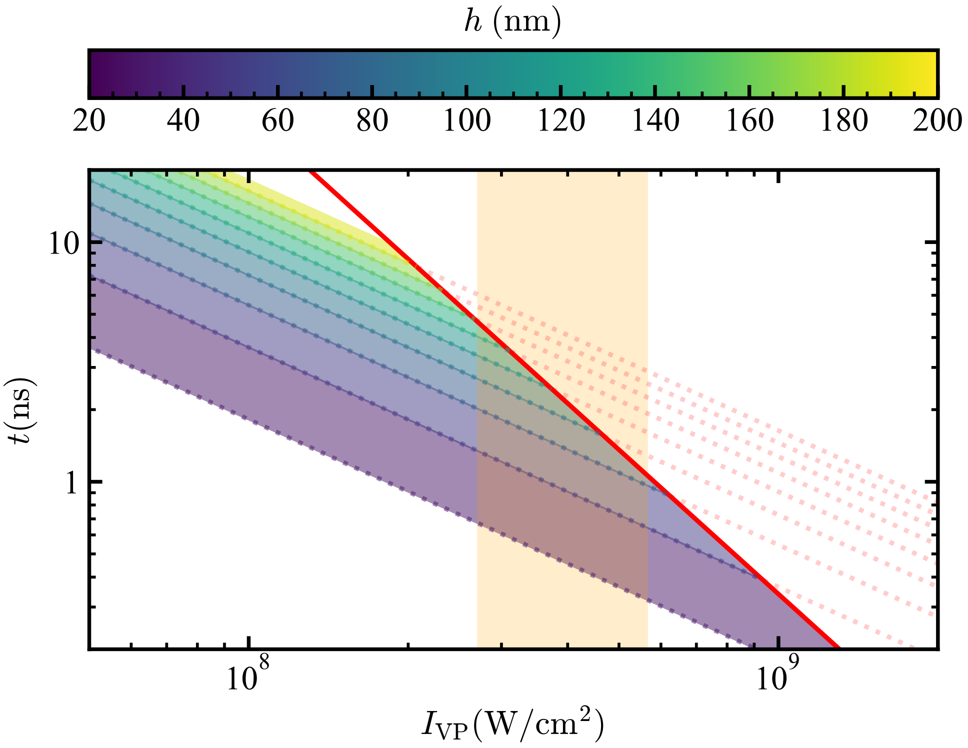

FIGURE 3.2: Vaporization time $t_{\mathrm{VP}} \propto I_{\mathrm{VP}}^{-1}$ (Eq. 3.1), for different initial local thicknesses (indicated by the color bar). The plasma onset time $t_{\mathrm{on}} \propto I_{\mathrm{VP}}^{-2}$ (Eq. 3.2) is shown in red. The shaded yellow region highlights the experimental measurement range.

It is important to note that the shadowgraphy observations of the sheet plasma are time-integrated over the VP duration (5 ns), as the camera exposure time is significantly longer (µs). The shadowgraphs therefore show only the integrated result of the emission. At any stage of the droplet deformation process, the sheet exhibits a radially decreasing thickness profile and progressively thins over time [25]. We observe that the sheet-plasma radius initially follows the sheet expansion (*bulk* regime) but at some point decreases rapidly (*intermediate* regime). This suggests the existence of an intensity-dependent minimum sheet thickness required for plasma formation, as we argue in the following.

From previous studies, the time required for vaporization of a *thin film* is known to scale as

$$t_{\mathrm{VP}} = \frac{h(r)}{A \times I_{\mathrm{VP}}}, \tag{3.1}$$

where $h(r)$ denotes the local sheet thickness, $A = 1.0(3) \times 10^{-7}\,\mathrm{ms^{-1}/Wcm^{-2}}$ is a proportionality constant obtained by fitting, and I_{VP} is the laser intensity [67]. Physically, A reflects the balance between the laser energy deposited and the energy required for vaporization, and may be estimated by evaluating the energy required to vaporize a unit volume of tin $\rho H/M$, where ρ is the density, H is the latent heat and M is the molar mass. Assuming a 20 % absorption coefficient, Schubert et al. [67] estimated the prefactor $1.2 \times 10^{-7}\,\mathrm{ms^{-1}/Wcm^{-2}}$ close to the original fit result [67]. Figure 3.2 illustrates how the time to full (local) vaporization t_{VP} scales with intensity I_{VP} with a prefactor set by the initial (local) thickness.

In contrast, the onset of plasma formation in a *bulk* medium is known to follow

$$t_{\mathrm{on}} = B \times I_{\mathrm{VP}}^{-2}, \tag{3.2}$$

where $B = 3.4(5) \times 10^{-8}\,\mathrm{sW^2/cm^4}$ is a proportionality constant obtained from fitting [69]. Physically, B represents 1-D laser heat diffusion following energy deposition within the thermal absorption layer, and may be estimated (see Ref. [69] for details) from evaluating the energy required to reach a pulse length dependent threshold fluence $\rho H \sqrt{\kappa\tau}/M$, where κ is the thermal diffusivity and τ the laser pulse length. Assuming a 16 % absorption coefficient, Meijer et. al [71] estimated a prefactor $B = 4.4 \times 10^{-8}\,\mathrm{sW^2/cm^4}$ in reasonable agreement with the original fit result [69]. Figure 3.2 illustrates how the time to plasma onset t_{on} scales with intensity I_{VP} with a prefactor that is independent of the local thickness.

In the *intermediate* regime, both vaporization and plasma coexist, depending on the local thickness (cf. Fig. 3.1(d) at $t/\tau_c = 0.44$). For a given I_{VP} both models intersect when $t_{\mathrm{VP}} = t_{\mathrm{on}}$ at a thickness

$$h^* = \frac{A \times B}{I_{\mathrm{VP}}}. \tag{3.3}$$

Beyond this thickness, gradual vaporization transitions into plasma formation. However, we emphasize that this intersection point Eq. 3.3 serves only as an upper limit given that, as the sheet thins, the surface temperature will rise faster than in the bulk case and t_{on} will shift to earlier times. Consequently, Eq. 3.3 should also be interpreted as an upper bound, and the intensity scaling exponent α of t_{on} will deviate from the value $\alpha = -2$ (ranging $-2 < \alpha < -1$ with -1 returning the thin sheet limit).

Returning to the shadowgraphs in Fig. 3.1(d), we find two further distinct features that exhibit plasma formation. The first feature is the rim (and associated ligaments and ligament-fragments), which bounds the sheet [25]. Hydrodynamic arguments predict that its diameter is on the order of 1 µm in diameter [25]. The second feature is the center mass [72], also with a thickness of a few µm. These regions are significantly thicker than the sheet and exceed the necessary threshold h^*. We also observe that the fragments ejected by the rim ligaments appear larger at later times (100 ns) due to the combined effects of fragment size increasing with time [72] and partial vaporization leading to expanded dense, partially opaque vapor surrounding the fragments. From hereon, we focus our studies on the central sheet that presents a window on the intermediate regime, and track the lateral plasma size (cf. §3.2) over time.

In Fig. 3.3(a), we plot $\Delta R_{\mathrm{p}} = R_{\mathrm{p}} - R_{\mathrm{exp}}$, where ΔR_{p} is the difference between

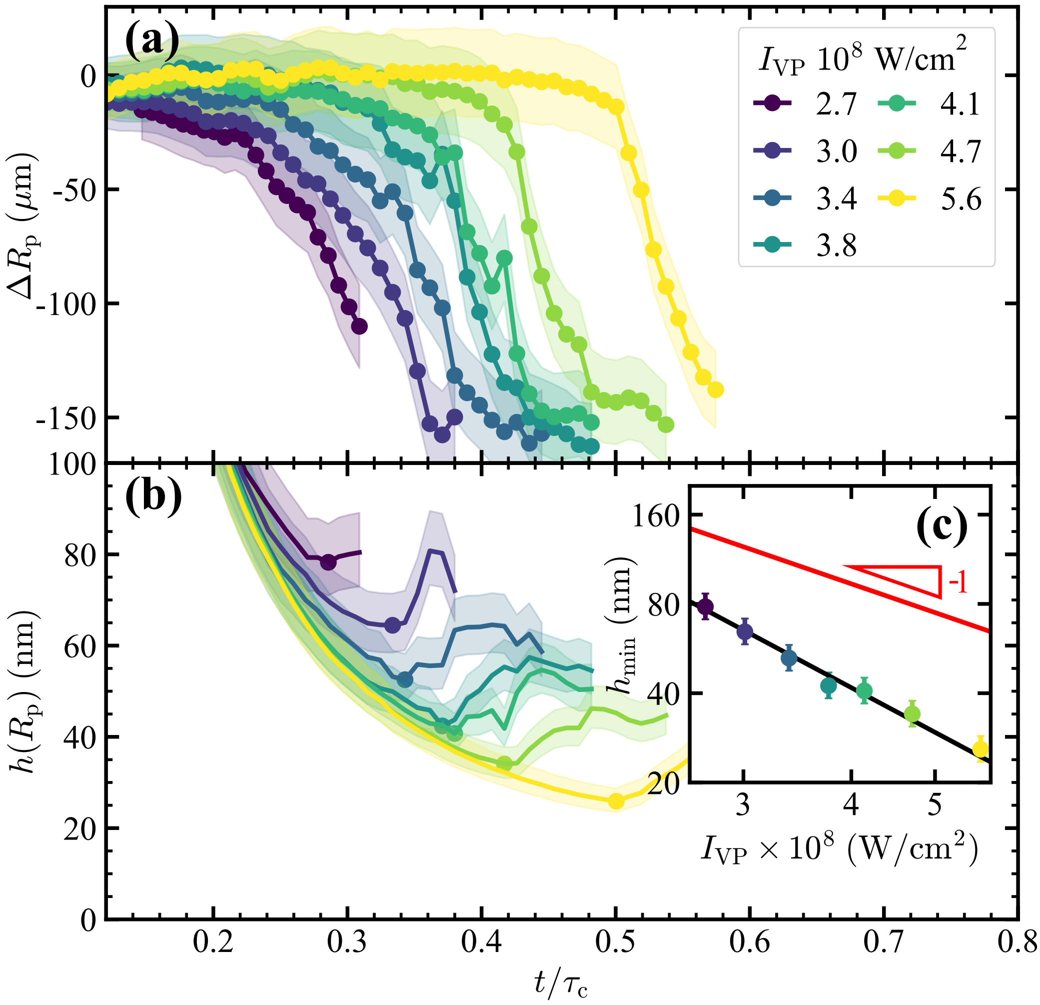

FIGURE 3.3: (a) Difference plasma radius ΔR_p for various I_{VP}. (b) Sheet thickness at the plasma emission radius R_p during expansion for various I_{VP}. (c) Minimum sheet thickness identified in (b) as a function of I_{VP}; the red line presents the threshold thickness h^* (see Eq. 3.3).

the lateral extent of the plasma R_p and the radius of the liquid sheet R_{exp}. We observe that the VP-induced sheet plasma radius initially closely follows the sheet expansion trajectory (that is, $\Delta R_p \approx 0$) before deviating at an intensity-dependent time. For higher I_{VP}, the contraction of ΔR_p occurs later and more abruptly. In Fig. 3.3(b), we present the sheet thickness at R_p using the semi-empirical model by Liu *et al.* [25], developed for laser-shaped tin targets. This model was inspired by the self-similar solution by Wang *et al.* [53] for the case of water-pillar impact. Using this model of Liu *et al.* [25] to calculate the sheet thickness leads to the observation that, for each I_{VP}, there is a minimum thickness below which the sheet plasma is no longer observed. In both panels Fig. 3.3(a,b), the error bars on ΔR_p and $h(R_p)$ represent uncertainties from radial sheet plasma tracking ($\pm 10\,\%$) in (a) and an additional uncertainty from thickness estimation due to the input parameter $\dot{R}_0$ ($\pm 5\,\%$) in (b), see Ref. [25]. In Fig. 3.3(c), we plot the minimum thickness h_{min} at which plasma is observed as a function of I_{VP} and find that it decreases with increasing I_{VP} in line with expectation cf. Eq. (3.3).

The h_{min} in Fig. 3.3(c) extracted from (b) follows a somewhat steeper slope than predicted with Eq. 3.3 for h^*, and lies systematically below it.

Overall, we observe reasonable agreement between the experiment and our model without performing any fit. This agreement is in fact surprising given the experimental limitations and the strongly simplified model, even more so given the fact that R_{p} is here determined from shadowgraph images that necessarily integrate the plasma emission over the full VP duration and thus is blind to any dynamics on the VP time scale.

3.3.2 Time-resolved laser transmission

To gain deeper insight, we next examine the temporal dynamics of the interaction between the VP and the liquid tin sheets using photodiode (PD) measurements of the VP beam that is transmitted past the tin sheet (cf. §3.2). To process the transmission PD data, we first apply an offset correction to all traces, then average the traces for each delay t/τ_{c}, and finally normalize all data. For the normalization we use, for each measurement independently, an early-time reference PD trace measured prior to the PP–droplet interaction. These reference traces correspond to negative time values, where there is only negligible ($\approx 0.1\%$) geometrical overlap between the VP and the unexpanded droplet. Fig. 3.4 shows a heatmap of the measured VP transmission (z-axis) as a function of the droplet deformation time t/τ_{c} (x-axis) and VP duration t_{VP} (y-axis) for $I_{\mathrm{VP}} = 4.7 \times 10^7\,\mathrm{W cm^{-2}}$. For better visibility, the color scale is limited to the range 65 to 100 %. This range is appropriate because the VP beam (diameter 822 µm) always partially bypasses the expanding sheet, resulting in an offset in the transmission dynamics. The PD signal at $t/\tau_{\mathrm{c}} = 0$, when the VP impacts the droplet simultaneously with the PP, shows a noticeable dip compared to one earlier and one later timestep, highlighting the effect from PP-induced plasma formation on the droplet, which causes absorption of the VP (via inverse Bremsstrahlung). Next, for $0 < t/\tau_{\mathrm{c}} < 0.1$, the PD signal gradually decreases in amplitude but remains approximately constant over the duration of the VP. We attribute the gradual decrease in VP transmission (at any t_{VP}) with t/τ_{c} to the liquid tin sheet's expansion: as the sheet expands, it spans a larger cross-sectional area within the VP beam, thereby reducing the transmitted signal.

Focusing next on $t_{\mathrm{VP}} = 0.5$, the gradual decrease with increasing t/τ_{c} is fully explained by this increasing geometrical liquid-sheet cross section. At larger t_{VP}, the same holds up to the white line that visually highlights (as a visual guide) the shrinking of the geometrical liquid-sheet cross section due to vaporization. This white line moves to higher t_{VP} for decreasing t/τ_{c} as for thicker sheets (earlier times t/τ_{c}) shrinking starts later in the VP given more vaporization is required. We plot the white line up to $t_{\mathrm{VP}} \approx 1.5\,\mathrm{ns}$ (indicated by the transparent band that takes into account the timing uncertainty inherent to the measurements), where the bulk plasma threshold is reached cf.

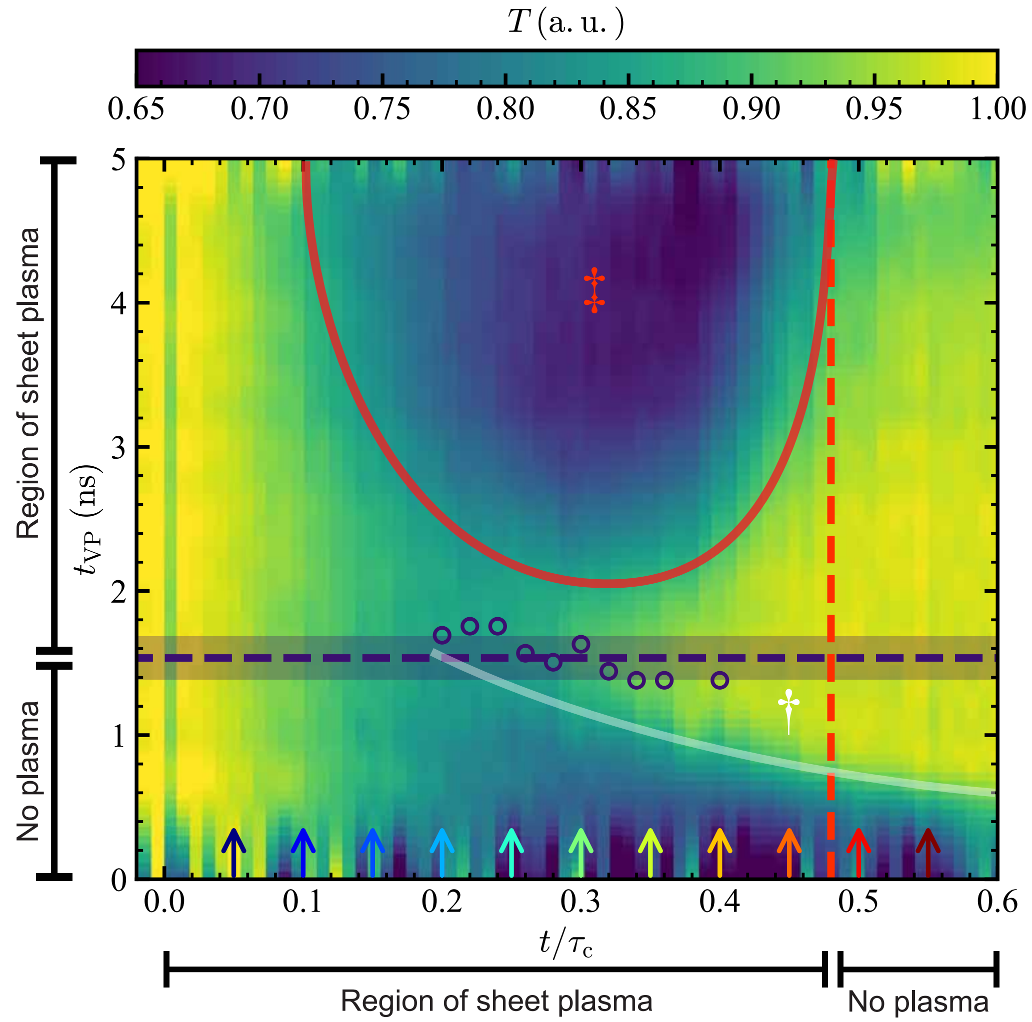

FIGURE 3.4: Heatmap of photodiode transmission (color axis) during the 5-ns long VP irradiation, for a fixed intensity ($I_{\mathrm{VP}} = 4.7 \times 10^{8}\,\mathrm{W/cm^{2}}$), plotted over normalized droplet deformation time t/τ_{c} (x-axis) and VP duration t_{VP} (y-axis). The horizontal dashed line marks the onset of plasma formation based on Eq. 3.2 and is accompanied by a shaded band indicating the ±150 ps systematic uncertainty in t. The hollow markers denote the transmission maxima for selected t/τ_{c}. The red dashed vertical line marks the last timestep at which plasma is observed via shadowgraphy. The region above the white line † corresponds to increased transmission due to vaporization of the sheets' thinner outer regions. The region outlined by the red solid line ‡ highlights a sharp drop in transmission, attributed to plasma formation. Colored arrows along the bottom denote time line-outs used in Fig. 3.5. Regions labeled "Region of sheet plasma" and "No plasma" summarize plasma presence as inferred from photodiode data (vertical axis) and shadowgraphy (horizontal axis, cf. Fig. 3.1), respectively.

Eq. 3.2. We attribute the drop in transmission for larger $t_{\mathrm{VP}} > 1.5\,\mathrm{ns}$ (specifically in the region enclosed by the red solid line, again as a visual guide) to plasma formation, decreasing transmission. We mark the moment of transmission drop in the photodiode (PD) signal at intermediate values t/τ_c (open purple markers). We note that the observed transmission drop due to plasma formation could result from inverse Bremsstrahlung absorption of VP, and, in part, from lensing by plasma gradients. In addition to geometric blockage by plasma formation, dense fragment clouds could contribute to attenuation, particularly at later times $t/\tau_c > 0.5$, when the number of droplets within the vaporization pulse (VP) beam, as well as the diameter and size of the fragment rim, increases with t/τ_c [72]. The plasma formation region enclosed by the red solid line is bounded on the right by $t/\tau_c \approx 0.45$ at which point the entire sheet is too thin to support plasma formation. The region is limited on the left by the merging of the red and white vaporization lines; however, at this point, the signal-to-noise ratio no longer supports identifying a maximum in transmission.

Importantly, we observe a distinct inflection point in the photodiode (PD) signal only when plasma light emission is visible at the sheet position in the shadowgraph images. We therefore label the regions “Region of sheet plasma” and “No plasma” to indicate the inferred presence of plasma, based on photodiode data (vertical axis) and shadowgraphy observations (horizontal axis; see Fig. 3.1),

To make a quantitative connection with the shadowgraph frames (and the data in Fig. 3.3), we extract a *plasma* radius R_p by converting the transmission signal to a *blocking* radius R_B. This heuristic conversion is based on the simple Ansatz of a circular top-hat beam and a circular blocking element of radius R_B that geometrically blocks the light from reaching the PD. The conversion is based on the linear relation between the PD signal and the beam area transmitted A_T, which is given by $A_T = \mathrm{PD} \times A_{\mathrm{beam}}$. The corresponding blocked beam area A_B is then $A_B = A_{\mathrm{beam}} - A_T$. From this, we determine the blocking radius R_B as

$$R_B = \sqrt{\frac{A_B}{\pi}} = \sqrt{R_{\mathrm{beam}}^2 \times (1 - \mathrm{PD})} \tag{3.4}$$

and, in line with the previous section, we focus on the difference radius $\Delta R_B = R_B - R_{\mathrm{exp}}$. Figure 3.5(a) shows ΔR_B as a function of t_{VP} for selected droplet deformation times t/τ_c [cf. vertical arrows in Fig. 3.4]. The shaded region indicates the uncertainty in R_B, resulting from an estimated uncertainty 5 % in determining R_{beam}. We find that R_B follows the shadowgraph-inferred sheet radius during early times of t_{VP} aside from overestimating the sheet radius by up to 15 % at the early times ($< 1\,\mathrm{ns}$), which we attribute to the exclusion of fine structures and ligaments in the shadowgraph analysis (where we track the rim), features that contribute to geometric blocking and R_B. Thus, the interpretation of R_B should be made with care, given that the Ansatz of a single circular blocking element represents a strong simplification. To avoid bandwidth limitations and other electronic artifacts, our

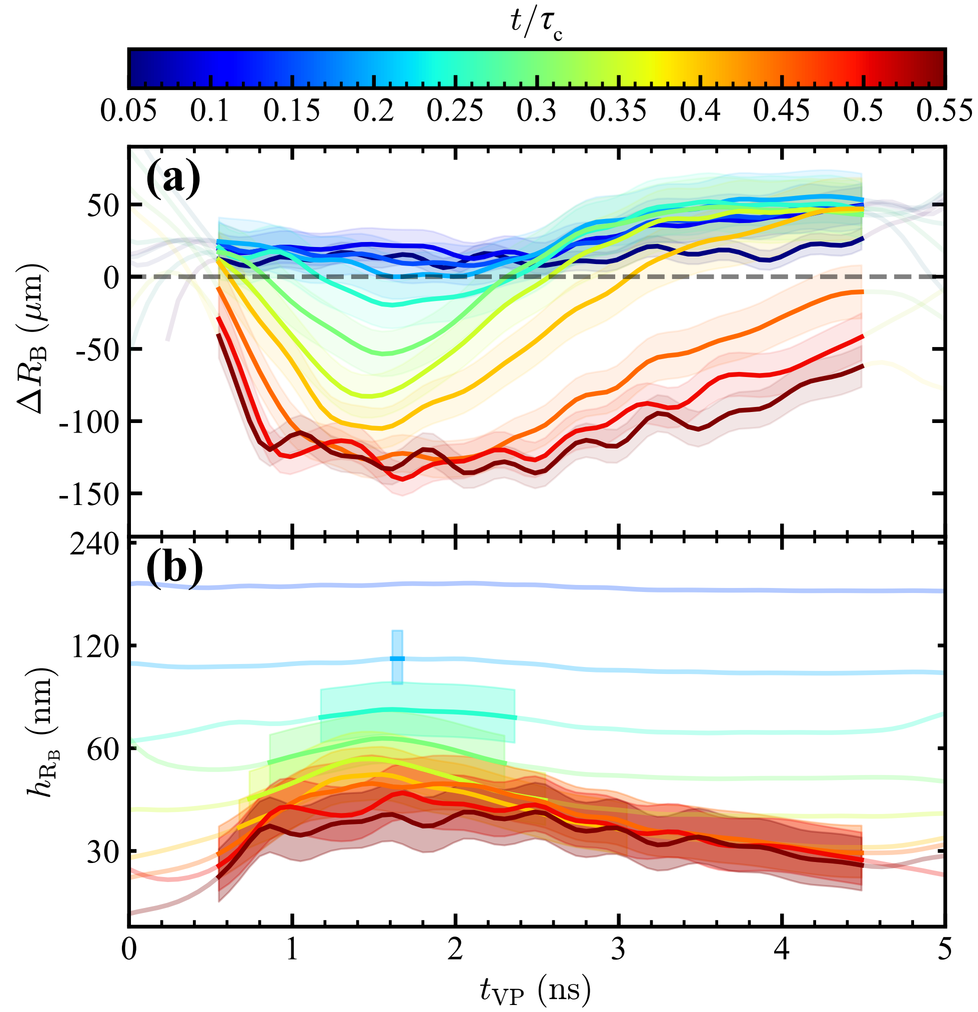

FIGURE 3.5: (a) Difference blocking radius ΔR_B as a function of t_{VP} for selected time steps t/τ_c for $I_{VP} = 4.7 \times 10^7\,\mathrm{Wcm}^{-2}$. (b) Sheet thickness at R_B as a function of t_{VP}. Only $R_B < R_{sheet}$ can yield physically relevant values for the thickness; non-physical regions $R_B > R_{sheet}$ are faded.

quantitative PD analysis is restricted to the interval between 0.5 and 4.5 ns. Soon after the onset of VP, ΔR_B shrinks to an inflection point, after which it increases again. This dynamic becomes more pronounced for later time t/τ_c. We observe that ΔR_B levels off at positive values at the end of the VP, indicating $R_B > R_{sheet}$. The observation of the PD data in terms of ΔR_B makes clear that the time-integrated plasma emission shadowgraphs hide a rich fast dynamic [compare Fig. 3.3(a) and 3.5(a)]: gradual vaporization reduces ΔR_B until the plasma sparks on thicker regions underlying the increase in ΔR_B. In our interpretation of a blocking radius, the fast dynamics of the increase in ΔR_B corresponds to an expansion speed of several tens to 100 µm/ns. Such high speeds have been predicted by simulations [73] on ionization waves propagating through subcritical tin vapor. Laser-induced ionization waves in gases such as air and argon have been experimentally observed to propagate at similarly high supersonic speeds (10 −30 µm/ns) [74].

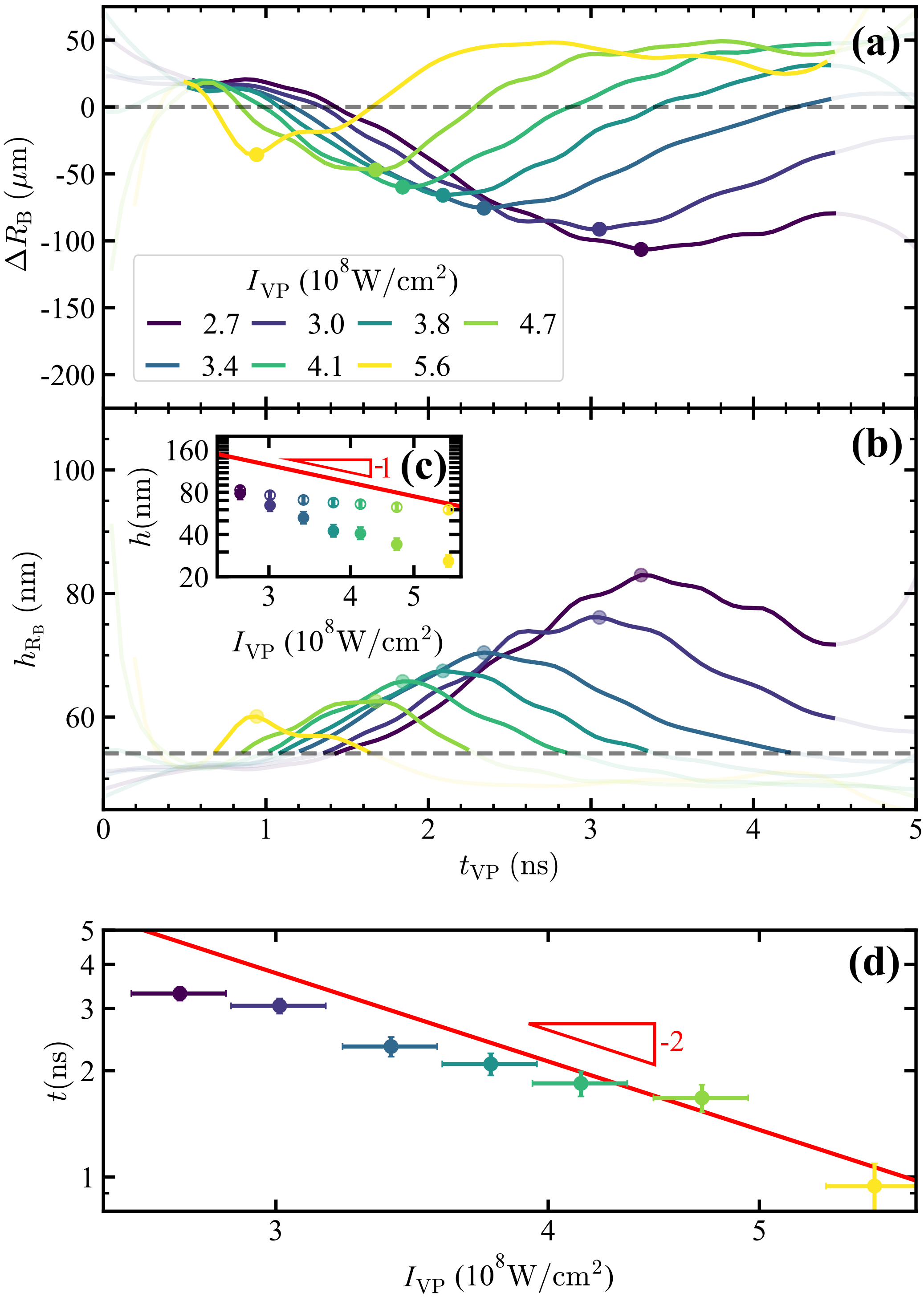

FIGURE 3.6: (a) Difference blocking radius ΔR_B as a function of the VP timescale t_{VP} at $t/\tau_c = 0.3$ for multiple I_{VP}. (b) Sheet thickness h at the blocking radius R_B at $t/\tau_c = 0.3$. (c) Thickness at inflection point as a function of I_{VP} (open circles); data from Fig. 3.3(c) is also shown for comparison (closed circles) and the red line is the threshold thickness h^* see Eq. 3.3. (d) Time of inflection as a function of I_{VP} with the plasma onset time t_{on} see Eq. 3.2.

We attribute the observed inflection points in Fig. 3.6(a) [cf. open circles in Fig. 3.5] to the moments when the vapor and plasma phases intersect at a threshold thickness h^*. Given that the sheet thins over time t/τ_c, h^* is found at ever larger ΔR_B.

In Fig. 3.5(b), we next present the thickness calculated at the blocking radius as a function of t_{VP} for the same selected droplet deformation times t/τ_c. The shaded region indicates the uncertainty in h_{R_B}, arising from an estimated 10 % uncertainty in the radial expansion speed $\dot{R}_0$ and a 5 % uncertainty in R_B. Note that nonphysical thicknesses corresponding to values R_B larger than the liquid tin sheet are faded but remain calculable from the thickness model [25]. We observe that the thickness at the inflection point progressively decreases between 0.2 and 0.6 t/τ_c from approximately 120 to 30 nm at which point it appears to level out: no significant change in thickness (at the inflection point) is observed for $t/\tau_c > 0.3$–0.4. We interpret this "converged" thickness, far away from nonphysical interpretation near the sheet edge, as the relevant estimator for h^*.

We next extract the *difference* blocking radius ΔR_B and the corresponding thickness at R_B at a common time $t/\tau_c = 0.3$ for all measured I_{VP}, as presented in Fig. 3.6 (we refer to Fig. 3.8 in the Appendix for the underlying heatmaps). We select the delay step 0.3 t/τ_c because it consistently captures both the initial rise and subsequent drop in the PD signal throughout the investigated range I_{VP} (see Fig. 3.8) although it lies at the limit of the converged thickness range, overestimating h^*.

Fig. 3.6(a) presents ΔR_B as a function of I_{VP} for the selected $t/\tau_c = 0.3$. We observe that for all I_{VP}, ΔR_B exhibits an inflection point t_i that occurs earlier and at larger ΔR_B for higher I_{VP}. We also compute the thickness at R_B for each I_{VP} in Fig. 3.6(b) following the same procedure as before, and find that the thickness of the inflection point h_i decreases with increasing I_{VP}, in line with expectations cf. Eq. 3.3. We find closer agreement between the time-resolved approach to obtain h_i (open markers) and the predictions (red line) than in the case of time-integrated plasma emission data cf. Fig. 3.3(c, filled markers), although the intensity scaling is not in close agreement. This difference in scaling may be because, again, Eq. 3.3 should be interpreted as an upper limit and that its intensity scaling exponent α of t_{on} will differ from the value $\alpha = -2$ (to the range $-2 < \alpha < -1$). A value of this exponent in this range can bring the observed scaling back into agreement. To avoid dependence on the inferred thickness h_i and the related assumptions and systematic errors, we instead focus on the time of inflection, shown in Fig. 3.6(d). We attribute an uncertainty of 5 % in the measured I_{VP}, which is represented as the x-axis error, and an uncertainty of ±150 ps in t_i, corresponding to the specified rise time of the photodiode. These data are close to the plasma onset time predicted by Eq. 3.2, within experimental uncertainty. However, again, a difference in the scaling exponent may be observed, consistent with that of h_i.

Finally, in Fig. 3.7 we populate the diagram cf. Fig. 3.2 with experimental

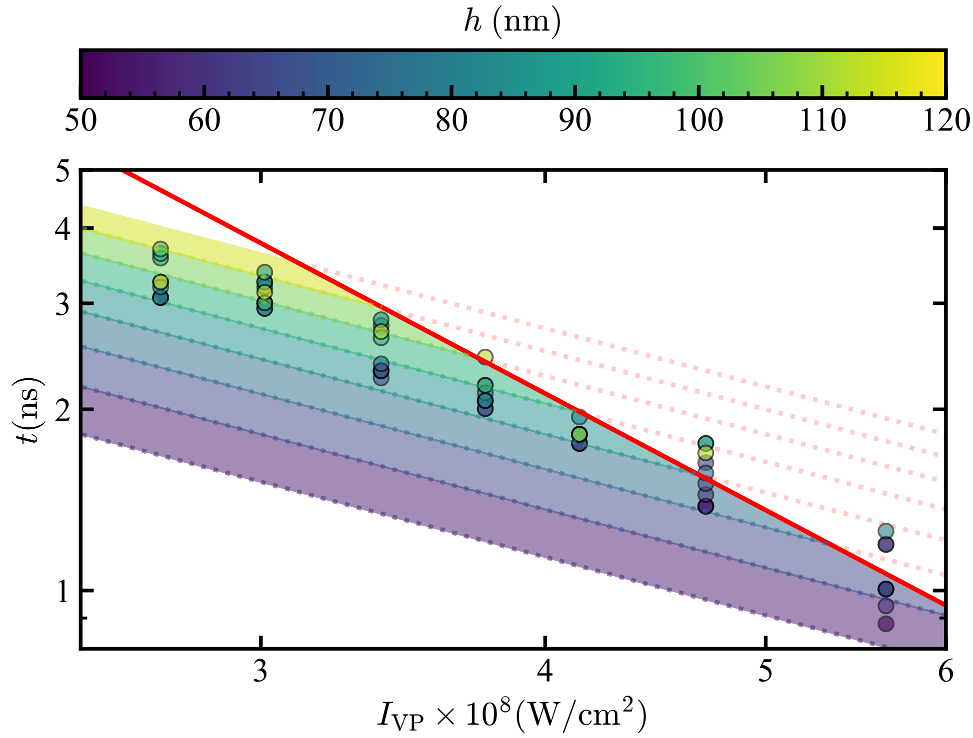

FIGURE 3.7: Zoomed-in view (cf. Fig. 3.1) and comparison with experimental data on vaporization time, where $t_{\mathrm{VP}} \propto I_{\mathrm{VP}}^{-1}$ (see Eq. 3.1), for various initial thicknesses (indicated by the color bar). The plasma onset time, $t_{\mathrm{on}} \propto I_{\mathrm{VP}}^{-2}$ (Eq. 3.2), is shown in red. Experimental data for the inflection time and corresponding thickness are indicated by markers, with their color representing the inflection thickness as given by the color bar.

data. The experimental points are extracted by examining the times between 0.2 and 0.4 t/τ_c in the steps of 0.02 t/τ_c. In each time step, we extract the inflection time t_i and threshold thickness h_i, and plot them for all I_{VP} values. The comparison between the experimental data and the theory shows good agreement between the investigated range and times I_{VP}. We observe that at lower I_{VP}, t_i is systematically slightly lower than the theoretical prediction, again in line with the interpretation of Eq. 3.2 as an upper limit and its power exponent to differ from -2. Overall, we find reasonable agreement between the model prediction and the time-resolved experimental data, where again no fit was performed and instead fundamental data from previous work (specifically parameters A, B) were combined to predict the threshold behavior in the intermediate case of interfacing bulk and thin film regimes.

3.4 Conclusion

In this study, we investigate the spatial and temporal dynamics of plasma formation on liquid tin sheets by irradiating them during the droplet deformation process with a 5 ns vaporization laser pulse featuring a spatial and temporal box profile. For intensities around $I_{\mathrm{VP}} \sim 10^7\,\mathrm{Wcm^{-2}}$, we observe plasma formation on sheets during the target deformation process. We employ imaging to detect plasma emission and photodiodes to measure laser pulse transmission past the sheet. The temporally integrated shadowgraphy frames reveal that the extent of the sheet plasma does not continuously follow the liquid tin sheet boundary during deformation. Instead, it corresponds to an intensity-dependent thickness threshold: plasma formation occurs at thicker, more central sheet regions, whereas full local vaporization occurs in thinner, outer regions. Photodiode traces reveal that during the 5 ns VP, the laser transmission exhibits an inflection point, characterized by a distinct decrease in transmission following an initial rise, indicating an intensity-specific onset time within the duration of the VP pulse. We attribute the observed inflection point to the moment when the vapor and plasma phases intersect. We hypothesize that plasma formation on the tin sheet begins at its center, following the bulk plasma onset time $\sim 1/I_{\mathrm{VP}}^2$). Subsequently, our interpretation of a single blocking radius indicates that the plasma propagates radially outward. However, experimental limitations (including the strong simplification in assuming a single circular blocking geometry) and uncertainty in accurately determining a unique threshold thickness lead us to mainly keep the focus on the time of inflection. Future work may include time-resolved imaging of plasma light emission to further study the physical origins of the transmission dynamics. Time-resolved imaging the transmitted VP (with a controlled numerical aperture) would possibly enable identifying plasma lensing effects.

Finally, we produce a phase map using all experimental inflection time and thickness data and show reasonable agreement with a model that combines preexisting scaling laws governing vaporization time (which scales as $\sim 1/I_{\mathrm{VP}}$) and plasma onset time ($\sim 1/I_{\mathrm{VP}}^2$). These findings are particularly relevant for target preparation and metrology in extreme-ultraviolet (EUV) light sources utilizing tin microdroplets.

Acknowledgments

This work was carried out at the Advanced Research Center for Nanolithography (ARCNL). ARCNL is a public-private partnership with founding partners UvA, VU, NWO-I, and ASML, and associate partner UG. This research was funded by the European Research Council (ERC StG 802648). The authors thank Haining Wang and Jorge Gonzalez for valuable discussions, and Henk-Jan Boluijt and Laurens van Buuren for their work on the experimental setup.

Appendix: Heatmaps

Figure 3.8 shows the heatmaps of the VP transmission [cf. Fig. 3.4] for various I_{VP}. These data underlie Figs. 3.6 and 3.5 in the main text.

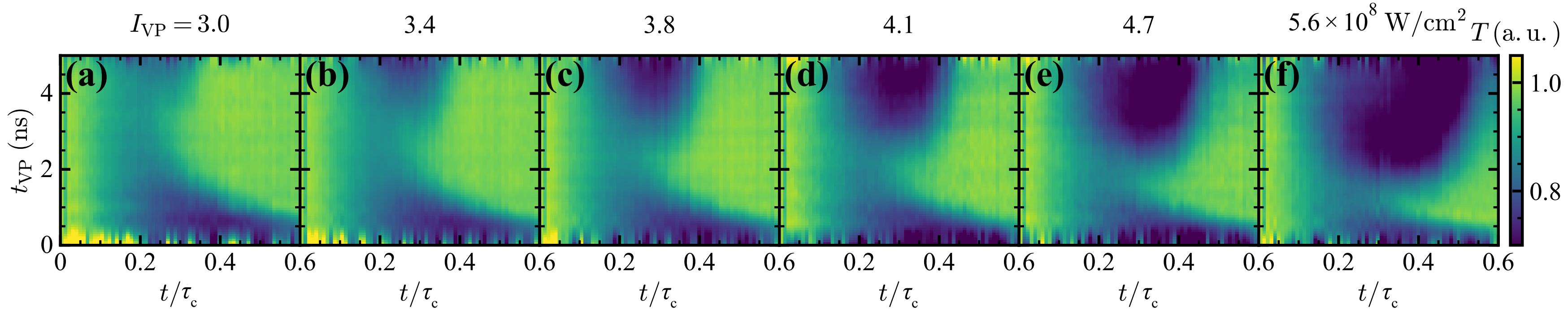

FIGURE 3.8: Photodiode measurements of vaporization pulse transmission shown as heatmaps for multiple intensities (I_{VP}) [cf. Fig. 3.4].

4

Chapter 4

Observation of Discrete Concentric Surface Modulations on Free-Flying Liquid Tin Sheets

H. K. Schubert*, D. J. Engels*, M. Kharbedia, H. Gelderblom, O. O. Versolato

Phys. Fluids **37**, 094108 (2025).

We report on the observation of concentric surface modulations on thin tin sheets formed from laser pulse impact on tin microdroplets (of various diameters $D_0 = 27, 31, 45, 55$, and $70\,\mu$m) at intermediate Weber (We) numbers in the range ∼1 000–7 000. By combining optical inspection in both reflection and transmission modes, we establish that the modulations, with a wavelength on the order of $15\,\mu\mathrm{m}$, have an amplitude of the order of $10\,\mathrm{nm}$ on a sheet (ranging 50 to several $100\,\mu\mathrm{m}$ in radius) with an average thickness of the order of $100\,\mathrm{nm}$. Surprisingly, the modulations appear to be predominantly axisymmetric. The highly reproducible modulations are interpreted as an intermediate We manifestation of the sheet modulations that cause sheet breakup for higher We numbers as investigated by Klein et al. [J. Fluid Mech. 893, A7 (2020)]. We compare the obtained typical wavenumber and amplitude to their model, which relates the instantaneous wavenumber to the key system parameters assuming a Rayleigh-Taylor instability, although questions on the origin of the axisymmetric modulations remain.

4.1 Introduction

Droplet impact on solid surfaces or pillars leads to thin sheet formation [75–81]. Industrial processes that involve droplet deformation upon impact include spray coating (for example, in agriculture [82, 83]), printing [84, 85], and advanced EUV nanolithography systems [65, 86]. Understanding the fluid dynamics of sheet formation is, therefore, critical for optimizing these applications. In state-of-the-art nanolithography machines, thin sheet formation is specifically engineered by laser-driven deformation of liquid tin droplets. An initial laser pulse, known as the prepulse (PP), induces an impulsive acceleration ($a \sim 10^{10}\,\mathrm{m/s^2}$) to the liquid tin droplet, initiating radial expansion of the droplet into a thin sheet target on the capillary time scale ($\sim \mu$s) [65, 86, 87]. This sheet optimizes the subsequent interaction with the main pulse, which produces plasma from the tin sheet and generates the essential extreme-ultraviolet (EUV) light required for high-resolution nanolithography [88–90]. Various hydrodynamic (in)stabilities on such rapidly expanding liquid sheets, play a key role in maximizing EUV yield while minimizing liquid tin "debris" [72].

---

* Shared first authorship: Karl Schubert led the experimental measurements and data analysis, whereas Dion Engels developed the 1-D Raytracer model in Python.

Squire conducted a foundational study on water sheet instabilities leading to atomization [91]. Taylor later confirmed the findings of Squire, demonstrating that sheet instabilities occur only when the liquid system exceeds a critical threshold [92]. Following Taylor's work, numerous studies have explored sheet instabilities using various experimental setups to better characterize and understand the underlying mechanisms. For example, Villermaux and Clanet studied sheet instabilities generated by the impact of a liquid jet on a disc [93, 94], while Li et al. examined sheet instabilities arising from collisions between liquid jets [95]. Bremond and Villermaux [96] took a different approach, investigating the breakup of a thin homogeneous soap film under impulsive acceleration from a uniform shock wave, thereby inducing a Rayleigh-Taylor instability that ultimately leads to sheet fragmentation. That study revealed a time-dependent growth rate and mode selection of wavelengths λ within the range $R_0 \geq \lambda \geq \lambda_c$, where $\lambda_c = 2\pi\sqrt{\sigma/\rho a}$ represents the capillary length of the liquid system of size R_0 (the initial radius of the droplet) with density ρ and surface tension σ undergoing an acceleration a. In these studies, it has been observed that the fastest growing modes dominate the sheet surface modulation, and that the modulation amplitude is a characteristic feature of each liquid system [97, 98]. Vledouts et al. [99] found that impulsive radial expansion of a dense liquid shell triggers a Rayleigh-Taylor instability, leading to destabilization of the shell and the formation of characteristic instability patterns. More recently, Klein et al. [26] investigated the fragmentation of both liquid tin and water droplets impacted by a laser pulse. They proposed that thermal noise inherently present in the laser-matter interaction seeds equally all allowed wavenumbers, assuming white noise, while the acceleration of the droplet after impact drives the selection and growth of specific modes. The fastest-growing modes eventually lead to sheet piercing when their amplitude approaches the sheet thickness. Based on these observations, scaling laws have been developed for characteristic breakup time and wavenumber, identifying specific regions of the sheet, specifically the center and edge, where modulations predominantly can be observed to influence stability [26]. These modulations have primarily been *inferred* from their impact on sheet breakup, particularly hole formation [26]. However, the behavior of instabilities on expanding sheets in the pre-breakup phase remains largely unexplored.

In this work, we experimentally investigate sheet modulations arising from laser-induced deformation of tin microdroplets in a vacuum environment, in a setting similar to that of Klein et al. [26]. We employ our stroboscopic microscopy setup to capture sheet surface *reflections* along with the usual shadowgraphy images, and unveil patterns characterized by discrete concentric rings on intact sheets. These patterns appear consistently and identically on both sides of the sheet. We find that by increasing the laser pulse energy, the concentric symmetry is broken and azimuthal modulations appear to culminate in sheet breakup. The primary aim of the current study, however, is to report on the direct observation of discrete concentric modulation patterns at intermediate We numbers.

Our observations are interpreted along the lines of a model introduced by Klein et al. [26].

4.2 Experimental methods

Our experimental setup has previously been described in detail [24, 67]. Here, we present a summary and the additions that enable the reflection measurements. A more comprehensive schematic of our measurement setup is provided in Fig. 4.11 in Appendix B. The experiment (see Fig. 4.1) employs a droplet generator to produce a kHz stream of liquid tin droplets at a temperature of 270 °C in a vacuum environment at a base pressure of 10^{-7} mbar. Droplet diameters, adjustable between 17 µm and 70 µm, travel at velocities of $\sim$10 m s^{-1} through a continuous-wave HeNe laser light sheet. The scattered HeNe laser light is detected through a photomultiplier tube and down sampled to 10 Hz, triggering the experiment and synchronizing all lasers at the same repetition rate.

Figure 4.1(a–d) illustrates the laser pulse scheme. Figure 4.1(a) shows the prepulse (PP), focused to a Gaussian spot with a full width at half maximum (FWHM) of approximately 100 µm at the droplet location, centered in the vacuum chamber. The PP is generated by a seeded Nd:YAG system (Continuum Surelight III, $\lambda = 1064$ nm) that emits temporally Gaussian pulses with durations ranging from $\tau = 6$ to 20 ns; the pulse length is set to 10 ns unless specified otherwise. Circularly polarized for uniform energy deposition, the PP creates plasma on the side of the droplets where it strikes, imparting an impulsive acceleration (of the order of $\sim 10^{10}$ m/s^2) that drives radial expansion into a thin sheet [87] at velocities of several 100 m s^{-1} on the time scale of the laser pulse duration. Over time, the radial expansion velocity, initially $\dot{R}_0$, decreases due to surface tension on the capillary time scale (on the order of µs), while the propulsion velocity, U, remains constant.

Figure 4.1(b) illustrates the vaporization pulse (VP), focused to a Gaussian spot of 1400 µm × 1280 µm at the center of the chamber. The VP, generated by a seeded Nd:YAG system (Continuum Agilite 569-12, $\lambda = 1064$ nm), emits temporally box-shaped pulses of fixed 50 ns duration. The VP is circularly polarized and vaporizes the liquid tin sheet. The vaporization rate depends on the VP intensity and typically in the experiments is of the order of a few nm ns^{-1} [67]. Under these conditions the vaporization does not lead to any appreciable acceleration.

To observe the liquid tin sheet, we use an imaging system synchronized with the PP timing [Fig. 4.1(c)] or VP timing [Fig. 4.1(d)]. In the case of Fig. 4.1(c), the shadowgraphy pulse (SP) is scanned (in delay steps) at a time Δt after the PP ($\Delta t = 0$ marks the center of the PP). In part of our studies we use a double-framing camera in tandem with two backlighting pulses (spaced as close as 300 ns) to enable studying dynamics on the same sheet, cf. Ref. [25]. In the case of Fig. 4.1(d), the SP is scanned (in delay steps) over the ongoing VP ($t_{\mathrm{VP}} = 0$ marks the start of the VP). The VP itself impacts at a time Δt after the PP. In both cases, we use an imaging system that comprises a dye-based illumination source with 5 ns duration (FWHM), 12 nm spectral bandwidth (FWHM), 560 nm center wavelength and CCD cameras (AVT Prosilica GT2450, pixel size: 3.45 µm and PCO ultraviolet, pixel size: 4.65 µm), coupled to long-distance microscopes (K2 Distamax with CF-1/B objective). This setup provides a spatial resolution of approximately 5 µm, a numerical aperture (NA) of 0.046, and a depth of focus of around 230 µm [100]. At each delay step, we record 20 frames in a stroboscopic manner, with each frame capturing a distinct laser-droplet interaction event. After some finite expansion time, we carefully adjusted the focus at each step for both the front and back cameras throughout the droplet deformation process.

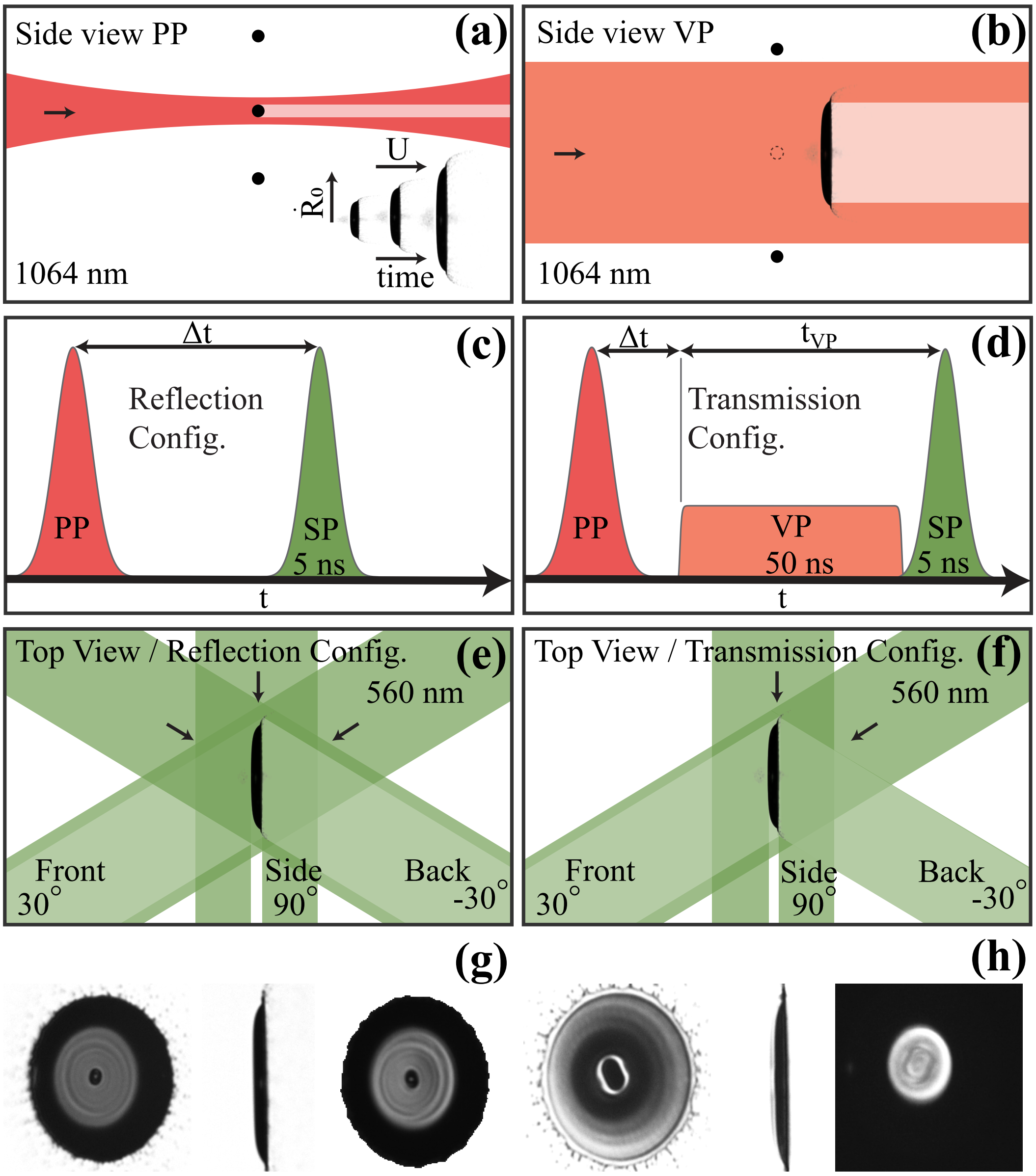

FIGURE 4.1: (a-d) Schematic of the experiment's laser pulse schemes with irradiation geometries and timings shown. (a) Side-view schematic of the prepulse (PP) induced deformation dynamics. (b) Side-view schematic of the vaporization pulse (VP) irradiating the liquid tin sheet. (c) Timing of the shadowgraphy pulse (SP) relative to the PP in the reflection configuration. (d) Timing of the SP in the transmission configuration. The VP follows the PP after Δt, with the SP scanned in time over the VP. (e) Top-view schematic of the reflection configuration showing illumination geometries. (f) Top-view schematic of the transmission configuration showing illumination geometries. Shadowgraphs from front, side, and back view (31 µm, We $\sim$ 3 100, We$_d$ $\sim$ 4 200) (g) in the reflection configuration at $t = 0.21\tau_c$ and (h) in the transmission configuration slightly later at $t = 0.38\tau_c$.

Figure 4.1(e) illustrates the reflection setup. It utilizes three synchronous SPs for front, side, and back view imaging at angles of 30°, 90°, and 150° relative to the laser axis, respectively, and enables observing reflection patterns from both sides of the sheet along the droplet deformation process. Figure 4.1(f) presents the transmission setup, which utilizes two synchronous SPs for front and side imaging at angles of 30° and 90°, respectively, relative to the laser axis. This setup enables the observation of liquid tin sheet dynamics during VP irradiation and has been previously employed to study the vaporization mechanism in detail [67]. Those previous studies [67] have shown that irradiating liquid tin sheets with VP at intensities below $5 \times 10^7\,\mathrm{W/cm^2}$ induces Hertz-Knudsen evaporation, gradually reducing the sheet thickness at a constant, intensity-dependent rate. As a result, the SP transmission through the sheet increases with each successive delay step. We extract the raw optical transmission values pixel by pixel, applying corrections for backlight intensity fluctuations, additional glare sources, and the 30° observation angle. Using the TMM [44] Python package, we establish a relationship between these corrected transmission values and the sheet thickness. In summary, this process integrates an established method to correlate SP transmission values through the liquid tin sheet with its corresponding thickness [25, 67].

4.3 Results

Figure 4.1(g) presents example shadowgraphs obtained with the reflection setup, showing front, side, and back views (left to right). The front view captures the sheet illuminated from the back side, with reflections from the front illumination visible on the inner part of the sheet. Next, the side view reveals a non-trivial curvature of the sheet: the sheet is not flat but at its edges curves away from the laser. Finally, the back view shows the sheet illuminated from the front, with reflections from the back illumination visible on the inner part of the sheet. Note that we employed image-processing techniques to enhance the visibility of the inner reflecting area in the back view while maintaining a consistent background across all shadowgraphs acquired with the reflection setup for this example. This adjustment accounts for the varying background illumination intensities between the front and back views. The acquisition reveals that only an inner region of the sheet reflects light, as the sheet's non-trivial curvature causes the relatively large surface angles outside this region to reflect incoming rays outside the NA of the imaging system (see below). More importantly, the reflection of the inner part of the sheet is not uniform but displays a discrete concentric pattern. This reflection pattern suggests the presence of a discrete concentric modulated sheet profile that appears to be similar on both sides.

Figure 4.1(h) shows example shadowgraphs obtained with the transmission setup from front, side, and back views (left to right). In this setup, the front view captures the sheet under back illumination during the vaporization pulse. The shadowgraphs clearly show the presence of the main features of the target: center mass, sheet, bounding rim, ligaments, and fragments [25]. We observe gradual mass removal from the sheet with increasing t_{VP} through the increase in transparency of the sheet to shadowgraphy backlight illumination in line with prior works (e.g., see [67]). The front view highlights the presence of discrete concentric regions with greater thickness, indicating a *thickness* modulation of the sheet profile as vaporization occurs at a globally constant, intensity-dependent rate [67]. The side view shows another perspective of the vaporization progress, while the back view captures back illumination reflections from the inner, thicker, yet not-yet-vaporized part of the sheet.

In our experiments, the PP laser energy can be adjusted, directly influencing two key parameters: the propulsion Weber number (We) and the deformation Weber number ($\mathrm{We_d}$) following e.g. Refs. [25, 26]. These two parameters are defined as follows:

$$\mathrm{We} = \frac{\rho U^2 D_0}{\sigma}, \quad \mathrm{We_d} = \frac{\rho \dot{R}_0^2 D_0}{\sigma}. \tag{4.1}$$

Here, $\rho = 7000\,\mathrm{kg/m^3}$ and $\sigma = 0.55\,\mathrm{N\,m^{-1}}$ represent the density and surface tension of the liquid tin, respectively, while D_0 is the initial droplet diameter [31, 101]. We extract the propulsion velocity (U) and initial expansion velocity ($\dot{R}_0$) from shadowgraph images [cf. Fig. 4.1(g)], with U measured from side-view shadowgraph images (1–4 µs) and $\dot{R}_0$ from front-view shadowgraph images (200–500 ns). As we will explain below (see Sec. 4.4), the propulsion Weber number (We) seeds and mode-selects a Rayleigh-Taylor-type instability [26], while the deformation Weber number ($\mathrm{We_d}$) drives sheet expansion [101] and with it the stretching of the surface modulations (along with the other dynamics relevant for target preparation [72]). The ratio of the two Weber numbers $\mathrm{We_d}/\mathrm{We}$ is of order unity and typically reduces with laser pulse energy and length [102]. The droplet deforms into a sheet-type target on an inertial time scale $\tau_\mathrm{i} = D_0/U$ and the overall sheet expansion process occurs on a capillary time scale $\tau_\mathrm{c} = \sqrt{\rho D_0^3/6\sigma}$. We note that the definitions of We, $\mathrm{We_d}$, and τ_c used here differ from those in Klein et al. [26] to adhere to a more consistent notation by using D_0 in all combined equations.

In the following, we first discuss in detail the observations obtained using the reflection setup (Sec. 4.3.1), followed by those obtained using the transmission setup (Sec. 4.3.2). For an overview of the parameters used, refer to Tab. 4.1 in the Appendix.

4.3.1 Reflection

By varying the laser pulse energy, and with it the Weber number, we observe changes in the reflection patterns. Figure 4.2(a-d) presents shadowgraphy images of expanding sheets at time $t = 0.2\tau_\mathrm{c}$ of a 31 µm droplet for increasing We. At (for the current work) relatively low We numbers we observe discrete concentric reflection patterns. At higher We, the concentric reflection pattern develops azimuthal components, i.e., angular modulations around the sheet's center that perturb the predominantly concentric rings. We observe that azimuthal modulations begin at the outer radii earlier than at the inner radii, indicating perhaps an additional dependence on sheet thickness and time, driven by continuous thinning during droplet deformation [25] or sheet radius. We find that the azimuthal modulation wavelength is of similar order as the wavelength of the concentric modulation. At even higher We the pattern randomizes with no clear symmetry. This observation indicates a transition from discrete concentric to azimuthal modulations with randomized phases, similar in appearance to the work of Xia et al. [103].

For the highest We numbers, hole formation becomes evident in line with Refs. [25, 26], with the amplitude of the perturbations reaching a magnitude similar to the local thickness of the liquid sheet [26]. To better understand both the reflection pattern and hole formation, we present shadowgraph images in Fig. 4.2(e, f) showing two example sheet breakup events of a 50 µm-diameter droplet at $t = 0.3\,\tau_\mathrm{c}$ with a very high We of approximately 123 000, using a double-framing camera in tandem with

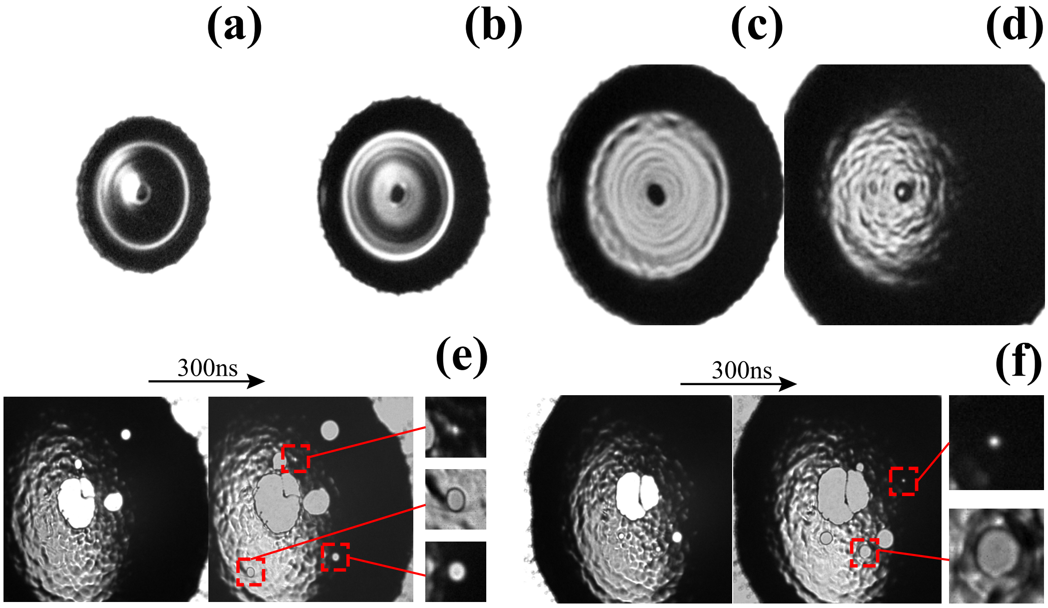

FIGURE 4.2: Front view reflection shadowgraphs of 31 µm-diameter droplets subjected to a 10 ns laser pulse at a common non-dimensionalized time $t = 0.2\tau_c$ for: (a) We = 800, $\mathrm{We_d} = 1\,200$; (b) We = 1 700, $\mathrm{We_d} = 2\,300$; (c) We = 4 700, $\mathrm{We_d} = 5\,800$; and (d) We = 12 000, $\mathrm{We_d} = 10\,600$. The lower row (e, f) shows (at $t = 0.3\,\tau_c$) 50 µm-diameter droplets exposed to a 15 ns laser pulse, achieving approximately We = 123 000, $\mathrm{We_d} = 57\,000$. For both cases, the left image depicts the initial state, while the right image shows the *same* sheet 300 ns later using a double-framing camera (see the main text).

two backlighting pulses, to enable capturing the dynamics of specific single holes. Each panel shows the initial sheet state (left) and the same sheet just 300 ns later (right). The initial shadowgraphs reveal preexisting holes in the liquid tin sheet, while the subsequent frame captures newly formed holes (marked with red circles) and their growth following Taylor-Culick [25, 26]. These shadowgraphs demonstrate that our setup enables direct observation of sheet modulations in reflection prior to sheet breakup.

As holes open, they induce additional radial modulations (lower inset in Fig. 4.2(f)) and lead to ligament formation, as reported by Vledouts et al. [99]. Importantly, the connecting ligament between the center mass and the sheet provides clear evidence that the center mass remains physically connected to the sheet prior to hole formation. While hole formation highlights later stages of sheet evolution, the earlier stages of surface modulations also offer valuable insights. At intermediate We values around 2 300, as shown in Fig. 4.2(b), the sheet exhibits a striking discrete concentric reflection pattern. This pattern facilitates clearer analysis, including comparisons between front- and back-view acquisitions, allowing a more detailed understanding of the instability's growth rate and propagation.

In summary, Fig. 4.2 shows that the laser-on-droplet impact causes various types of reflection patterns depending on the Weber number. We hypothesize that these reflection patterns share a common underlying primary instability mechanism, similar to the Rayleigh-Taylor type proposed by Klein et al. [26] (see discussion in Sec. 4.4 below). At lower We, we observe discrete concentric reflection patterns that are more easily traceable; these will be the main focus of the current study.

We next qualitatively examine the temporal evolution of the reflection pattern for a low We. Figure 4.3 illustrates the sheet expansion of a 31 μm droplet with a low We of $\sim 1\,700$ shown from the (a) front, (b) side, (c) back and (d) combined front/back views. For each delay step we average 20 frames to improve the signal-to-noise ratio. During the characteristic sheet expansion following impact (see Ref. [79]), an inner region on both sides of the sheet reflects the green shadowgraphy light. The radial extent of this reflective region roughly follows the overall trajectory of the expanding sheet. This contraction arises from the temporal evolution of the global sheet curvature. As the curvature evolves, the sheet's surface angles increasingly reflect light outside the NA of the imaging system, causing those regions to be dark. Consequently, the reflective region is limited to those areas where the sheet's surface angles allow reflections within the NA, as we will explore in more detail in Sec. 4.3.1.

Figure 4.3(d) highlights that during the sheet expansion, the inner reflective region exhibits discrete concentric reflection patterns that are highly similar (within a fraction of the wavelength) in both the front (left) and back (right) views, suggesting a coupling between the concentric modulated surfaces of the sheet. Noticeable differences between the front and back views are primarily observed near the center mass.

We identify an onset time of discrete concentric reflections on both sides around $t = 0.19\,\tau_c$. At this time, the thickness of the inner reflective region is estimated to be larger than ~500 nm, based on a thickness model for liquid tin sheets provided by Liu et al. [25]. This suggests that the surface modulations are coupled already in the early stages of the droplet deformation. At earlier times, such as at $t = 0.13\,\tau_c$, the back curvature differs from the front curvature, as no concentric reflection patterns are observed in the back view in line with a Rayleigh-Taylor scenario (see below) in which the laser-facing surface destabilizes first. Although discrete concentric reflections may still form earlier during the expansion, we do not detect them perhaps due to limitations in resolution and in the focusing of the imaging systems throughout the expansion.

As the sheet expands, the surface modulations responsible for the reflections stretch over time, with a closer spacing observed at earlier times (e.g., compare $t/\tau_c = 0.26$ with $t/\tau_c = 0.44$).

Also, the data hint at a wavelength that is a function of the radial coordinate, with larger spacings between bright rings towards the large radii (cf. Fig. 4.3(a) near $t/\tau_c = 0.26$). Around the sheet expansion apex ($t/\tau_c = 0.38$), we may extract a typical modulation wavelength of approximately 15 μm as the difference between two bright rings.

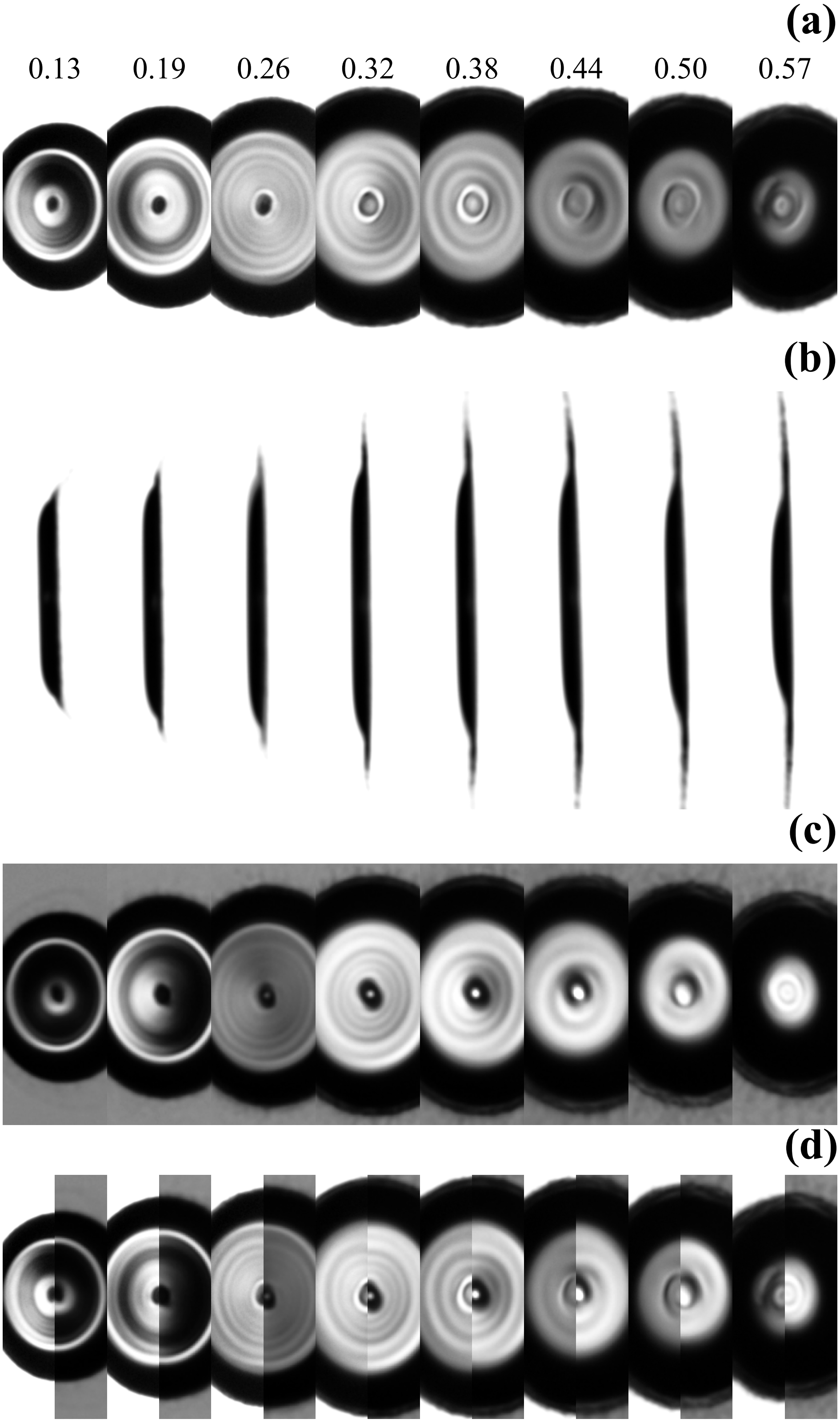

FIGURE 4.3: Shadowgraphy images of sheet expansion of a 31 µm diameter droplet, propelled to $\mathrm{We} = 1\,700$, and $\mathrm{We_d} = 2\,300$ in (a) front view, (b) side view, (c) back view, and (d) combined front view (left) and back view (right) comparison. Numbers on the top indicate the non-dimensional time t/τ_c.

In the following, we address several open questions. What sheet morphology causes the observed discrete concentric reflections? What are typical amplitudes of these surface modulations? Finally, can we argue that these surface modulations are symmetrically phased?

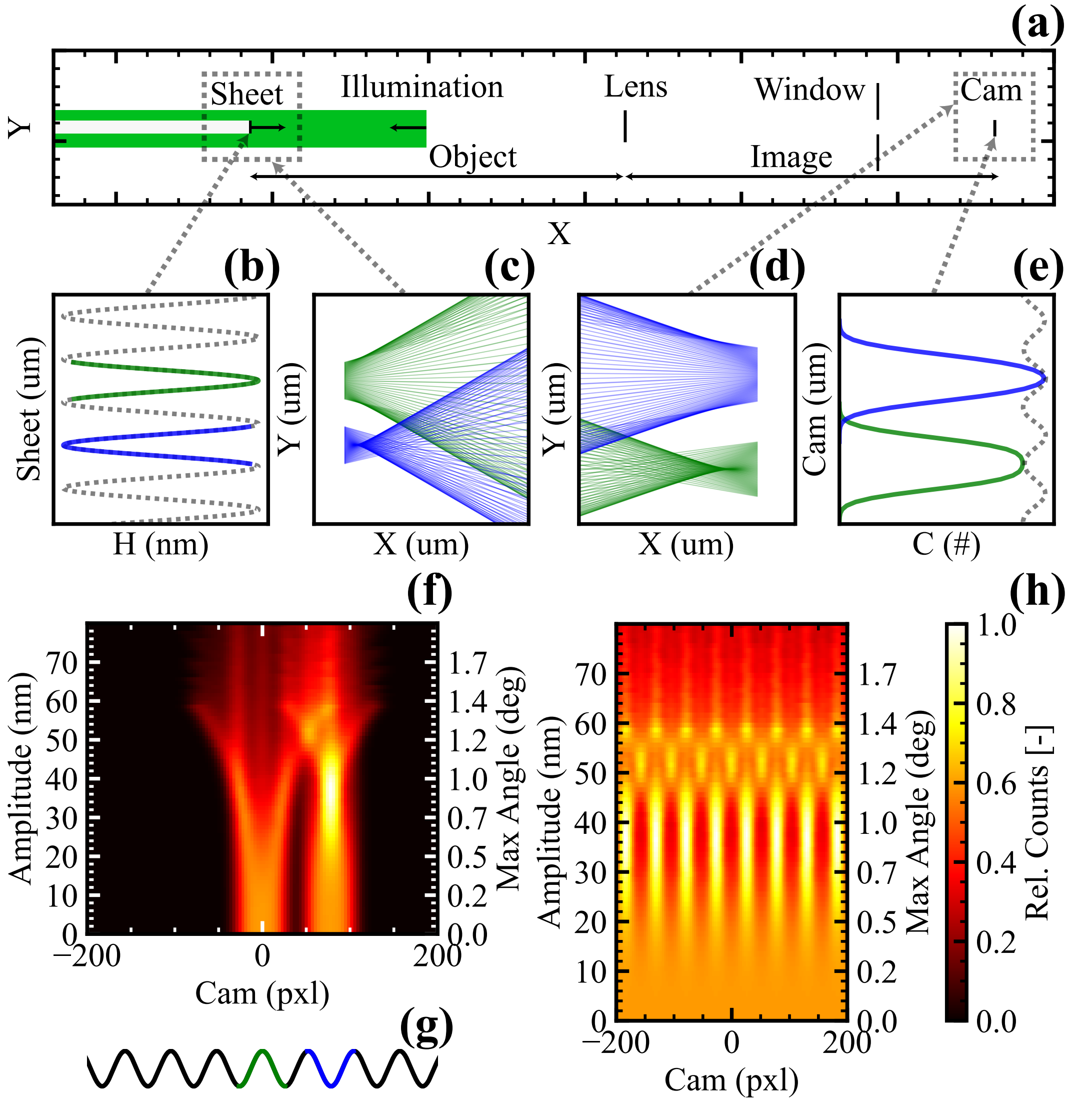

FIGURE 4.4: (a) Overview of the ray tracer model, showing key components: illumination source, sheet, window (1.5″), lens (2″), and camera chip. (b) Close-up of a model sheet with a sinusoidal modulation of 15 µm wavelength and 15 nm amplitude, highlighting a single hill (green) and a sink (blue). (c) Reflected rays near sheet hill and sink. (d) Ray convergence on the camera chip. (e) Ray count on the camera chip corresponding to sheet hill and sink, with total ray count (grey). (f) Ray distribution on the camera chip as a function of amplitude for isolated sheet features highlighted in (g). (h) Ray distribution for the full sinusoidal surface.

To interpret the reflection measurements, we utilize an in-house developed 1-D raytracer to correlate the reflection intensity recorded on the camera chip with height modulations on the sheet surface. Fig. 4.4(a) depicts the modeled setup in side view with the illumination and camera positioned in the same plane for simplicity (i.e., back illumination and back camera). It illustrates the raytracer model setup and its key components, while Figs. 4.4(b, c, d) provide zoomed-in views of an example simulation. In the simulation, a spatially box shaped illumination pulse is used and the lens is modeled as ideal, with a constant focal length across its surface. Rays are initialized from the light source and directed toward the sheet, which is assigned a sinusoidal modulation with adjustable parameters such as amplitude (η) and wavelength (λ) at any radial location on the sheet (r) in $y = \eta \cos(2\pi/\lambda r)$. A sinusoidal modulation with a wavelength of 15 µm is chosen, in line with the typical wavelength that may be observed in the experiment cf. Fig. 4.3. Figure 4.4(b) depicts an example sinusoidal modulation, highlighting a hill (green) and sink (blue) regions. Upon reaching the sheet, rays are reflected specularly. As shown in Fig. 4.4(c), hill regions cause ray divergence, while sink regions lead to focusing. Reflected rays then propagate further and encounter the lens, where they are refracted according to Snell's law. Figure 4.4(d) shows the rays after lens refraction, just before reaching the camera chip that is placed in the image plane. Due to the single-lens imaging system, the reflected image is inherently flipped. A zoomed-in view near the camera chip highlights how blue rays (from sinks) accumulate on the chip, creating bright regions, while green rays (from hills) diverge, resulting in dimmer regions. Finally, Fig. 4.4(e) presents the accumulated counts within each camera pixel (3.45 µm), with the gray line indicating the total counts if the full sheet reflects. This example simulation shows that a hill (green) causes lower count on the camera chip than a hill (blue).

We demonstrate that our raytracer simulation effectively maps reflection points on the sheet to their corresponding positions on the camera sensor. The simulation reveals that the bright, discrete concentric reflections observed on the sensor originate from surface sinks.

Building on this insight, we investigate the effect of varying sheet modulation amplitudes. Note that in the following, the sheet and counts are plotted from the perspective of the camera. Figure 4.4(f) presents a heatmap of the camera count distribution as a function of sheet modulation amplitude for selected regions of a sinusoidal modulated sheet profile. These regions are highlighted in Fig. 4.4(g), with a hill marked in green and a sink marked in blue.

At very low amplitudes, both hill and sink produce similar count patterns, as the amplitude increases, the hill count pattern spreads a bit and loses contrast, while the sink pattern shows an increase in contrast, maximizing between 30–40 nm. At higher amplitudes, some interference occurs between the reflecting regions on the sheet, and beyond 60 nm, the camera counts diminish because of the NA limit. The right axis of the heatmap indicates that the maximum observable surface angle is approximately 1.42° (corresponding to a full surface angle of $\theta = 2.84°$ and NA of 0.049). This aligns with our experimental setup and supports the conclusion regarding why only an inner region reflects, as shown in Fig. 4.3. Beyond this maximum angle, imaging of the SP reflection becomes impossible due to the NA limitations of the experimental setup. The local sheet surface normal can exceed this angle, for instance, in cases of large modulation amplitudes or high curvature, and would then produce a dark region.

Figure 4.4(h) presents a heatmap of camera counts for a fully reflecting sinusoidally modulated sheet profile, illustrating both the maximum observable surface angle and the interference patterns that again arise at higher amplitudes. We note that both heatmaps [Fig. 4.4(f,h)] are globally normalized, making it difficult to identify differences between hills and sinks at low amplitudes. At around 10 nm amplitude, these contrast differences (ratio of count values between maxima and minima) are approximately 4 %; at 30 nm amplitude the contrast already increases to approximately 50 %.

Next, combining raytracer insights (Sec. 4.3.1, Fig. 4.4) with experimental shadowgraphs (Sec. 4.3.1, Fig. 4.3), we arrive at the following conclusions. We learn that dark regions in shadowgraphs correspond to reflections from surface modulations (hills). The phase-relation question is resolved: a hill decreases the camera count, while a sink increases it. From the reflection measurements, it is observed that the surface reflections are approximately in a fixed phase, meaning a bright spot in the front view corresponds to a bright spot in the back view. This suggests a symmetric relation between the sheet surfaces, with both surface modulations being out-of-phase (i.e. they are mirror symmetric, see schematic in Fig. 4.5). The contrast that is typically observed for good ripple observation cases in the experiments [such as those shown in Fig. 4.3(a)] lies at the level of 5–10%, which, following the simulations, would be consistent with a modulation amplitude of approximately 10–15 nm in this specific example. Assuming a symmetric sheet instability, the thickness variation indicates that the thickest regions are given by $h_\mathrm{m} = h_0 + 4\eta_0$. Of course, any nonzero phase (Φ) would reduce the thickness, as is illustrated in Fig. 4.5.

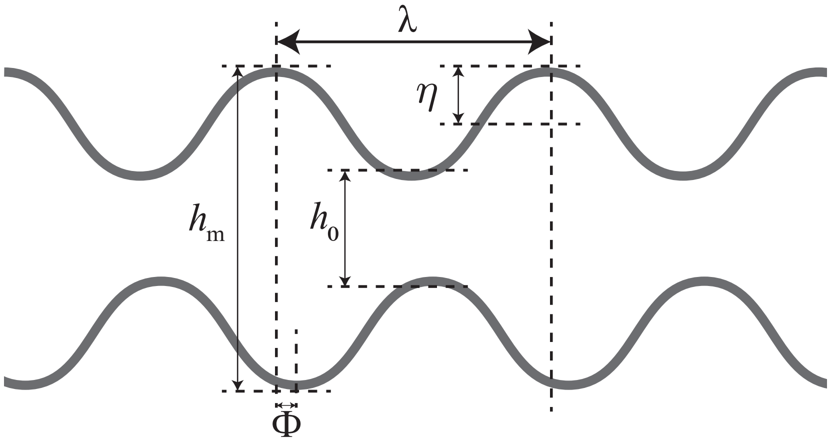

FIGURE 4.5: Schematic of a symmetric sheet instability with modulation amplitude η, modulation wavelength λ undisturbed sheet thickness h_0, disturbed thickness h_m, and phase Φ.

4.3.2 Vaporization

We apply a vaporization pulse [see methodology in Fig. 4.1(b, d, f, h)] to a liquid tin sheet to better understand its modulation by studying variations in thickness as enabled by the vaporization method, following Ref. [67]. Specifically, we aim to validate the relative amplitude of the modulation (η) under the assumption of a symmetric sheet instability (see Fig. 4.5). First, we link the reflection and transmission data and then estimate the thickness of the observed modulations.

In Fig. 4.6, we generate an intermediate We = 3 100 with concentric modulations and compare shadowgraphs recorded using the reflection and transmission setups. This slightly higher We compared to Fig. 4.3 is chosen to improve comparability between

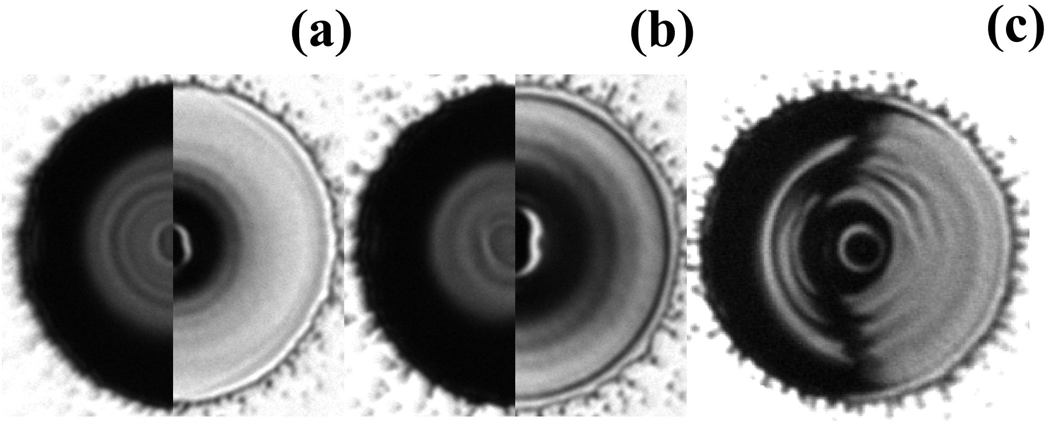

FIGURE 4.6: Front view reflection shadowgraph (left) alongside a front view transmission shadowgraph (right) of the same We but a different frame [31 µm droplet diameter, We $\sim$ 3 100, We_d $\sim$ 4 200] at (a) $t/\tau_\mathrm{c} = 0.24$ and (b) $t/\tau_\mathrm{c} = 0.38$. (c) A liquid tin sheet irradiated only locally by a modified VP, leading to predominant vaporization on the right side while reflecting SP light on the left side [36 µm diameter droplet, $t/\tau_\mathrm{c} = 0.31$, We $\sim$ 1 400, We_d $\sim$ 3 900]. In both panels, the shadowgraphs have been adjusted (they are horizontally stretched) to account for the observational angle of 30°.

the reflection and transmission setup. We trade off visibility of the reflections (best seen at low We) for transmission (best at high We numbers where sheets are thin).

Figure 4.6 shows shadowgraphs from the reflection setup (left) and the transmission setup (right) at (a) $t/t_c = 0.24$ and (b) $t/t_c = 0.38$. The reflection shadowgraph has been discussed in detail in Sec. 4.3.1. The transmission shadowgraph is obtained by applying a VP, which induces gradual thinning of the sheets thickness profile [67] [also see the schematic in Fig. 4.1(f)]. For this We value, the thinning process results in the formation of dark concentric rings. These rings correspond to regions of greater sheet thickness, as the evaporation is governed by a globally constant, intensity-dependent rate that is independent of the instantaneous thickness [67].

More specifically, in Fig. 4.6(a), right-hand side, we select a transmission shadowgraph captured along a VP irradiation delay scan, where free-flying thickness modulations are clearly visible. Both reflection and transmission measurements exhibit patterns with closely matching periodicity, confirming the presence of surface modulations and that their mutual phasing leads to thickness variations in the liquid tin sheet's profile.

The transmission shadowgraph also highlights that, due to the sheets thickness gradient [25], the outer parts of the sheet evaporate earlier than the inner parts. As a result, thickness modulations in the sheet thickness profile at the outer radii become visible and fully vaporize earlier than those closer to the center.

With continued VP irradiation, the inner parts of the sheet begin to exhibit finite transmission, leading to the unraveling of the inner sheet thickness modulations, while fully vaporizing the outer ones. This dynamic not only confirms the presence of thickness modulations but also provides a basis for quantifying their thickness (see below).

To compare reflection and transmission over a larger sheet area, we acquire shadowgraphs later in the droplet deformation process at $t/\tau_c = 0.38$, as shown in Fig. 4.6(b) for the same We. At this stage, the reflection pattern shows noticeable changes, with the inner reflective area being slightly reduced in size compared to earlier times. This observation is consistent with that for the slightly lower We case shown in Fig. 4.3. The time $t/\tau_c = 0.38$ corresponds to the sheet expansion apex, where the thickness gradient is much weaker, resulting in a more homogeneous thickness profile [25] which benefits visibility of any thickness modulations over a large area. This example demonstrates that a low thickness gradient does not necessarily correlate with the curvature of the sheet. At this time, the thinner sheet exhibits a smaller area reflecting into the NA of the imaging system (cf. Sec. 4.3.1).

In contrast, the transmission measurements reveal thickness modulations in the sheet that are not observable in reflection. This confirms that these thickness modulations persist throughout the droplet deformation process and emphasizes that each methodology has a distinct observational window: For the reflection setup, optimal conditions require a locally flat sheet, whereas for transmission, a more homogeneous sheet thickness profile is preferred instead. In this sense, the reflection and transmission methods give a complementary view of the surface modulations.

Finally, we compare reflection and transmission shadowgraphs by optimizing the conditions for both setups for the same sheet. This is achieved by selecting We $= 1\,400$ and $t/\tau_c = 0.31$, as shown in Fig. 4.6(c). We vaporize only the right side of the sheet using a VP intensity that induces evaporation up to the sheet center. Even in this case, despite the high similarity and consistent wavelength of patterns observed in reflection and transmission, we cannot draw definitive conclusions about the exact relationship between the bright (or dark) concentric reflections in the reflection shadowgraph and the dark concentric rings in transmission, because of poor contrast in the transition area.

In the following, we use the VP to estimate the sheet thickness and, from the thickness, derive the amplitude of the modulation assuming a symmetric sheet instability (see Fig. 4.5).

Figure 4.7 shows liquid tin sheets in the leftmost column at two different times during the droplet deformation process: (a) at $t/\tau_c = 0.28$ and (b) at $t/\tau_c = 0.37$. At both expansion times, a VP delay scan is performed. The left column shows a frame of the VP delay scan that highlights the progress of vaporization and the presence of thickness modulations. For both VP delay scans, the VP intensity is carefully adjusted to achieve sufficient vaporization of the sheet at the end of VP irradiation, resulting in evaporation rates [67] of 6.4 nm/ns and 2.6 nm/ns, respectively, as explained in more detail below.

The middle column of Fig. 4.7 shows direct thickness maps (h_T), obtained from the transmission shadowgraphs in the leftmost column using the transmissivity method (for further details, see Sec. 4.2). In both cases, concentric thickness modulations are evident, but are challenging to resolve directly in thickness.

The right column shows the reconstructed sheet thickness profile (h_{VP}). The sheet profiles are obtained as follows: First, we align all shadowgraphy frames for each delay step (t_{SP}) during VP irradiation. Next, we determine pixel-wise vaporization times by evaluating whether a pixel has been vaporized in more than 50 % of the

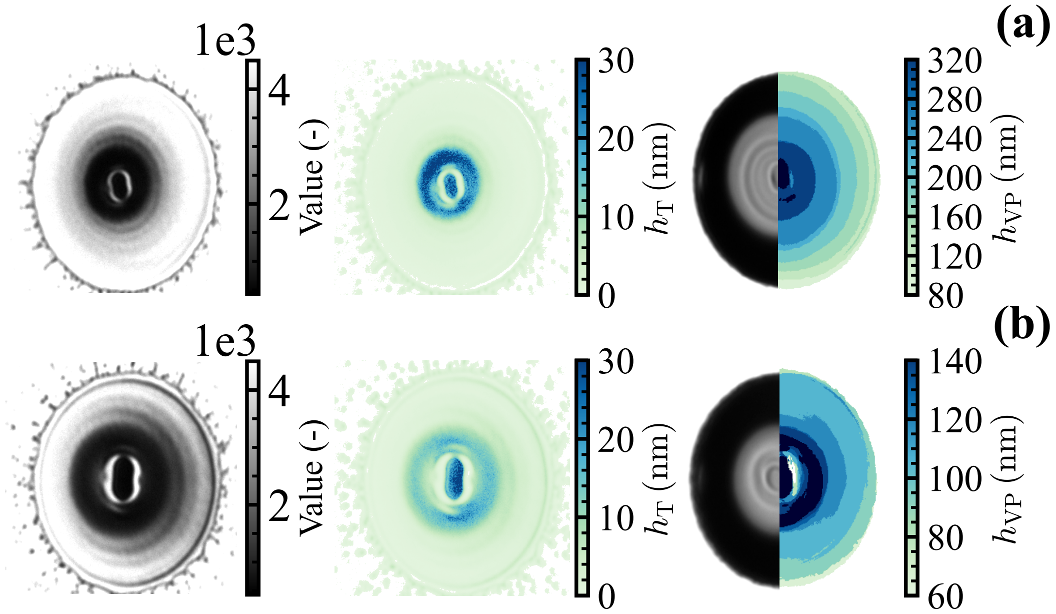

FIGURE 4.7: Shadowgraph images and analysis. From left to right: partially vaporized sheet, corresponding thickness map using transmissivity method (see Ref. [67]) and reconstructed sheet thickness map by using the vaporization time and vaporization rate. Both rows show data for a 31 µm diameter droplet propelled to We $\sim$ 3 100 and $\mathrm{We}_d \sim$ 4 200 at time (a) $t/\tau_c = 0.24$ and (b) $t/\tau_c = 0.37$.

frames for a given delay. We then calculate the sheet thickness maps by multiplying the pixel-wise determined delay values t_{SP} with the vaporization rate $\dot{h}$, such that $h_{VP} = t_{SP} \times \dot{h}$. We define a pixel as vaporized if its value reaches 30 % of the green SP backlight illumination through the sheet at a refractive index of $n = 1.7 + 5.1j$ (corresponding to 1100 K, see Ref. [104]), indicating a residual sheet thickness of 6 nm as calculated using the TMM [44] Python package. The thickness threshold is set to 6 nm because the sheets were not fully vaporized at the end of the VP irradiation. Thus, regions with thicknesses exceeding 6 nm at the end of the VP irradiation are represented as dark blue areas in the reconstructed thickness maps, indicating unknown thickness. Note that we thereby underestimate the thickness in these areas; however, this is of no substantial consequence as we focus on differences in thickness, as explained below. We determine the value of $\dot{h}$ by fitting the sheet thickness values to the profile calculated with the thickness model for liquid tin sheets as introduced by Liu et al. [25]. Additionally, we correct the obtained thickness for the observational angle of 30°.

The rightmost heatmap may suggest a stepwise reduction of the sheet radius. However as shown in [67], evaporation occurs gradually. The apparent stepwise reduction is instead caused by the shadowgraphy scan step size of Δ5 ns, which results in a delay step-wise thickness reduction given by $h = \Delta t_{SP} \times \dot{h}$. In case (a), the stepwise reduction is approximately 30 nm, while in case (b), it is approximately 13 nm. Since we compare the reconstructed thickness map with the transmission shadowgraph, we can infer that a height modulation is on the order of a vaporization step, providing an upper limit for the thickness modulation. As the sheet shown in row (a) is measured earlier in the expansion curve than (b), the sheet is thicker [72], and the VP intensity required to sufficiently vaporize it by the end of the VP duration is higher, resulting in (intentional) differences in the vaporization rate. The observation that the thickness modulation is of the order of one vaporization step then tentatively hints that the sheet in row (a) has thicker modulations than the one in row (b). This, in turn, may suggest that the thickness modulations decrease over time, which we hypothesize occurs due to a radial and temporal-dependent stretching (see Sec. 4.3.1). Furthermore, a radially dependent stretching would imply that the thickness modulations at radii farther from the center are thinner than those closer to the center. As we previously outlined, the reflection and transmission setups provide complementary measurements (see Fig. 4.6). Here, a full vaporization of thickness modulation primarily occurs at larger radii where reflections are not observed, potentially probing thinner thickness modulations. Thus, this approach offers an upper estimate for the thickness modulation within the vaporized radii.

We now interpret the observed thicknesses in the context of the predicted symmetric sheet instability, inferred from the reflection patterns that are highly similar in back and front view, combined with raytracer insights, which suggest that only identical sheet features can produce the observed reflection patterns. In the case of a perfectly symmetric mode, the thickest part of the sheet would be $h_\mathrm{m} = h_0 + 4\eta$ (see Fig. 4.5). For the estimated modulation thicknesses, the corresponding derived amplitudes are approximately in the range of $3-8$ nm. In a direct comparison between simulation and reflection pattern at $t/\tau_\mathrm{c} = 0.28$, we achieve contrast ratios similar to the experimental using a raytracer amplitude of about 12 nm cf. Fig. 4.4(h). These complementary estimates of the amplitudes are reasonably consistent given (i) the uncertainty in the VP method (and limited step size); (ii) the fact that the reflection amplitude may only be obtained from the inner part of the sheet and the thickness from the outer part. It may well be that, indeed, modulation amplitudes reduce with the radial coordinate. Additionally, it is possible that the two surfaces of the sheet are not perfectly symmetrically coupled in this specific measurement: any phase shift Φ of the surface modulation would result in a reduced overall thickness and, consequently, a smaller inferred amplitude (see the schematic in Fig. 4.5).

We next aim to understand how the location of the peak of the plasma pressure influences the symmetry and distribution of the modulations. By adjusting the timing of the arrival of the PP, we can adjust the laser-to-droplet alignment [105]. Such alignment adjustments lead to a tilt of the sheet, as shown in side view in Fig. 4.8(a). For consistency, the PP energy is tuned for each (intentional) misalignment condition such that the propulsion velocity remains approximately constant. To enable clear observations of thickness modulations after vaporization, we set PP energies (and, thus, We numbers) to values such that some azimuthal modulations occur, but concentric ripple patterns still remain dominant. Measuring the reflection pattern is not feasible in this case, as the tilt creates curvature with a surface normal that reflect light outside the NA of the imaging system. We observe that a negative misalignment (that is, the laser strikes the towards the upper pole of the droplet) leads to a negative tilt angle (cf. the -21.0° example in Fig. 4.8). This negative misalignment leads to a much more rapid expansion of the top part of the sheet, given there is less mass to be accelerated, and makes that the center mass appears in the bottom half of the sheet. We observe that the thickness modulations are not simply concentric around the sheet center but instead are centered around its shifted center mass. Thus, we conclude that the concentric pattern is centered at the location of the peak pressure.

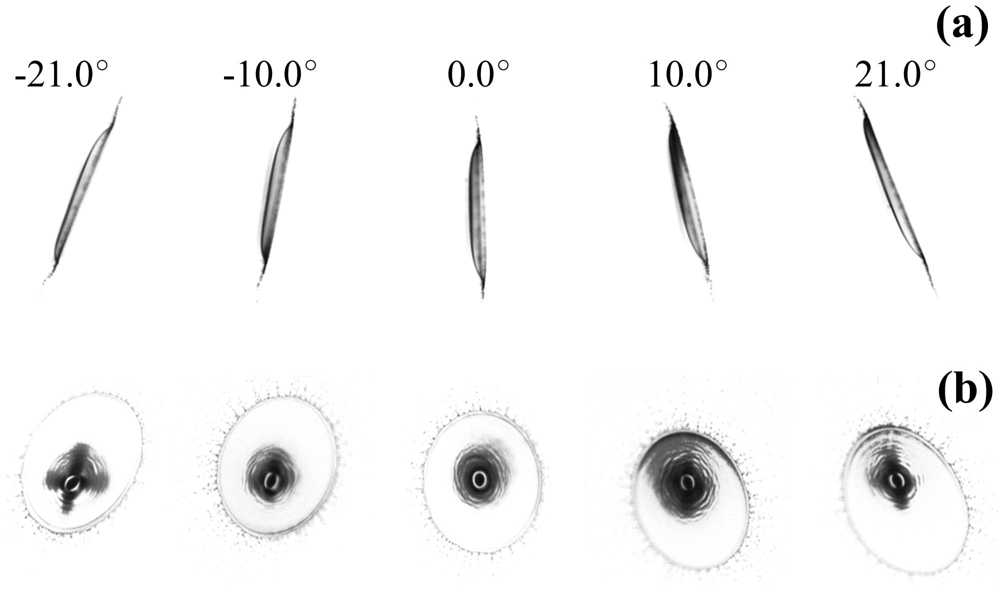

FIGURE 4.8: Side (a) and front view (b) shadowgraphs from partially vaporized targets for different PP misalignment conditions (resulting tilt angles are shown), for a 27 µm diameter droplet hit by a PP propelling to We $\approx$ 7000, observed at a time $t/\tau_c \approx 0.4$.

4.4 Discussion

We next interpret our observations with the instability model proposed by Klein et al. [26], which provides estimates for the characteristic breakup time t_s and wavenumber k_s for highly modulated sheets. They suggest that a Rayleigh-Taylor (R-T) type instability may be triggered on the laser pulse "ejection time scale" τ_e [26], during which the liquid tin droplet experiences an acceleration $\sim U/\tau_e$. This acceleration is caused by pressure exerted by the laser-induced plasma normal to the surface of the still spherical droplet, leading to the amplification of any perturbations present on the interface of the droplet. The amplified perturbations continue to evolve inertially in the absence of an external acceleration (which ends with the laser pulse), and are affected by capillary forces on a dynamically changing topology of the evolving sheet. The model describes the evolution of the instability during the droplet deformation process. Here we interpret our findings along the same lines. In the following, we use the non-dimensional expressions for wavenumber $\hat{k}$ and time $\hat{t}$:

$$\hat{k} = kR_0, \qquad \hat{t} = \frac{t}{\tau_c} \tag{4.2}$$

with R_0 as initial droplet radius. The model defines three-phases (see Fig. 4.9), in brief:

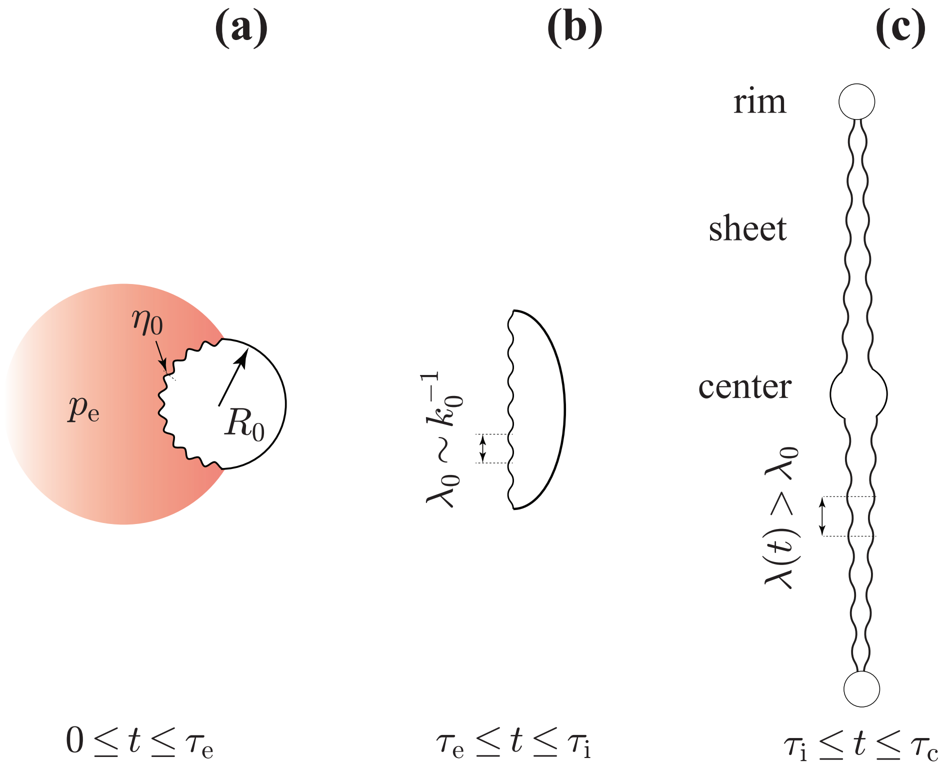

FIGURE 4.9: Schematic based on the Rayleigh-Taylor instability-type model proposed by Klein et al. [26], illustrating three distinct phases: (a) acceleration, (b) expansion, and (c) stretching, each associated with their respective time scales. The symbols used are η_0 (initial amplitude), p_e (plasma pressure), R_0 (initial droplet radius), and τ_e (acceleration time); λ_0 (initial wavelength), k_0 (initial wavenumber), τ_i (inertial time scale); $\lambda(t)$ (wavelength over time); and τ_c (capillary time).

1. **Acceleration Phase** ($0 \leq t \leq \tau_e$):

   During this phase, the droplet undergoes an impulsive acceleration driven by the laser-induced plasma over the (very short) duration of the laser pulse (τ_e). The plasma introduces thermal (white) noise, which seeds permissible wavenumbers $1 \leq \hat{k} \leq \hat{k}_c$ on the liquid, with $\hat{k}_c = \sqrt{\rho a R_0^2/\sigma} = \mathrm{We}^{1/4}\tau_e^{-1/2}$ the capillary wavenumber [26]. The acceleration sets a growth rate for the permissible R-T unstable modes with an initial amplitude η_0 and associated wavenumber k. At the end of phase 1 each mode has a specific growth rate while the corresponding normalized amplitude is still equal to unity given that the modes did not yet have any time to grow, given the impulsive nature of the acceleration.

2. **Expansion Phase** ($\tau_e \leq t \leq \tau_i$):

   Following the acceleration, the droplet transitions into a flattened, sheet-like structure. In the absence of acceleration, the excited modes inherited from phase 1 continue to evolve inertially due to the velocity (growth rate) they acquired during phase 1 (see Ref. [26] for the detailed derivation). The fastest-growing mode at the end of phase 2 is given by:

$$\hat{k}_{\max} = \frac{\mathrm{We}^{1/4}}{\sqrt{3\hat{\tau}_{\mathrm{i}}}}, \tag{4.3}$$

with phase 2 ending at $\hat{\tau}_{\mathrm{i}} = \mathrm{We}_{\mathrm{d}}^{-1/2}$. This enables rewriting Eq. (4.3) to obtain:

$$\hat{k}_{\max} = \sqrt{\mathrm{We}_{\mathrm{d}}} \frac{1}{\sqrt{3}} \left(\frac{E_{\mathrm{k,cm}}}{E_{\mathrm{k,d}}} \right)^{1/4}, \tag{4.4}$$

where we introduced an energy partitioning ratio[26] $E_{\mathrm{k,d}}/E_{\mathrm{k,cm}} = \mathrm{We}_{\mathrm{d}}/\mathrm{We}$ (the equivalence here would require a different, but constant prefactor to be absorbed in the We_{d} definition, following Ref. [26] contrasting Ref. [72]) to translate between the two We numbers and the underlying kinetic energy in deformation vs translation. Given that both We numbers (We, We_{d}) play a role in the three-phase model, the introduction of the energy partitioning allows the final result (see below) to be expressed using only We.

3. **Stretching Phase** ($\tau_{\mathrm{i}} \leq t \leq t_{\mathrm{s}}$):

   We enter phase 3 when the droplet has truly deformed into a thin sheet, with $R/R_0 \gg 1$, accompanied by a significant thinning. The model assumes that the two opposing surfaces interact and couple, as their spacing satisfies the condition $\hat{h}\hat{k} \sim 1$ [26].

   For $t > \hat{\tau}_{\mathrm{i}}$, the wavenumber evolution is:

$$\hat{k}(\hat{t}) = \frac{\hat{k}_{\max}}{\hat{R}(\hat{t})}. \tag{4.5}$$

   The dynamics of the sheet expansion $\hat{R}(\hat{t})$ is well understood, and can at early times $\hat{t} \ll 1$ be approximated as [26]

$$\hat{R}(\hat{t}) = \sqrt{3\mathrm{We}_{\mathrm{d}}} \cdot \hat{t}, \tag{4.6}$$

   which with unity prefactor (following Ref. [26]) leads to:

$$k(\hat{t}) = \frac{(E_{\mathrm{k,cm}}/E_{\mathrm{k,d}})^{1/4}}{3\,\hat{t}R_0}. \tag{4.7}$$

   The corresponding amplitude of the modulations $\hat{\eta} = \eta/R_0$ follows from [26]

$$\hat{\eta}(\hat{t}) = \hat{\eta}_0 \hat{h}(\hat{t}) \mathrm{We} \left(\frac{E_{k,d}}{E_{k,cm}} \right)^{1/4} \hat{t}, \tag{4.8}$$

   where $\hat{h} = 4/3\,(R_0/R)^2$ is the average sheet thickness, and $\hat{\eta}_0$ is the initial perturbation amplitude. For this initial noise we find $\hat{\eta}_0 = 1.3 \times 10^{-2}$ as determined by Klein et al. [26] from experiments, assuming that the sheet punctures at a time $\hat{t}_b$ when $\hat{\eta}(\hat{t}_b) = \hat{h}(\hat{t}_b)$, with $\hat{h}$ determined from the average thickness ansatz. However, work by Liu et al. [25] has shown that the actual sheet thickness is significantly lower ($2 - 5\times$ depending on We and $\hat{t}$) than the average thickness, which proportionally reduces the initial noise value obtained by Klein et al. [26]. Consequently in the following we use a range $\hat{\eta}_0 = 3 - 7 \times 10^{-3}$.

From Eq. (4.7) we observe that the modulation wavelength is primarily a function of the non-dimensional time inversely proportional to the droplet radius and independent of the We number. We note that the energy partitioning ratio $E_{\mathrm{k,cm}}/E_{\mathrm{k,d}}$ weakly varies with laser pulse energy [26] (also see Ref. [102]). In the current analysis we may assume $(E_{\mathrm{k,d}}/E_{\mathrm{k,cm}})^{1/4} \approx 1$ [26]. At the apex of the sheet expansion trajectory, $\hat{t} \approx 0.38$ [72] we obtain a typical approximate modulation wavenumber $k \approx 1/R_0$. For the key data shown in Fig. 4.3 for a 31 µm diameter droplet, we obtain a predicted wavelength $\lambda \approx 110\,\mu\mathrm{m}$, a number that should in order of magnitude be compared to the several 10 µm in the experiments [e.g., we extracted 15 µm from Fig. 4.3(a)]. The corresponding amplitude of the modulations follows from Eq. (4.8), which gives $\eta \approx 40 - 90\,\mathrm{nm}$. This number should be compared to the order ~10 nm amplitude we obtain from the experiments. Of course, the relation Eq. (4.6) is a simplified description of the instantaneous sheet radius and instead we know that $\hat{R}(\hat{t}) = \sqrt{\mathrm{We_d}}\mathrm{P}(\hat{t})$ with known [72] polynomial $\mathrm{P}(\hat{t})$ which yields $\mathrm{P}(0.38) = 0.14$ and brings down the prediction to a closer match to the experiments with $\lambda \approx 42\,\mu\mathrm{m}$. However, the validity of using the instantaneous sheet radius to describe the stretching instead of Eq. (4.6) is an open question.

Finally, we qualitatively test the validity of the scaling relation in Eq. (4.7). Given the difficulty of obtaining reliable modulation wavelength over the various We numbers, we leave the detailed study of the We (in)dependence to future work. Instead, we focus our analysis on the proposed scaling $\sim \hat{t}R_0$ in the denominator. Figure 4.10 shows liquid tin sheets at $t \approx 0.33\tau_c$ for initial droplet sizes of (a) 37, (b) 50, and (c) 70 µm, with We remaining approximately constant (ranging from 850 to 1200) providing discrete concentric modulations. (To keep the underlying plasma physics scale-invariant, we scale the laser pulse duration with the initial droplet radius, keeping the ratio of acceleration time to acoustic time constant [69].) Each panel presents averaged shadowgraphs composed of 20 frames, with the front view (left half) and back view (right half) displayed side by side. The averaging improves the signal-to-noise ratio and underscores the high reproducibility of the observed patterns. To qualitatively validate the inverse linear dependency on droplet radius, we perform left/right comparisons of front-view acquisitions for droplets with low Weber numbers but varying initial sizes. Specifically, for the case of a droplet with an initial diameter of 37 µm, the left-side front view is scaled by the ratio of the initial diameter relative to the diameter of the comparison sheet's droplet at a similar time. The results are shown in Fig. 4.10(d, e, f).

For example, in Fig. 4.10(d), the left side of the 37 µm front view sheet is scaled by 45 µm/37 µm and compared with a mirrored left-side front view of a 45 µm droplet sheet. In this comparison, the sheets are not perfectly matched in size, which is simply attributed to (minor) differences in the Weber deformation number $\mathrm{We_d}$ and therefore the kinetic energy of deformation. When $\mathrm{We_d}$ values are more similar, as in Fig. 4.10(e, f), the sheet radii align more closely, and after scaling, the modulation reflection pattern is very nearly identical, underlying the proposed scaling $1/R_0$ of Eq. (4.7).

So far, we have found agreement on the order of magnitude of the modulations' wavelength and amplitude in comparing our observations to the three-phase R-T

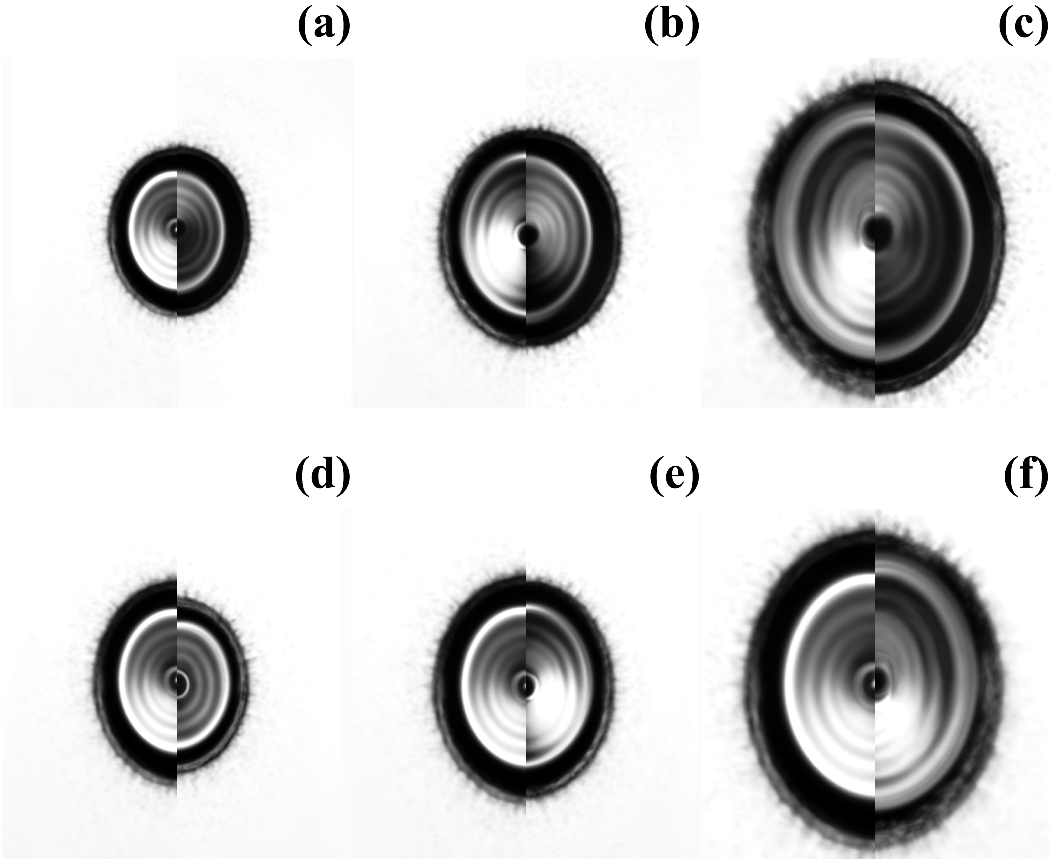

FIGURE 4.10: Front (left) and back (right) views around $t/\tau_c = 0.35$ of the following parameter sets [droplet diameter, laser pulse length, Weber number, and deformation Weber number] in (a) [37 µm, 10 ns, 1 200, 2 700], (b) [50 µm, 12 ns, 1 000, 2 700], (c) [70 µm, 20 ns, 850, 2 600]. Comparison of left side front views around $t/\tau_c = 0.33$ of [37 µm, 1 200, 2 600] with mirrored (d) [45 µm, 10 ns], 700, 1 900 (e) [50 µm, 12 ns, 1 000, 2 700], (f) [70 µm, 20 ns, 850, 2 600].

model, particularly so given the strong simplifications in the model, and experimental complexities in accurately determining wavelength and amplitude. However, there are still some observations that are not straightforwardly explained by the current model of the R-T instability. Firstly, we observe modulations that are predominantly cylindrically symmetric, indicating a suppression of azimuthal modulations at intermediate We numbers. This suppression could be explained by considering the (integer) number of azimuthal waves that need to fit on any individual radial wave. This explanation is partially supported by the observation that the azimuthal modulations are first observed on the outer radii [cf. Fig. 4.2(c)] where the larger circumference allows azimuthal modes to fit. Secondly, we find that new (concentric) modulations appear from the center region (cf. Fig. 4.3). This could hint at a driving mechanism separate from the early-time R-T instability, from which the hypothesis could be derived that the concentric modulations have an origin separate from the azimuthal ones. However, when azimuthal modulations are observed, they have a wavelength that is similar (same order) to the local concentric ones [cf. Fig. 4.2(c)] – such an implied coincidence would rather point towards a common R-T origin. Thirdly, we observe again that the modulation wavelength depends on the radial coordinate. Such implied *local* stretching, roughly proportional to the radial coordinate, is not captured in the current model [26], as may be expected given the assumption of a simple flat-disk geometry and uniform stretch [Eq. (4.5)]. Also, along with the radial local stretching, any temporal stretching dynamics is not adequately captured by the model. Lastly, as noted in Sec. 4.3.1, varying the Weber numbers results in different modulation patterns, although no definitive scaling could be obtained given the aforementioned difficulties of extracting a modulation wavelength from the data. Any visible changes may well be caused not by differences in the radial modulation wavelength, but rather by changing visibility of azimuthal modulations.

4.5 Conclusions

We present concentric surface modulations observed in reflection from both sides of laser-propelled and expanding liquid tin sheets, for droplets ranging from 27 to 70 μm in diameter at intermediate Weber numbers between 1 000 and 7 000. Through combined optical inspection in reflection and transmission modes, we determine that these surface modulations are only of order $\sim$10 nm in amplitude, on sheets with an average thickness of several 100 nm. The modulations appear predominantly front-back mirror symmetric (out-of-phase), and are highly reproducible.

We interpret these modulations as a manifestation of the instabilities that drive sheet breakup, as described by Klein et al. [26]. This study provides a clear and direct observation of such modulations. Furthermore, it reveals a (relatively) low-We counterpart of highly modulated sheets prior to sheet breakup. It provides experimental evidence of low-amplitude surface modulations in free-flying liquid sheets. We find qualitative agreement, in terms of the order of magnitude of the modulations' amplitude and wavenumber, with a model [26] based on a Rayleigh-Taylor instability that links the instantaneous wavenumber k to the system parameters, showing that $k(t/\tau_c)R_0 \sim (\tau_c/t)$, a scaling that is independent of the Weber number. Several aspects however remain insufficiently explained by the model such as (i) the concentricity of the perturbations and suppression of azimuthal modulation at low We number; (ii) the appearance of new modulations with time; (iii) the overall dynamics of the modulations. Moreover, there is a clear We number dependence of the visibility of azimuthal modes that is not yet understood. All such aspects have been brought to the forefront by the current work that is aimed to be a stepping stone for next works, which may include numerical studies, towards understanding the instability modes on thin sheets as produced from laser impact, a topic of particular relevance for stable target shaping in EUV lithography.

Acknowledgements

This work was conducted at the Advanced Research Center for Nanolithography (ARCNL), a public-private partnership between the University of Amsterdam (UvA), Vrije Universiteit Amsterdam (VU), Rijksuniversiteit Groningen (UG), the Dutch Research Council (NWO), and the semiconductor equipment manufacturer ASML and was partly financed by 'Toeslag voor Topconsortia voor Kennis en Innovatie (TKI)' from the Dutch Ministry of Economic Affairs and Climate Policy. This publication is also a part of the project 'Plasma driven by a variable-wavelength laser for next generation EUV sources for nanolithography' (with project number 19458) of the Open Technology Programme which is financed by NWO. We thank Hugo França, Randy Meijer, Arie den Boef, Dmitry Kurilovich, and Bo Liu for useful discussions and Laurens van Buuren for assistance on the setup.

Appendix A: Details measurements

Table 4.1 provides further details of the experiments discussed in the main text.

D_0 [μm]	d [μm]	τ [ns]	E [mJ]	t/τ_c	We	We$_d$	Fig.
31	100	10	5	0.2	800	1 200	4.2(a)
			10	0.2	1 700	2 300	4.2(b), 4.3 (a-d)
			15	0.24	3 100	4 200	4.1(g), 4.6(a), 4.7(a)
			15	0.38	3 100	4 200	4.1(h), 4.6(b), 4.7(b)
			25	0.2	4 700	5 800	4.2(c)
			50	0.2	12 000	10 600	4.2(d)
50	90	15	–	0.3	123 000	57 000	4.2(e,f)
		12	7.8	0.33	1 000	2 700	4.10(b)
27	100	10	Δ	0.4	7 000	–	4.8(c)
36	100	10	–	0.31	1 400	3 900	4.6 (a,b)
37	90	10	7.4	0.35	1 200	2 700	4.10(a)
45	90	10	6.4	0.35	700	1 900	4.10(e)
70	95	20	10	0.35	850	2 600	4.10(c)

TABLE 4.1: Details for shadowgraphs containing droplet diameter (D_0), beam spot size (d), pulse duration (τ), PP energy (E), non-dimensional time (t/τ_c), measured Weber number (We), measured Weber deformation number (We$_d$), and figure(panel) usage (Fig.).

Appendix B: Details setup

Figure 4.11 provides further details of the experimental setup.

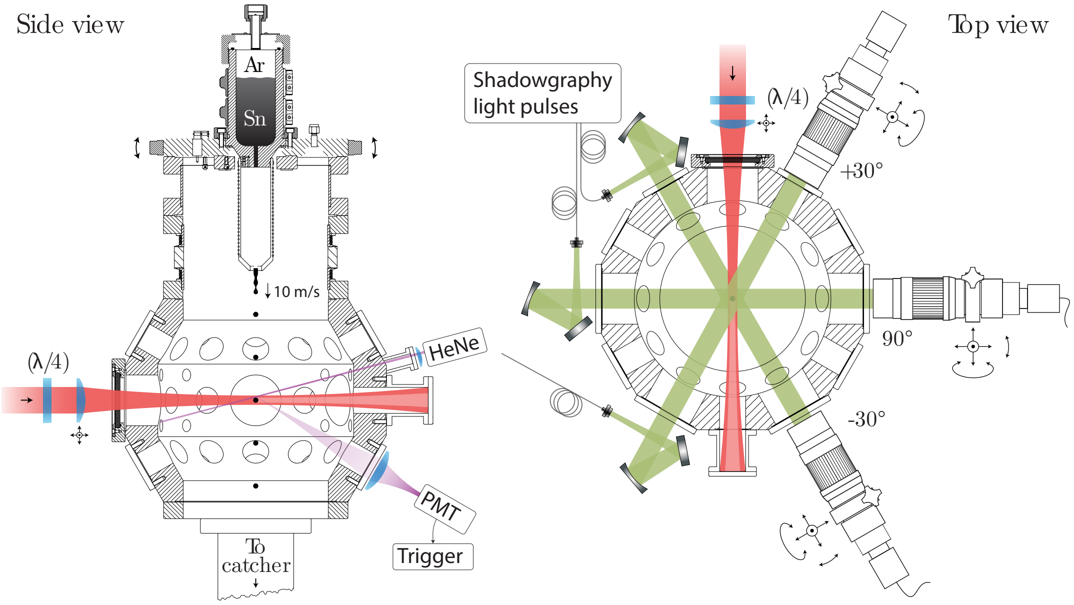

FIGURE 4.11: Schematic of the experiment. Figure modified from Ref. [106].

5

Chapter 5

Phase Transition of Surface Modulations on Free-Flying Liquid Tin Sheets

H.K. Schubert et al., in preparation.

We investigate the transition from concentric to azimuthal modulation patterns on expanding liquid tin sheets driven by laser-induced propulsion. Using time-resolved shadowgraphy, we systematically vary the Weber number by adjusting the prepulse energy, duration, and droplet size to determine the conditions that trigger this transition. Our results consistently reveal a phase transition: concentric modulations dominate at low Weber numbers, while azimuthal modulations emerge at higher values. The phase transition is gradual, with azimuthal features first appearing atop the concentric rings. Notably, once triggered, the azimuthal modulations persist throughout the droplet's deformation. We interpret this behavior within a Rayleigh-Taylor (R-T) framework proposed by Klein et al. [J. Fluid Mech. 893, A7 (2020)], which states that the modulation wavenumber is governed by the Weber number, with the initial amplitude set by the initial plasma-induced noise. However, from our preliminary analysis, we cannot explain the observed droplet-size and pulse-length dependence of the transition threshold energy. This study thus motivates further investigation into the mechanisms governing instability onset and mode selection in the transition between concentric and azimuthal modulations.

5.1 Introduction

Laser-induced modulation patterns on expanding liquid microdroplets are of particular relevance in applications such as extreme-ultraviolet (EUV) light sources and high-precision target shaping. Upon laser impact, a thin liquid sheet "target" rapidly expands from the initial droplet, during which surface instabilities can develop. These instabilities manifest as (thickness) modulations on the surface of the expanding sheet. We distinguish two primary types of modulations: *concentric* modulations, which appear as circular ripples centered on the original droplet axis, and *azimuthal* modulations, which appear atop concentric ripples and break the axisymmetry. In previous work [107], we identified that this phase transition is Weber number (We) dependent: concentric modulations dominate at low Weber numbers, while azimuthal modulations emerge at higher values. This transition was observed to be gradual; in the investigated cases, azimuthal features first appeared atop the outer concentric modulations. However, the underlying mechanism and its scaling behavior remained unclear. In particular, Schubert et al. [107] reported the observation of concentric surface modulations on thin tin sheets formed from laser pulse impact on tin microdroplets with diameters $D_0 = 27, 31, 45, 55,$ and 70 µm at intermediate Weber numbers ranging from $\sim 1\,000$ to $7\,000$. Optical inspection in both reflection and transmission modes revealed that these axisymmetric modulations, surprisingly robust and reproducible, had wavelengths on the order of 15 µm and amplitudes around 10 nm, appearing on sheets of radius 50 to several hundred µm and thickness $\sim$ 100 nm. These features were interpreted as a manifestation of a Rayleigh-Taylor (R-T) type instability at intermediate We, linking them to the more irregular breakup dynamics at higher We studied by Klein et al. [26], although several open questions remained.

In this study, we systematically investigate how the onset of azimuthal modulations depends on pulse duration (τ), droplet size (D_0), and prepulse energy (E_{pp}) using nanosecond time-resolved shadowgraphy. We revisit the three-phase (R-T) model [26] used in Schubert et al. [107] to interpret the observed concentric modulation patterns on expanding tin sheets but find no satisfactory explanation from the model in our preliminary analysis.

The remainder of this paper is structured as follows. Section 5.2 describes the experimental methods. Section 5.3 presents the shadowgraph data and threshold identification. Section 5.4 addresses the scalings of the modulation threshold, and Section 5.5 concludes with implications and future directions.

5.2 Experimental methods

For a description of the experimental setup, we refer the reader to our Ref. [107], from which the presented measurements originate. Briefly, a droplet generator produces a kHz stream of liquid tin microdroplets at a temperature of 270 °C, traveling at approximately $10\,\mathrm{m\,s^{-1}}$ in a vacuum environment with a base pressure of 10^{-7} mbar. A prepulse [PP, $\lambda = 1064$ nm, circularly polarized, Gaussian: $d_{\mathrm{foc}} \sim 100\mu m$] generates plasma upon interaction with a droplet, resulting in impulsive acceleration on the order of $10^{10}\,\mathrm{m/s^2}$. This drives the droplet to velocities of up to several 100 m/s, resulting in strong radial expansion and the formation of a thin liquid sheet. The sheet deformation has been studied in detail in several works [22, 23, 25, 39, 53, 70]. We employ nanosecond time-resolved shadowgraphy at 560 nm, using spatially and temporally incoherent illumination, to image the evolving tin sheet. Three cameras are positioned to capture side (90°), front (30°), and back (30°) views, each paired with an illumination source placed directly opposite the respective camera. For example, the front-view camera receives both direct light from its own opposing source and additional reflected light from the back-view illumination. We refer to this configuration as a *reflection mode* setup. Additionally, we employ a vaporization pulse [VP, $\lambda = 1064$ nm, circularly polarized, Gaussian: $d_{\mathrm{foc}} \sim 1000\mu$m] to gradually evaporate the expanding tin sheets [67, 107], enabling observation of transmitted light through the thinning material. This arrangement is referred to as a *transmission mode* setup.

In this study, we build upon previous work by systematically investigating how modulation dynamics are influenced by variations in E_{pp}(5–105 mJ), τ (6–30 ns), and D_0 (17, 27, 31, and 70 µm). We characterize the dynamics of droplet propulsion using the propulsion Weber number (We), which relates the droplet's inertial and surface tension forces:

$$\mathrm{We} = \rho U^2 D_0 \sigma^{-1}, \tag{5.1}$$

where $\rho = 7000\,\mathrm{kg/m^3}$ and $\sigma = 0.55\,\mathrm{N\,m^{-1}}$ are the density and surface tension of liquid tin, respectively. We extract the center-of-mass velocity (U) from side-view shadowgraphs along the droplet deformation. As we increase E_{pp}, more energy is deposited onto the droplets surface. The deposited energy on the droplet (E_{od}) accounting for the finite laser focus size and the spherical geometry of the droplet, is given by [31]:

$$E_{\mathrm{od}} = E_{\mathrm{pp}} \left(1 - 2^{-D_0^2/d_{\mathrm{foc}}^2}\right), \tag{5.2}$$

where d_{foc} is the effective focus diameter. The center-of-mass velocity U is known [31] to scale with the deposited energy E_{od} according to a power law:

$$U = K_U E_{\mathrm{od}}^{\alpha}, \tag{5.3}$$

with

$$K_U \approx 36 \left(\frac{25\,\mathrm{\mu m}}{R_0}\right)^{2.2} \left(\frac{\tau}{10\,\mathrm{ns}}\right)^{0.4} \mathrm{m/s/mJ^{\alpha}}.$$

with $\alpha = 0.6$ (experimentally determined). In summary, increasing E_{pp} increases E_{od}, which in turn increases U, and thus raises We cf. Eq. (1).

After the prepulse strikes the droplet, it begins to deform into a sheet-like structure on an inertial timescale $\tau_{\mathrm{i}} = D_0/U$. The subsequent evolution proceeds over the capillary timescale $\tau_{\mathrm{c}} = \sqrt{\rho D_0^3/6\sigma}$, which characterizes the expansion and retraction of the sheet due to surface tension forces acting on the rim [22, 23, 39].

5.3 Results

In the following, we first examine the transition from concentric to azimuthal modulation patterns as a function of Weber number over time. We then investigate this transition across different pulse durations for a fixed droplet size by varying the laser energy, at representative times during droplet deformation for two droplet sizes. Finally, we discuss the conditions under which the concentric-to-azimuthal transition occurs.

Prior studies demonstrated that the Weber number We governs the mode selection of a (R-T) instability [26, 107]. Figure 5.1 presents the temporal evolution of the modulation patterns, shown as a function of normalized time (t/τ_{c} increasing left to right) for four distinct Weber numbers (We increasing from top to bottom). We vary the Weber numbers by adjusting the PP energy, while keeping both the PP duration ($\tau = 10\,\mathrm{ns}$) and the droplet diameter ($D_0 = 31\,\mathrm{\mu m}$) constant. Increasing the PP energy translates into an increase of the propulsion velocity and thus into an increase of Weber number (see Eq. 5.1).

At lower Weber numbers (e.g., for We = 1 700 and We = 2 200), the droplet exhibits a concentric reflective pattern, as discussed in prior work [107]. In contrast, at higher Weber numbers (e.g., for We = 17 900), the pattern is fully azimuthally modulated. Fully azimuthal modulations lead to hole formation at late times (see at We = 17 900) as investigated by Klein et. al [26]. It is worth noting that at higher Weber numbers, the resulting sheet is also significantly larger as the center-of-mass propulsion U is related to a radial expansion velocity $\dot{R}_0$ such that, typically, $\dot{R}_0/U \geq 1$ [24]. We

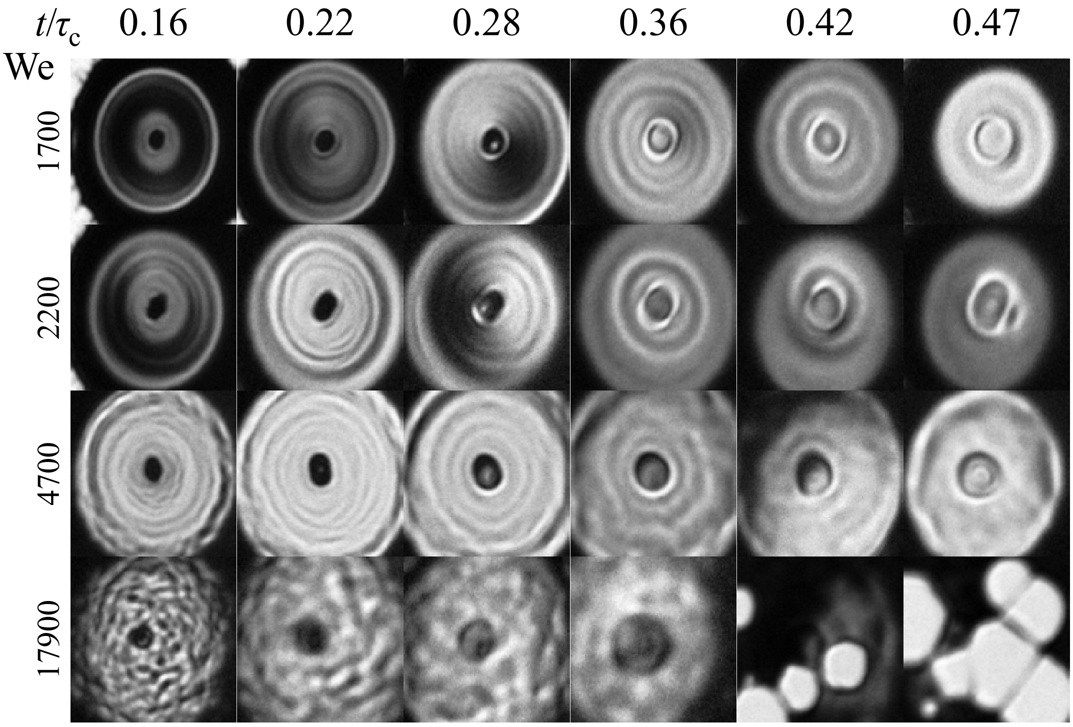

FIGURE 5.1: Shadowgraphs for Weber number (We; increasing top to bottom) and dimensionless time (t/τ_c; increasing left to right), for a 31 µm diameter tin droplet impacted by a 10 ns prepulse.

observe that at We $\approx$ 4 700, azimuthal modulations consistently emerge atop concentric patterns on the sheet surface at early times (e.g., at $t/\tau_c = 0.16$). These azimuthal features appear on top of concentric surface modulations. We interpret the simultaneous emergence of both concentric and azimuthal modulations as a threshold phenomenon.

Crucially, we find (cf. Fig. 5.2) that once azimuthal modulations appear atop of concentric modulations, they persist throughout the entire droplet deformation process. This suggests that the transition from concentric to azimuthal structures is not primally driven by the temporal evolution of the sheet, but is instead determined at an early stage, likely during or shortly after the prepulse–droplet interaction. We therefore conclude that the onset of azimuthal modulation is effectively *time-independent*, and classify the modulation type for a given Weber number as concentric, threshold, or azimuthal, based on observations made up to the apex of the sheet expansion ($t/\tau_c \approx 0.4$).

In the previous work [107] we concluded with a 1-D ray-tracing model that the observable reflective region with our imaging system corresponds to surface angles below approximately 1°. Notably, the reflective area evolves during the target deformation but remains centered and consistently smaller than the full sheet radius. Initially, the radial growth of the reflective area follows the sheet expansion but peaks before the sheet reaches its maximum radius. Additionally, concentric ripples stretch over time (see Fig. 5.2, We = 1 700, between $t/\tau_c \approx 0.2$ and $t/\tau_c \approx 0.4$). We do not further analyze these secondary effects in this work, as the goal is to only identify the criteria for the onset of azimuthal modulations. Note, for We = 17 900, the shadowgraph images appear increasingly blurred over time. This is due to the imaging plane in the shadowgraphy setup not being perfectly adjusted to follow the rapidly evolving shape of the deforming target.

Figure 5.2 presents shadowgraphs of a 27 µm diameter droplet subjected to various pulse durations ($\tau = 6$–20 ns; increasing from left to right) and increasing prepulse energies E_{pp} (from top to bottom), with one representative frame shown for each case. We organize the rows by E_{pp} rather than Weber number, as the latter varies for each specific combination of τ and E_{pp} due to the dependency on the scaling factor K_U in Eq. 5.3. Reflection-mode shadowgraph images are shown for 6, 8, and 10 ns pulses, captured at approximately $t/\tau_{\mathrm{c}} \approx 0.2$, while transmission-mode shadowgraph images are shown for 10, 15, and 20 ns pulses, recorded around $t/\tau_{\mathrm{c}} \approx 0.4$. For a given droplet size, long pulses lead to pronounced sheet curvature effects [108], which limits imaging in reflection mode. By utilizing both reflection and transmission imaging modes, we are able to investigate a broader range of pulse durations τ across various droplet diameters D_0. Therefore, we employ transmission-mode imaging to mitigate visibility limitations in reflection mode for large pulse lengths. The image crops are adjusted individually to best highlight the relevant sheet features for each pulse duration.

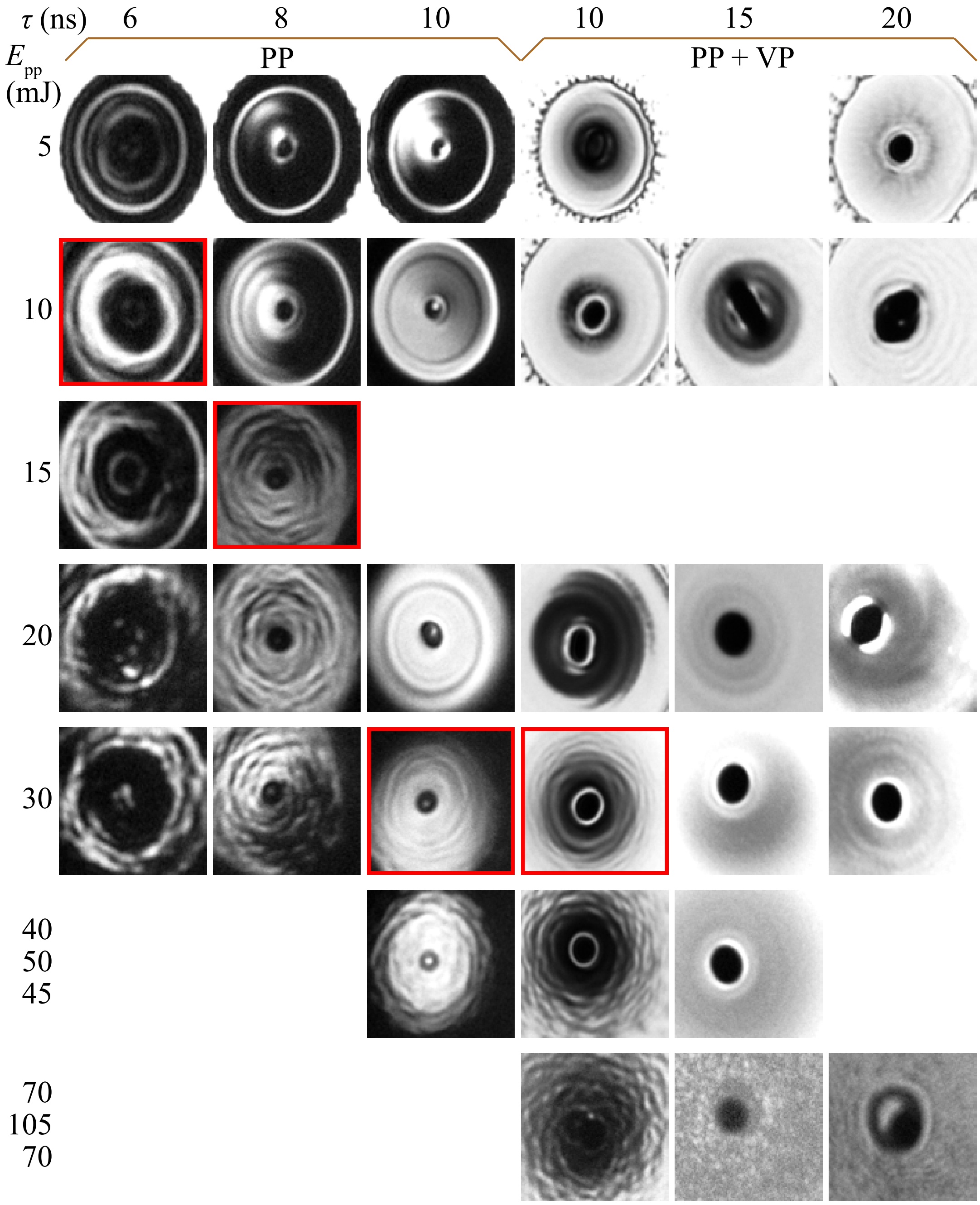

FIGURE 5.2: Shadowgraphs of a 27 μm diameter droplet subjected to varying pre-pulse durations (τ; increasing from left to right) and energies (E_{pp}; increasing from top to bottom). Reflection-mode shadowgraphs (only PP) are captured around $t/\tau_c \approx 0.2$, while transmission-mode shadowgraphs (PP + VP for visualization) are recorded around $t/\tau_c \approx 0.4$. Threshold cases are framed in red. Note that the last two rows each contain multiple E_{pp} values; these values are arranged top to bottom in the same order as left to right in the corresponding shadowgraphs.

Given the temporal stability for the onset of azimuthal modulations established in Fig. 5.1, and the similarity of features observed in both reflection and transmission modes at 10 ns, we confirm that transmission imaging, despite being captured at a later time, is equally suitable for identifying the modulation type. We highlight frames with a red square to indicate what we identify as a threshold case. Note that, after the onset, the spreading of azimuthal modulations over the sheet occurs gradually with increasing PP energy. Overall, we find that the phase transition occurs at lower E_{th} values for shorter τ, suggesting that the onset of azimuthal modulation is at least in part governed by PP intensity (see Discussion Sec. 5.4). For 15 ns and 20 ns pulse durations, concentric modulations persist up to 45 mJ and 30 mJ, respectively, without clear evidence of azimuthal onset. Notably, at the highest investigated energies for these durations (105 and 70 mJ), the resulting patterns deviate from purely concentric modulation but also differ qualitatively from the fully azimuthal cases observed at 10 ns and 70 mJ. This suggests that either the phase transition is not fully achieved at longer pulse durations, or the resulting azimuthal modulation amplitudes remain significantly lower under these conditions.

Similarly, Fig. 5.3 presents the modulation transition for three pulse durations (12, 15, and 20 ns) at a larger D_0 (70 µm). Although a similar trend of a lower E_{th} for shorter τ is observed, the absolute threshold energies differ when comparing the 27 and 70 µm diameter droplet cases. This suggests that a (yet hypothetical) critical intensity required for the onset of azimuthal modulation is dependent on the droplet size.

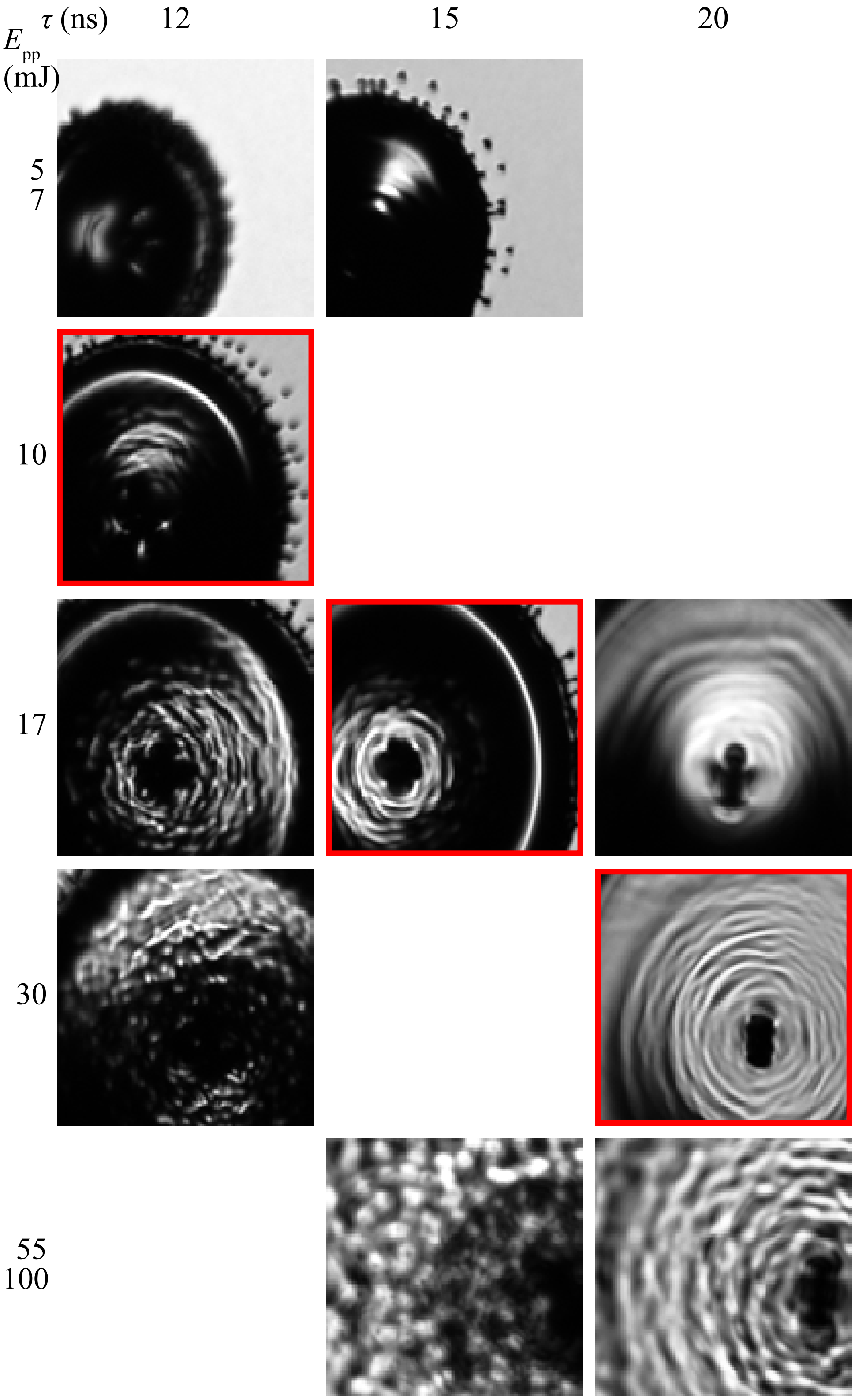

FIGURE 5.3: Shadowgraphs of a 70 µm diameter droplet subjected to varying pre-pulse durations (τ; increasing from left to right) and energies (E_{pp}; increasing from top to bottom). For cases with two energies in the same row, the upper value corresponds to the leftmost shadowgraph. Reflection-mode shadowgraphs are captured around $t/\tau_c \approx 0.2$.

5.4 Discussion

In the following, we quantitatively analyze the transition cases and revisit the three-phase Rayleigh-Taylor (R-T) instability model of Klein et al. [26].

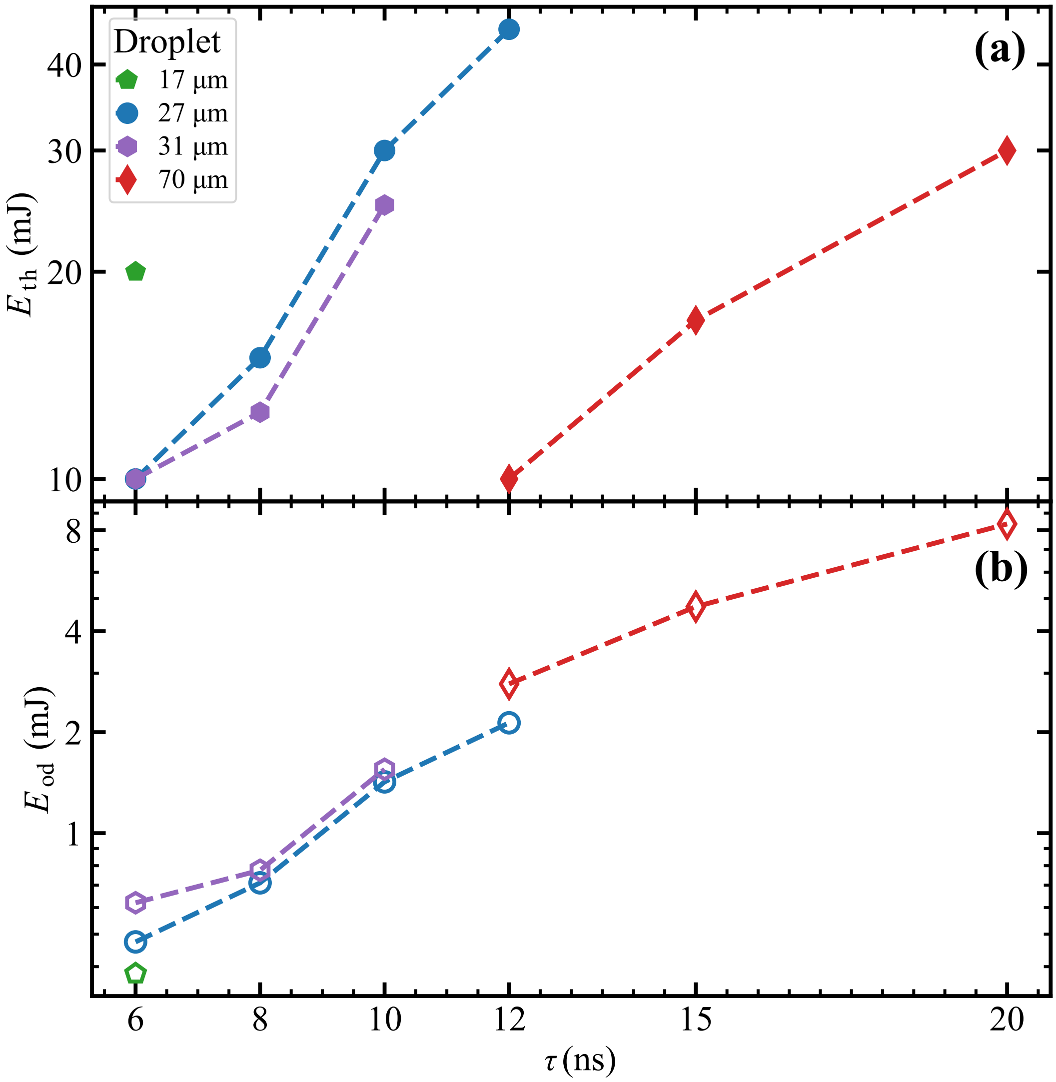

FIGURE 5.4: (a) Modulation threshold prepulse energy $E_{\rm th}$ (onset of azimuthal modulations atop concentric patterns) as a function of pulse duration for various droplet sizes. (b) Effective energy deposited on the droplet ($E_{\rm od}$) as a function of pulse duration (τ).

To quantitatively assess the suggested intensity dependence on droplet size, Figure 5.4(a) shows the modulation threshold energy $E_{\rm th}$ as a function of pulse duration τ for various droplet sizes D_0, including the exemplary cases of $D_0 = 27\,\mu$m and $D_0 = 70\,\mu$m, along with additional cases for which the onset of azimuthal modulation was similarly identified. This plot demonstrates that no universal threshold energy $E_{\rm th}$ exists for a given pulse duration. For a fixed D_0, shorter τ yield lower $E_{\rm th}$, suggesting an intensity-driven transition. However, it is also clear that any such threshold intensity appears to be a function of the size of the droplet (given that a similar $E_{\rm th}$ is required for large and small droplets but at very different values for τ). This trend looks similar for the Weber number, given its relation to $E_{\rm pp}$ (see Eq. 5.1, 5.2, and 5.3) cf. Fig. 5.5 in the Appendix. However, since larger droplets overlap more of the PP beam, it is instructive to consider the actual deposited energy on the droplet, given also that prior studies e.g. on droplet propulsion have found this deposited energy to be the key governing quantity. Therefore, in Figure 5.4(b), we plot the deposited energy E_{od}, calculated from the threshold energy using Eq. 5.2, for each droplet–laser pulse duration combination. We observe that the E_{od} values converge across different D_0 onto a common trend. This plotting may help explain why larger droplets require lower E_{th} for the same pulse duration, as they absorb a greater fraction of the laser energy. However, energy deposition alone does not alone govern the modulation threshold, and the threshold itself appears to be intensity dependent.

In an attempt to better understand the threshold behavior, we next revisit R-T model proposed by Klein et al. [26], which predicts surface modulation wavenumbers k, amplitudes η, and the eventual sheet hole formation time. This three-phase R-T model was employed previously by Schubert et al. [107] to interpret the observation of fully concentric surface modulations on tin sheets, finding qualitative agreement between theory and experiment. Briefly, the R-T instability cf. [26] requires an acceleration normal to the fluid interface, provided in our case by plasma pressure acting orthogonally on the initially undeformed droplet surface. This defines phase 1 of the model, where initial perturbations are seeded. Once the laser pulse ends, the external acceleration ceases, halting further mode amplification. In phase 2, permitted perturbations grow only inertially, driven by the momentum transferred during phase 1. In phase 3, both the sheet and its surface modulations undergo radial stretching, eventually leading to hole formation and the onset of sheet rupture. The resulting expression for the dominant modulation wavenumber evolution in the final, stretching phase 3, is given by:

$$k(\hat{t}) = \frac{\left(E_{\mathrm{k,cm}}/E_{\mathrm{k,d}}\right)^{1/4}}{3\,\hat{t}R_0}, \tag{5.4}$$

where R_0 is the initial droplet radius, and $\hat{t}= t/\tau_{\mathrm{c}}$ is the dimensionless time. We introduce the energy partitioning [26, 107]

$$E_{\mathrm{k,d}}/E_{\mathrm{k,cm}} = \mathrm{We_d}/\mathrm{We}, \tag{5.5}$$

to translate between the two Weber numbers and the underlying kinetic energy in deformation vs translation. In the following, we present a hypothesis based on the wavenumber and amplitude predicted by the R-T model.

First principle reasoning

From first principles, the observation of higher wavenumbers at higher Weber numbers is not unexpected, as the R-T model predicts the fastest-growing mode at the end of phase 2 to be

$$\hat{k}_{\mathrm{max}} = \frac{\mathrm{We}^{1/4}}{\sqrt{3\hat{\tau}_{\mathrm{i}}}} \sim \sqrt{\mathrm{We}}. \tag{5.6}$$

Given that the Weber number correlates with the deposited laser energy as $\mathrm{We} \sim U^2 \sim E_{\mathrm{od}}^{1.2}$, one can hypothesize that higher wavenumbers become accessible at higher E_{od} and appear atop the concentric modes, as $\hat{k}_{\mathrm{max}} \sim E_{\mathrm{od}}^{0.6}$. This reasoning is in line with Ref. [107], where a suppression of azimuthal modulations at intermediate Weber numbers was hypothesized to be due to the (integer) number of waves that would need to fit on a concentric wave. However, it does not explain why the modulation threshold E_{od} depends on droplet size and increases with pulse duration.

Amplitude Ansatz

Therefore, we take as a first Ansatz that there is a critical *amplitude* that defines when the transition to azimuthal modulations occurs. The normalized modulation amplitude $\hat{\eta} = \eta / R_0$ evolves from the initial noise as [26]:

$$\hat{\eta}(\hat{t}) = \hat{\eta}_0 \hat{h}(\hat{t}) \mathrm{We} \left(E_{\mathrm{k,d}} / E_{\mathrm{k,cm}} \right)^{1/4} \hat{t}, \tag{5.7}$$

where $\hat{\eta}_0$ is the initial perturbation amplitude, $\hat{h}(\hat{t})$ represents the normalized sheet thickness evolution, and We is the Weber number. This instantaneous modulation amplitude rewritten by substituting $\hat{h}(\hat{t}) \sim \hat{R}(\hat{t})^{-2} \sim \mathrm{We_d}^{-1} \hat{t}^{-2}$ so we find:

$$\hat{\eta}(\hat{t}) \sim \hat{\eta}_0 (\mathrm{We}/\mathrm{We_d}) \left(E_{\mathrm{k,d}} / E_{\mathrm{k,cm}} \right)^{1/4} 1/\hat{t}, \tag{5.8}$$

which, taking into account the energy partitioning [cf. Eq. 5.5], is independent of the Weber number:

$$\hat{\eta}(\hat{t}) \sim \hat{\eta}_0 \left(E_{\mathrm{k,d}} / E_{\mathrm{k,cm}} \right)^{-3/4} 1/\hat{t}. \tag{5.9}$$

We may hypothesize that the threshold behavior can be captured in the form of a threshold amplitude exceeded at early times. However, from the above equation, it becomes clear that the instantaneous modulation amplitude is Weber number- and droplet size-independent apart from a weak, indirect dependence via the energy partitioning. From previous studies [102] we know that $E_{\mathrm{k,d}} / E_{\mathrm{k,cm}}$ increases with droplet size all other things remaining constant and assuming a finite focal size. Thus, this dependence on the energy partitioning in Eq. 5.9, again with all other things being constant, leads to a reduced amplitude for the bigger droplets. This dependence does not lead to any insight into why the threshold amplitude would *reduce* with the size of the droplet. Thus, our hypothesis leads to the conclusion that the initial "thermal" noise amplitude, $\hat{\eta}_0$, sets the threshold, defining a critical initial noise amplitude $\hat{\eta}_{0,c}$ that is independent of time. This is consistent with our observation that the threshold behavior is independent of the observation time (see Fig. 5.1, limited to phase 3). Naively, we may expect a dependence of this initial noise on the laser intensity via the plasma temperature near the surface $\eta_0 \sim T \sim \sqrt{I}$ which, however, again does not lead to insight into why the critical intensity would *reduce* with the size of the droplet.

In sum, we find from our preliminary analysis, in terms of the three-phase R-T model in tandem with our Ansatz of a critical modulation amplitude, no overall explanation of the key observations in this study. Alternative Ansatzes or dedicated numerical simulations may yield new insights into the underlying mechanisms and should be explored in future work.

5.5 Conclusion

In this study, we investigated the onset of azimuthal modulation patterns on laser-impacted tin droplets by systematically varying the Weber number, pulse duration, and droplet size. Time-resolved imaging reveals a gradual transition from concentric to azimuthal modes, with azimuthal features appearing early and persisting throughout the deformation. We revisit the Rayleigh-Taylor (R-T) framework with which we, in previous work, qualitatively found agreement with wavenumbers for concentric sheet perturbations for intermediate Weber numbers. The R-T model predicts $\hat{k}_{\mathrm{max}} \sim \mathrm{We}^{1/2}$ at the end of phase 2, suggesting that higher perturbation modes become accessible at higher E_{od} and emerge atop the concentric pattern. However, this does not straightforwardly explain why the modulation threshold E_{od} depends on droplet size and increases with pulse duration. Also the Ansatz of a critical modulation amplitude underlying the transition does not explain the transition threshold. Our findings motivate future high-resolution simulations to better resolve the underlying physics and support improved control in applications such as EUV light generation.

Acknowledgments

This work was conducted at the Advanced Research Center for Nanolithography (ARCNL), a public-private partnership between the University of Amsterdam (UvA), Vrije Universiteit Amsterdam (VU), Rijksuniversiteit Groningen (UG), the Dutch Research Council (NWO), and the semiconductor equipment manufacturer ASML, and was partly financed by 'Toeslag voor Topconsortia voor Kennis en Innovatie (TKI)' from the Dutch Ministry of Economic Affairs and Climate Policy. The authors were supported, in part, by funding from the European Research Council (ERC) under the European Union's Horizon 2020 research and innovation programme under grant agreement No 802648.

Appendix

We reprint Fig. 5.4(a) below with the y-axis showing the propulsion Weber number instead of the (directly correlated) threshold pulse energy E_{th}. The relation between Weber number and the pulse energy E_{pp}, given a pulse duration and droplet diameter, can be obtained (assuming for simplicity $d_{\mathrm{foc}} \gg D_0$) combining Eqs. 5.1, 5.2, and 5.3 in We $\sim U^2 D_0 \sim (K_U E_{od}^{0.6})^2 D_0 \sim E_{\mathrm{pp}}^{1.2} \tau^{0.8} / D_0$. The Fig. 5.5 shows trends identical to those presented in Fig. 5.4(a) in the main text and enables the direct conclusion that any critical Weber number is a function of both pulse duration as well as droplet size.

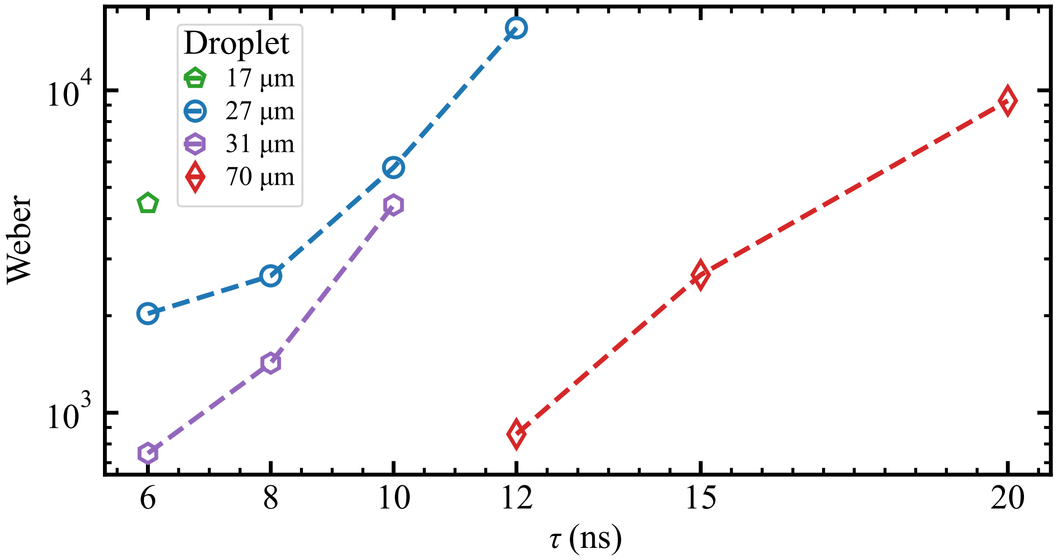

FIGURE 5.5: Modulation threshold Weber (onset of azimuthal modulations atop concentric patterns) as a function of pulse duration for various droplet sizes.

6

Chapter 6

Conclusions & Outlook

This thesis investigates laser-matter interactions that govern the dynamic response of liquid tin droplets and expanding sheets to pulsed laser irradiation. These interactions are directly relevant for optimizing target design in next-generation extreme-ultraviolet (EUV) nanolithography systems. The central aim is to understand how liquid tin responds to the vaporization pulse (VP) and prepulse (PP), both of which play a critical role in shaping and controlling the morphology of tin targets before exposure to the high-energy main pulse (MP). From this overarching objective, two fundamental research questions emerge:

1. What are the governing mechanisms in the interaction between a nanosecond laser pulse and a free-flying liquid tin sheet?
2. What causes the surface modulations observed on expanding free-flying liquid tin sheets?

Through a series of carefully designed experiments and supporting numerical models, this thesis provides a detailed exploration of these two questions across four main Chapters.

6.1 Summary of findings

Chapter 2 investigated the vaporization behavior of flat liquid tin sheets subjected to low-intensity vaporization pulse (VP) irradiation (100 ns temporal and spatial box pulse). By combining time-resolved shadowgraphy with a resolution of 5 ns and a 1-D numerical heating and vaporization model, we identified the vaporization process as gradual and governed by the Hertz–Knudsen equation. We established a clear linear relationship between the vaporization rate and the laser intensity $\dot{h} = A \cdot I_{\mathrm{VP}}$, where the proportionality constant $A = 1.0(3)\,10^{-7}\,\mathrm{ms}^{-1}/\mathrm{Wcm}^{-2}$ was determined by fitting the experimental data. Our findings indicate that within the investigated VP intensity range, the vaporization dynamic is governed solely by the deposited laser fluence. We find good agreement between experimental observations and simulations, confirming the predictive capability of our model and offering valuable insights for future laser-based target-shaping strategies.

In **Chapter 3**, we investigated plasma formation on expanding sheets under higher-intensity VP irradiation (compared to the previous Chapter). We found that plasma formation is localized and thickness-dependent, initiating at the center where conditions first satisfy the breakdown threshold, and subsequently propagating outward. A reproducible inflection point in the temporal photodiode transmission signal characterizes the onset of plasma formation. The time of this inflection scales approximately as the bulk plasma onset time $\sim I_{\mathrm{VP}}^{-2}$. These findings provide experimental evidence for local plasma dynamics and underscore the importance of pulse shaping and intensity control in target design.

Chapter 4 focused on concentric surface modulations observed on laser-propelled liquid tin sheets at intermediate Weber numbers. These nanometric symmetric features were found to be highly reproducible and aligned well with predictions from a Rayleigh–Taylor instability model proposed by Klein et al. [26], which describes the evolution of modulation wavenumber, timing, and eventual sheet breakup. Our experimental results offer direct validation of this model in the pre-breakup regime and demonstrate that the intermediate Weber number domain provides a well--controlled setting for systematically studying surface modulation dynamics with high precision.

Chapter 5 built upon the findings of the previous Chapter by systematically varying droplet size, prepulse energy, and duration to investigate the transition from a phase of fully concentric modulations to a phase where azimuthal modulation patterns appear atop the concentric ones. Our results reveal that azimuthal modulations emerge at higher Weber numbers and initially overlay the outer concentric features. We find that the transition from concentric to azimuthal is gradual in nature and time-independent once established. The transition hints at a critical intensity that is droplet-size dependent. These findings enhance our understanding of fluid instabilities in rapidly expanding liquid sheets and provide further insight into the modulation dynamics across different energy regimes.

Taken together, the four Chapters reveal a coherent picture of how laser parameters can be systematically tuned to manipulate the response of liquid tin targets. The first two Chapters show that vaporization and plasma formation are not only intensity-dependent but also spatially and temporally localized processes that can be accurately modeled and predicted. This establishes a foundation for designing precise laser pulse-based strategies for shaping the liquid tin.

The final two Chapters demonstrate how relatively subtle changes in laser prepulse parameters result in variations in surface modulations. At lower prepulse energies, these modulations are strikingly concentric, while at higher energies, azimuthal modulations appear atop the concentric ones as a result of underlying hydrodynamic instabilities. These modulations provide insight into instability modes in thin sheets produced by laser impact, a topic of particular relevance for stable target shaping in EUV nanolithography.

Importantly, the interplay between the findings of the two research questions highlights a unified theme: *control through understanding*. This thesis provides a robust foundation for laser pulse-tin interactions. It offers a comprehensive characterization of laser-induced thermal and plasma dynamics of liquid tin sheets, as well as hydrodynamic instabilities on their surfaces. These insights contribute to the physics of laser-driven fluids and also hold direct relevance for industrial-scale applications in EUV nanolithography.

6.2 Addressing the research questions

Accordingly, we now address the questions posed at the beginning of this thesis:

1. The interaction between a vaporization pulse and a liquid tin sheet is governed by the local sheet thickness and laser intensity. At low intensities, vaporization is gradual and fluence-driven, while at higher intensities, plasma formation occurs abruptly once a critical thickness-intensity threshold is met. Plasma initiates at thick sheet parts (centrally and rim) and propagates radially on a nanosecond time scale, a dynamic captured both in imaging and photodiode data.

2. Surface modulations on liquid tin sheets arise from instability dynamics that depend on the Weber number. At lower prepulse intensities, concentric patterns emerge, in qualitative agreement with descriptions by a Rayleigh-Taylor (R-T) instability model. At higher intensities, azimuthal modes occur atop concentric modulations, marking a phase change that may reflect a shift in the dominant instability wavenumber. This phase transition is intensity-dependent (with a threshold intensity that depends on droplet size) and time-independent once initiated. From our preliminary analysis, using the three-phase R-T model in tandem with the Ansatz of a critical amplitude, we find no satisfactory explanation for these observations. These findings motivate further research.

Together, these findings contribute to a more comprehensive understanding of how laser pulses interact with deformable liquid targets. The methods and models developed here offer robust tools for the further development of advanced target schemes in EUV applications.

6.3 Outlook

The insights gained from this thesis are relevant to both fundamental fluid dynamics and applied laser-matter interaction research. From a technological perspective, the characterization and control of tin target morphology are essential for applications such as extreme-ultraviolet (EUV) lithography, and they support the design of tailored laser pulses for advanced target shaping. Future work should aim to refine plasma diagnostics, enhance pulse-shaping capabilities, and advance understanding of modulation instabilities through numerical fluid-dynamics simulations, e.g., using BASILISK C.

Simulations.—In the following, we present preliminary simulation results of modulation instability for two Weber numbers (see Fig. 6.1) and qualitatively compare them to the three-phase model proposed by Klein et al. [26]. These simulations have been conducted within our group by Pires using BASILISK C and illustrate the mode selection process on the inertial time scale t_i.

In the simulations presented in Fig. 6.1, the driving surface pressure is defined as

$$p_s(t,\theta) = A(t) \cdot f(\theta,t),$$

where $A(t)$ is a time-dependent pressure amplitude modeled as a Gaussian pulse:

$$A(t) = A_\mathrm{max} \cdot \exp\left(-\frac{(t-t_c)^2}{2\sigma^2}\right),$$

and the angular pressure distribution is given by:

$$f(\theta, t) = f_0(\theta) + \alpha \cdot n(\theta, t),$$

with $f_0(\theta)$ the normalized pressure profile (we here take a raised cosine function following Ref. [108]) and the noise term $\alpha \cdot n(\theta, t)$ that introduces small-scale perturbations, where α is the amplitude of the noise perturbation, set to a small percentage relative to the peak pressure, and $n(\theta, t)$ is a normalized (white) noise field. Note that for the following simulations, a constant noise amplitude is applied across the pressure profile.

The y-axis in Figure 6.1 indicates the non-dimensional wavenumber $\hat{k} = kR_0$, the x-axis shows the normalized time t/τ_i, and the amplitude is plotted along the z-axis on a logarithmic scale, ranging from 0.1 (dark blue) to 100 (yellow). The red line marks the minimum resolvable spatial frequency, corresponding to the sheet radial size $2\pi/R$.

Comparison.—To enable the direct comparison between the simulation results and the theoretical predictions of the three-phase R-T model (cyan line) in Fig. 6.1, we rearrange and combine the relevant equations to express the dominant wavenumber in terms of simulation parameters, such as the Weber number and the inertial time scale. Briefly, the three-phase R-T instability model of Ref. [26] assumes an acceleration normal to the fluid interface, provided in our case by plasma pressure acting orthogonally on the initially undeformed droplet surface. In phase 1 of the model, the droplet undergoes an impulsive acceleration during which initial perturbations are seeded ($0 \leq t \leq \tau_\mathrm{e}$), with τ_e as the duration of the laser pulse. Once the laser pulse ends, the external acceleration ceases. In phase 2, the droplet expands into a sheet and the permitted perturbations grow inertially ($\tau_\mathrm{e} \leq t \leq \tau_\mathrm{i}$) with τ_i as the inertial time of the droplet. In phase 3, both the sheet and its surface modulations undergo radial stretching, eventually leading to hole formation ($\tau_\mathrm{i} \leq t \leq t_\mathrm{s}$) with t_s as sheet breaking time. The dominant wavenumber $k(\hat{t}) = k(t/\tau_\mathrm{c})$ according to the three-phase R-T model [26] is given by:

$$k(\hat{t}) = \frac{(E_\mathrm{k,cm}/E_\mathrm{k,d})^{1/4}}{3\hat{t}R_0} \sim \frac{1}{3\hat{t}R_0} \tag{6.1}$$

where we simplify by assuming $E_\mathrm{k,cm}/E_\mathrm{k,d} \sim 1$. In the simulation, the capillary time scale is defined as $\tau_\mathrm{c}^\mathrm{sim} = \rho R_0^3/\sigma$ and the Weber number is given by $\mathrm{We}^\mathrm{sim} = \rho U^2 R_0 \sigma^{-1}$, where R_0 and U denote the droplet radius and propulsion, respectively. The inertial time scale is defined as $\tau_\mathrm{i}^\mathrm{sim} = R_0/U$. Combining these expressions, we yield the following relation between capillary and inertial time:

$$\hat{t} = t/\tau_\mathrm{c}^\mathrm{sim} = \mathrm{We}^{-1/2} t/\tau_i^\mathrm{sim}. \tag{6.2}$$

Note that the Weber number is defined slightly differently here compared to previous Chapters, differing by a factor of 2 due to the use of the droplet *radius* rather than the *diameter*. As a result, the simulated Weber numbers (see Fig. 6.1) correspond to experimental values, as reported in the previous Chapters, of approximately 2000 and 5000, respectively. To compare the simulation with the R-T model [see Eq. 6.1], we relate the capillary time scales used in simulation and experiment:

$$\tau_\mathrm{c}^\mathrm{exp} = \sqrt{\frac{4}{3}}\,\tau_\mathrm{c}^\mathrm{sim}. \tag{6.3}$$

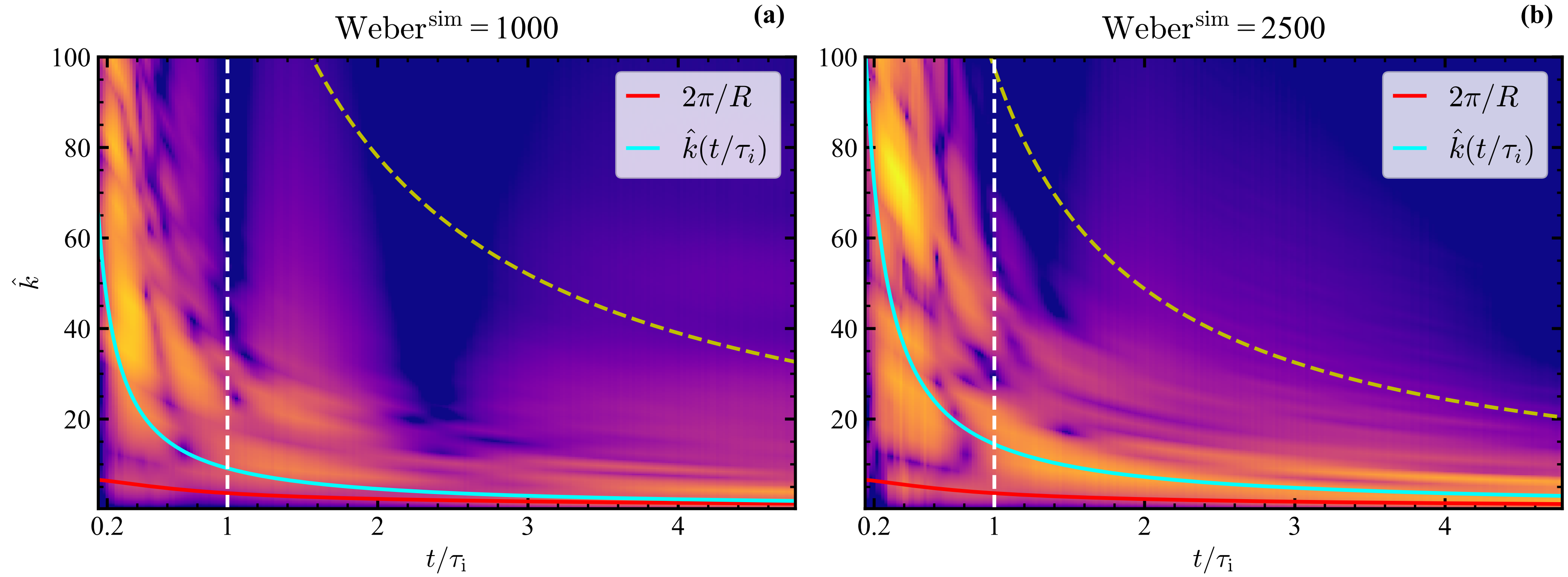

FIGURE 6.1: Simulation results for Weber numbers 1000 and 2500. The red line indicates the minimum resolvable frequency, $2\pi/R$, and the cyan curve shows the dominant frequency predicted by the Rayleigh–Taylor model [see Eq. 6.4]. The yellow dashed line indicates the experimentally determined wavenumber (see previous Chapter 4), which is backpropagated assuming a temporal stretching behavior $\sim 1/\hat{t}$ from its point of determination. The vertical dashed white line at $t/t_i = 1$ marks the end of phase 2, according to the definition provided by the R-T model [26].

Substituting Eq. 6.3 and Eq. 6.2 into Eq. 6.1, we obtain the normalized wavenumber:

$$\hat{k}(\hat{t}) = k(\hat{t})R_0 = \frac{\sqrt{3}}{6} \cdot \frac{\sqrt{\mathrm{We}}}{t/\tau_\mathrm{i}}. \tag{6.4}$$

A first comparison between the simulations the R-T model in Fig. 6.1 highlights a similarity in the scaling of the dominant wavenumber with time. Additionally, we find reasonable agreement for the dominant wavenumber (at late times in the simulations) with the R-T predictions (cyan line), especially for the higher Weber number case (Fig. 6.1(b)). A further preliminary analysis of the simulations (including cases with a higher We number not shown) reveals that, at the same times ($\hat{t}$ non-dimensionalized in the capillary time), the dominant perturbation wavenumber is independent of the Weber number, in line with expectations from the three-phase R-T model cf. Eq. 6.1. Additional simulations (not shown) indicate a similarly weak dependence of the dominant wavenumber on the noise amplitude α for values between 1 % and 7 %, as expected (larger noise amplitude values led to jetting incompatible with experimental observations). The results also show that amplitude damping of perturbation modes occurs early, at $t/\tau_\mathrm{i} < 1$, preceding the predicted end of phase 2 according to the R-T model (marked by the vertical white dashed lines at $t/\tau_\mathrm{i} = 1$ in Fig. 6.1). This suggests that inertial growth is insufficient to overcome surface tension effects, causing the perturbations to flatten out during phase 2. Moreover, comparing $\mathrm{We}^\mathrm{sim} = 1000$ and 2500 shows that the effective end of phase 2 varies with Weber number: the higher Weber number case exhibits a slightly longer inertial growth period. This is reflected in the extended presence of high-wavenumber content (yellow regions) approaching the white dashed line, which we attribute to the reduced influence of surface tension at higher Weber numbers. Note that we do not observe sheet penetration by the perturbations. This is consistent with predictions of the R-T model as $t_s/t_c \sim 1.3 \times 10^{-3} \cdot \mathrm{We}^{-1}$ (see [26]), which estimates sheet breakup at much later times: $t/\tau_\mathrm{i} = t/\tau_\mathrm{c} \cdot \sqrt{\mathrm{We}} \approx 24$ and $t/\tau_\mathrm{i} \approx 15$ for $\mathrm{We} = 1000$ and $\mathrm{We} = 2500$, respectively, assuming a typical droplet radius of $R_0 = 15.5\,\mu\mathrm{m}$ [107]. In summary, we find good agreement between preliminary simulation results and aspects of the theoretical predictions.

Next, we compare with experimental results. In the previous Chapter [107], we experimentally identified a non-dimensional wavenumber of $\hat{k} = \frac{2\pi}{\lambda}R_0 = 6.5$, measured at a later time ($t/\tau_\mathrm{c} \approx 0.38$) than those considered in the present simulations ($t/\tau_\mathrm{i} = 5$), for a We number that translates to $\mathrm{We}^\mathrm{sim} = 400$. Since this value was extracted well into phase 3 of the R-T model, the corresponding wavelength was likely stretched, and therefore, the wavenumber is expected to be higher during the simulated time range. To facilitate comparison, we assume a temporal stretching behavior $\sim 1/t$, and use this to extrapolate the experimental wavenumber backward to the simulation time range (see the yellow dashed line in Fig. 6.1). However, we note that in previous work we observed that stretching depends on the local sheet coordinate, and thus this approach constitutes a strong simplification. As reported in the prior Chapters, the experiments yield a dominant wavenumber that is significantly larger than the predictions from theory and simulation.

Future work.—To further refine our understanding of the origin and evolution of perturbation modes, future work may incorporate more BASILISK C simulations and could explore alternative models beyond the classical R-T framework. Simulations should be extended to cover a broader range of (larger) Weber numbers and time ranges, with improved mesh resolution and noise amplitude profiles that reflect the actual pressure distribution rather than assuming a constant (white noise) amplitude. Fully three-dimensional simulations will be essential to capture azimuthal modulation modes. In addition, incorporating asymmetric laser irradiation profiles into experiments may reveal new instability regimes. The preliminary simulations shed new light on the topic; yet, despite an extensive analysis of experimental data, the fundamental question remains open: Are the strikingly concentric ripples *solely* a manifestation of a Rayleigh–Taylor-type instability? This consideration is also relevant for the vaporization of sheets and the formation of plasma on sheets, as both processes are sensitive to the *local* sheet thickness. As a result, variations in surface modulation may translate into plasma formation instabilities.

Shadowgraphy Gallery

In the following, I present several illustrative figures containing shadowgraphs from the various categories relevant to the research questions driving this thesis: surface modulations, plasma formation, early-time prepulse dynamics, and low-Weber-number oscillations. Although not included in the core of my thesis, these examples offer valuable insight. Each figure description consists of two parts: the first provides an objective account of the observation, while the second part, indicated by ➢, offers a brief interpretation.

Surface modulations

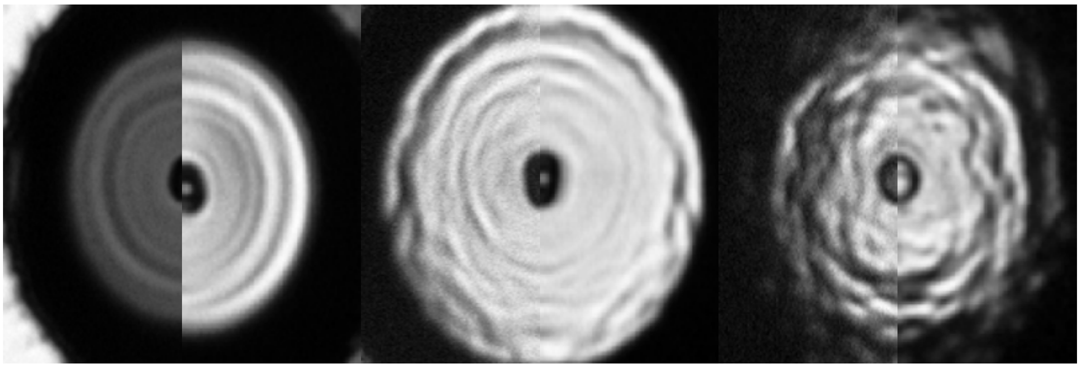

FIGURE 6.2: Three front (left) and back (right) views of liquid tin sheets for increasing Weber numbers (left to right). ➢ This suggests that the front and back side show an identical modulation pattern throughout the phase transition from concentric to azimuthal.

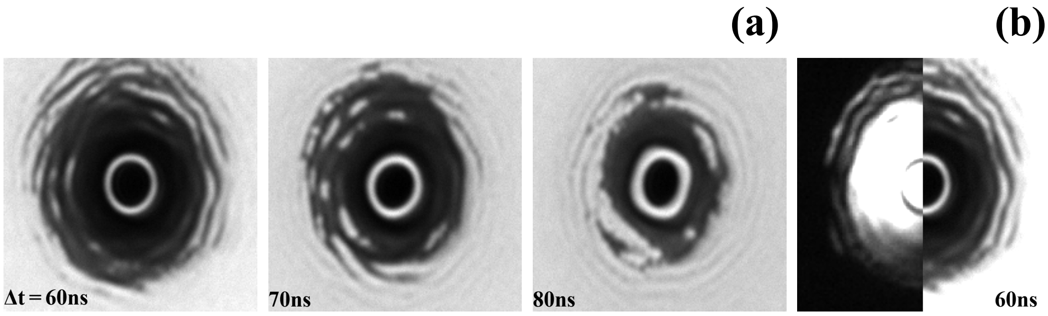

FIGURE 6.3: Zoomed-in shadowgraphy frames following the partial vaporization of a liquid tin sheet. Δt indicates the time after the start of the 50 ns vaporization pulse. ➢ (a) Coalescence between freely flying thickness modulations is observed. (b) Comparison between the back side (left) and the front side (right) highlights that non-vaporized tin continues to reflect shadowgraphy light.

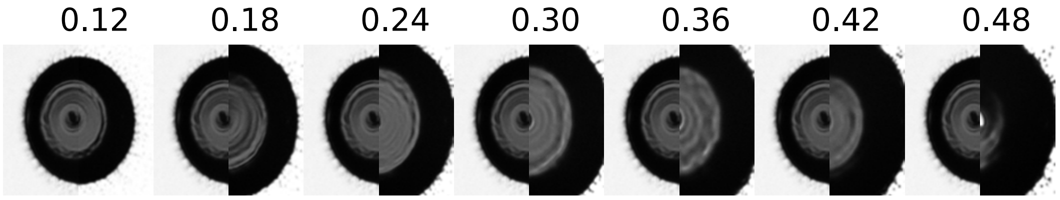

FIGURE 6.4: Front view of the liquid tin sheet, where the left side of each frame corresponds to $t/\tau_c = 0.12$, and the right side shows a later timestep as indicated by the value on top of the frames. ➢ The sequence highlights the temporal evolution of the observed ripples, including azimuthal modulations, widening, and radial stretching. Furthermore, it suggests that inner concentric ripples gradually acquire azimuthal features over time.

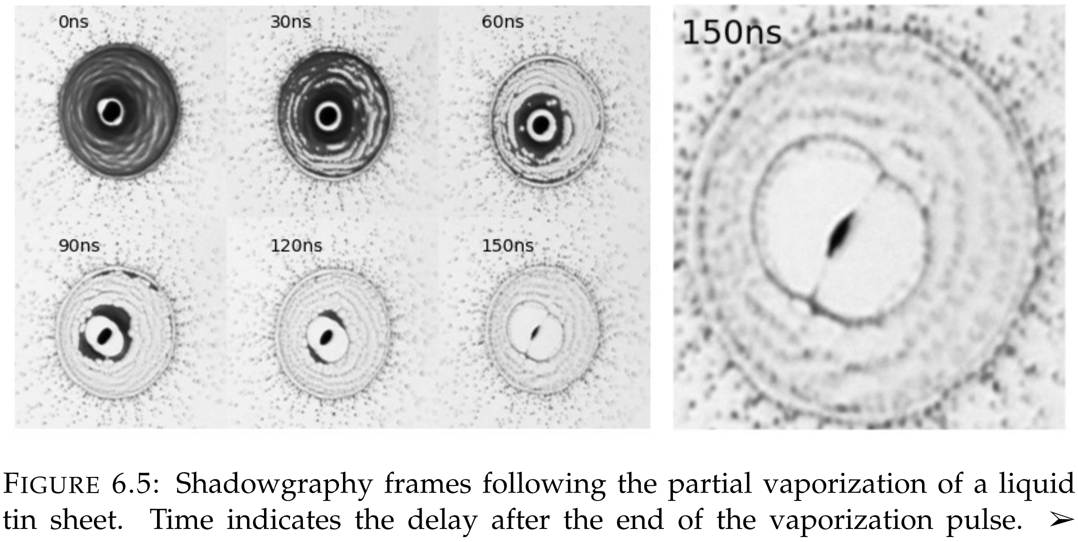

FIGURE 6.5: Shadowgraphy frames following the partial vaporization of a liquid tin sheet. Time indicates the delay after the end of the vaporization pulse. ➢ The sequence highlights several physical phenomena, such as the coalescence of freely flying thickness modulations and the onset of breakup, likely driven by a Rayleigh–Plateau instability. Figure developed with Mikheil Kharbedia (ARCNL).

Plasma formation

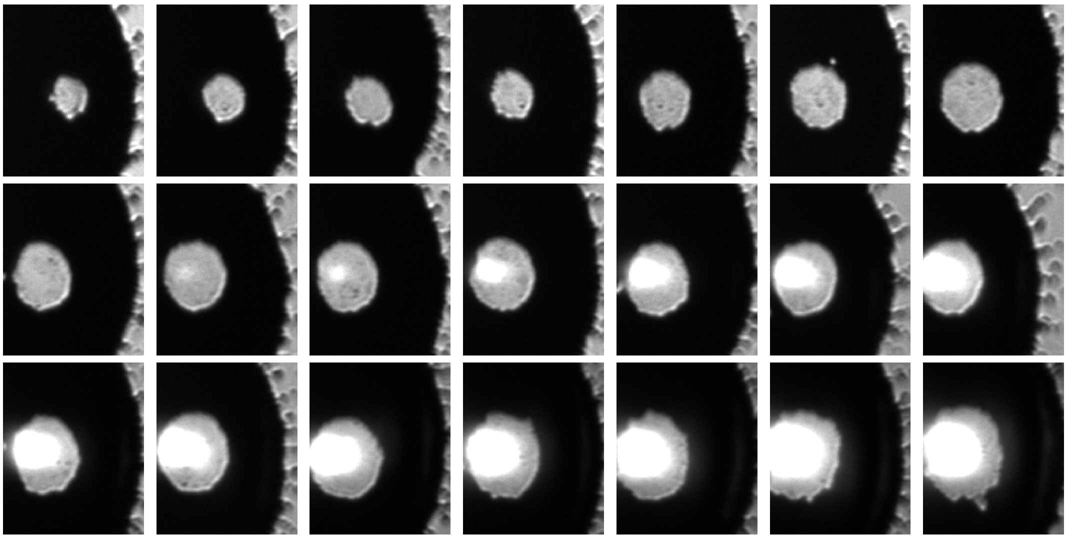

FIGURE 6.6: Plasma threshold measurement using a small imaged VP spot on a sheet to probe a region of uniform thickness. The VP laser fluence increases from left to right and top to bottom. ➢ At low fluences, vaporization occurs; at higher fluences, plasma formation (i.e., a light-emitting region) is observed. The size of the vaporized or plasma spot increases with VP fluence, indicating that the VP beam's intensity profile is nonuniform. This also highlights the distinct thickness and intensity requirements for the sheet to (i) remain intact, (ii) undergo evaporation according to the Hertz-Knudsen [67], or (iii) enable plasma formation (see Chapter 3).

Early-time prepulse dynamics

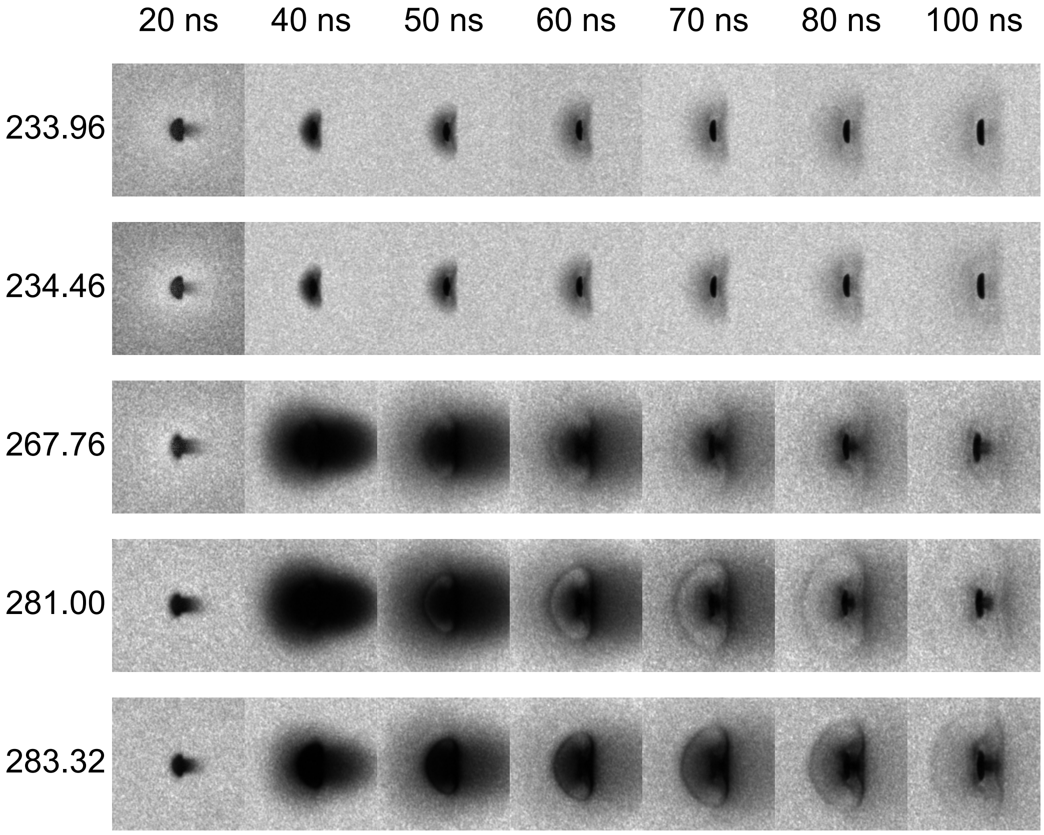

FIGURE 6.7: Early-time shadowgraphs captured using laser light obtained from an optical parametric oscillator (OPO) as the imaging laser (instead of green light at 560 nm, as used previously) are shown for different air wavelengths (rows) and various delays (columns) after the prepulse (PP) impact on the droplet. ➢ Observations at different wavelengths reveal varying absorption levels, which highlight rapid vapor expansion during and after PP irradiation of the droplet (on the order of km s^{-1}). As the vapor rarefies, slower-propagating density waves become visible around 60 ns.

Low-Weber-number oscillations

Further details will be presented in an upcoming publication by M. Kharbedia et al. (see List of Publications).

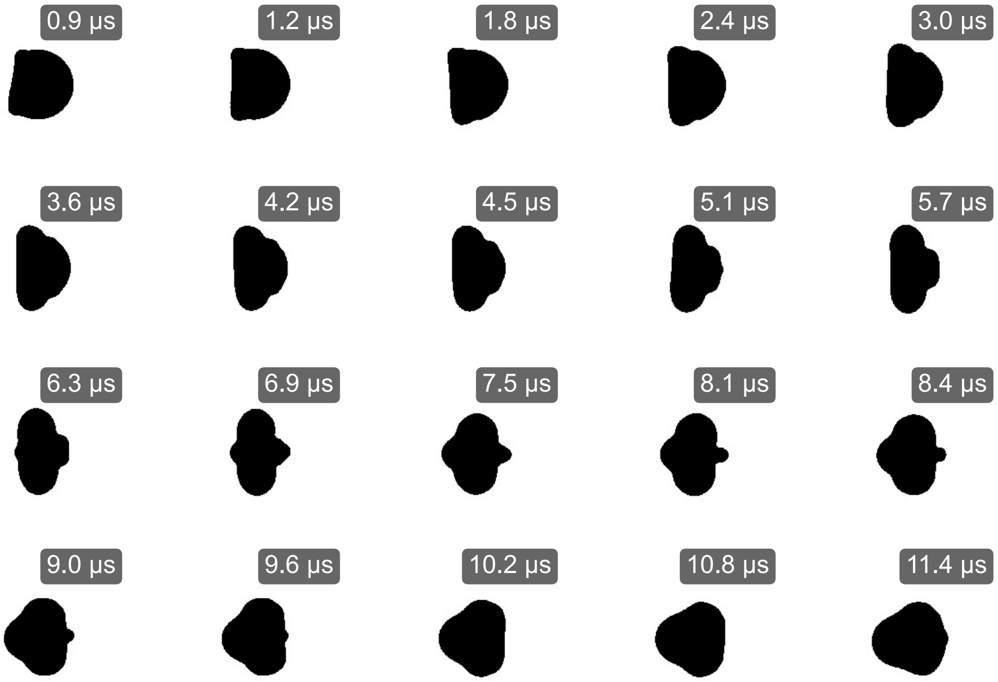

FIGURE 6.8: A 50 µm-diameter droplet that is irradiated by a 6 ns prepulse with 0.4 mJ energy. ➢ As result, capillary waves are observed traveling from left to right in response, colliding on the right side.

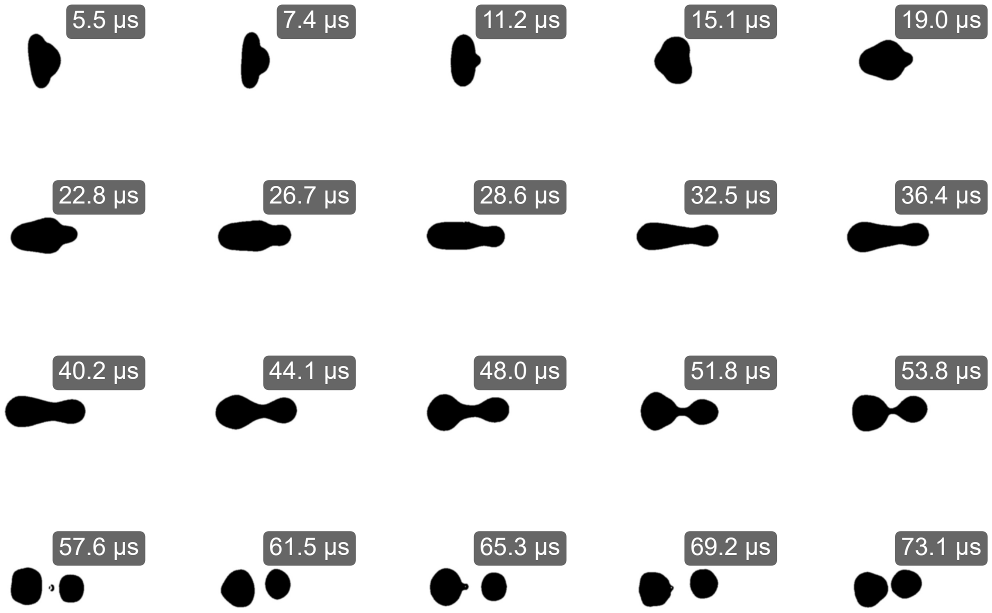

FIGURE 6.9: A 70 µm-diameter droplet irradiated by a 6 ns prepulse with 0.6 mJ energy. ➢ As a result, capillary waves, colliding on the right side, lead to droplet *splitting*.

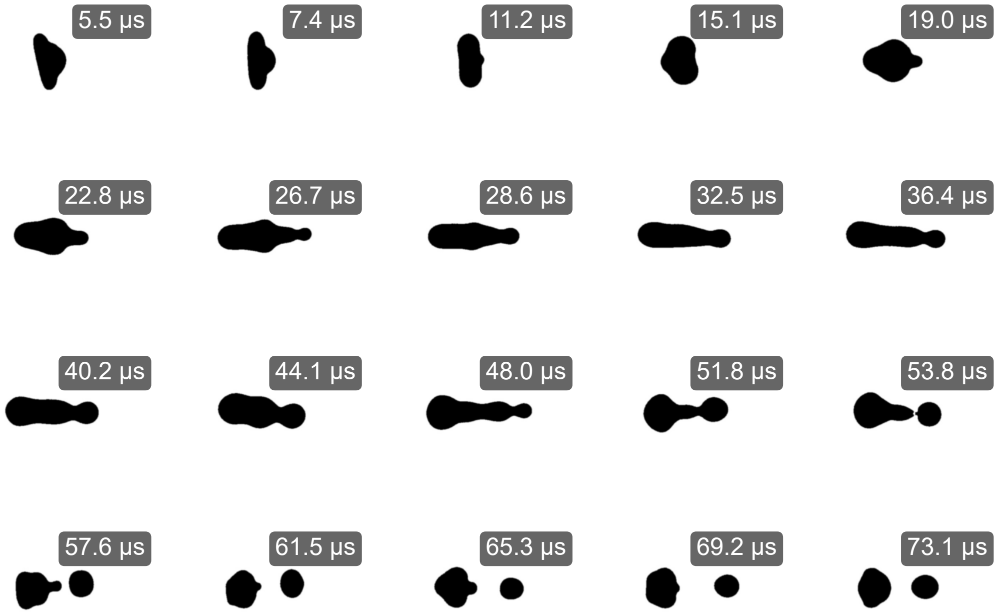

FIGURE 6.10: A 70 µm-diameter droplet irradiated by a 6 ns prepulse with 0.7 mJ energy. ➢ As a result, capillary waves, colliding on the right side, lead to droplet *dripping*.

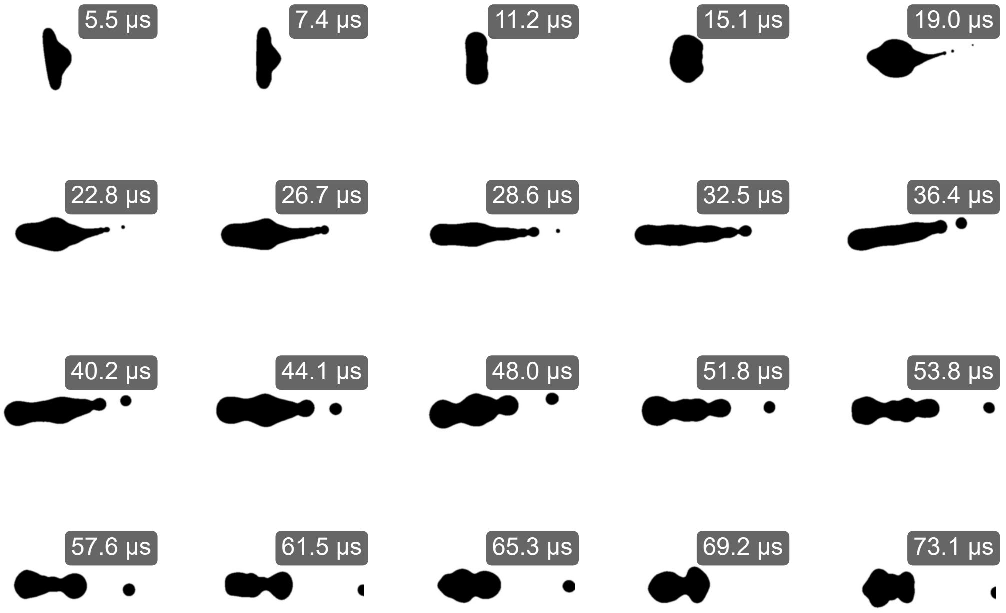

FIGURE 6.11: A 70 µm-diameter droplet irradiated by a 6 ns prepulse with 1.1 mJ energy. ➢ As a result, capillary waves, colliding on the right side, lead to droplet *jetting* (see C. Clanet and J. Lasheras, *Transition from Dripping to Jetting*, J. Fluid Mech. **383**, 307–326 (1999).

List of Publications

The following work resulted directly from the doctoral research of H. K. Schubert:

CHAPTER 2
H. K. Schubert, D. J. Engels, R. A. Meijer, B. Liu, and O.O. Versolato, *Scaling relations in laser-induced vaporization of thin free-flying liquid metal sheets*, Phys. Rev. Res. **6**, 023182 (2024).

CHAPTER 3
H. K. Schubert, R. A. Meijer, B. Liu, D. J. Engels, O. O. Versolato, *Laser-Induced Plasma Formation on free-flying Liquid Tin Sheets*, Submitted.

CHAPTER 4
H. K. Schubert, D. J. Engels R. A. Meijer, B. Liu, O. O. Versolato, *Observation of discrete concentric surface modulations on free-flying liquid tin sheets*, Phys. Fluids **37**, 094108 (2025).

H. K. Schubert contributed to the preparation of measurement campaigns, performed measurements, and participated in technical discussions during weekly setup meetings for the following work:

D. J. Engels, R. A. Meijer, **H.K. Schubert**, W. van der Zande, W. Ubachs, and O. O. Versolato, *High-Resolution Spectroscopic Imaging of Atoms and Nanoparticles in Thin Film Vaporization*, Appl. Phys. Lett. **123**, 254102 (2023).

D. J. Engels, **H. K. Schubert**, M. Kharbedia, W. Ubachs, and O. O. Versolato, *Spectroscopic Imaging of Tin Vapor Near Plasma Threshold*, Phys. Rev. Res. **7**, 023307 (2025).

H. L. França, **H. K. Schubert**, O. O. Versolato, and M. Jalaal, *Laser-induced droplet deformation: curvature inversion explained from instantaneous pressure impulse*, J. Fluid Mech. **1020**, A21 (2025).

M. Kharbedia, B. Liu, R. Meijer, D. J. Engels, **H. K. Schubert**, L. Bourouiba, and O. O. Versolato, *Rim destabilization and re-formation upon severance from its expanding sheet*, Submitted.

M. Kharbedia, H. L. França, **H. K. Schubert**, D. J. Engels, M. Jalaal and O. O. Versolato, *Laser-driven droplet deformation at low Weber numbers*, Submitted.

M. Kharbedia, H. L. França, **H. K. Schubert**, D. J. Engels, M. Jalaal and O. O. Versolato, *Droplet breakup and jetting upon laser impact*, In preparation for publication.

Furthermore, H. K. Schubert contributed to **five** invention disclosure files (IDFs), of which **two** resulted in granted patents. The outcome of an IDF may be (i) a patent, (ii) a publication, (iii) an archive, or (iv) confidentiality (“keep secret”). Importantly, the chosen outcome reflects a business decision rather than an assessment of the invention’s quality.

Bibliography

[1]R. Kurzweil, “The law of accelerating returns”, in *Alan turing: life and legacy of a great thinker*, edited by C. Teuscher (Springer Berlin Heidelberg, Berlin, Heidelberg, 2004), pp. 381–416.

[2]B. Wood and E. K. Boyle, *The human genus*, Annual Review of Anthropology **45**, 151–164 (2016).

[3]J.-J. Hublin, A. Ben-Ncer, S. E. Bailey, and et al., *New fossils from jebel irhoud, morocco and the pan-african origin of homo sapiens*, Nature **546**, 289–292 (2017).

[4]Y. N. Harari, *Sapiens: a brief history of humankind* (Harper, 2014).

[5]S. Mcbrearty and A. S. Brooks, *The revolution that wasn't: a new interpretation of the origin of modern human behavior*, J. Hum. Evol. **39**, 453–563 (2000).

[6]C. Henshilwood and C. Marean, *The origin of modern human behavior*, Current anthropology **44**, 627–651 (2004).

[7]G. E. Moore, *Lithography and the future of Moore's law*, Proc. SPIE **2439**, 2439 - 2439 –16 (1995).

[8]J. van Schoot, K. Troost, F. Bornebroek, R. van Ballegoij, S. Lok, P. Krabbendam, J. Stoeldraijer, J. Benschop, J. Finders, H. Meiling, E. van Setten, B. Kneer, P. Kuerz, W. Kaiser, T. Heil, and S. Migura, *The future of EUV lithography: continuing Moore's Law into the next decade*, Proc. SPIE **10583**, `10.1117/12.2295800` (2018).

[9]E. Harma, R. Rathi, J. Misharwal, B. Sinhmar, S. Kumari, J. Dalal, and A. Kumar, *Evolution in lithography techniques: microlithography to nanolithography*, Nanomaterials (Basel) **12**, 2754 (2022).

[10]J. VerWey, *Tracing the emergence of extreme ultraviolet lithography*, Technical report (CSET, Georgetown University, July 2024).

[11]T. Sterling, *Asml's next chip challenge: rollout of its new $350 mln 'high na euv' machine*, Reuters (2024).

[12]Insemi Technologies, *Moore's law and beyond: the future of semiconductor scaling*, Accessed: 2025-04-28, (2023) `https://insemitech.com/blogs/moores-law-and-beyond-the-future-of-semiconductor-scaling/`.

[13]Y.-W. Kim, S. Mishra, S. Jin, R. Panda, H. Kuehne, L. Karlinsky, V. Saligrama, K. Saenko, A. Oliva, and R. Feris, *How transferable are video representations based on synthetic data?*, in Thirty-sixth conference on neural information processing systems datasets and benchmarks track (2022).

[14]I. Hidalgo, F. Fernández-de-Vega, J. Ceberio, et al., *Sustainable artificial intelligence systems: an energy efficiency approach*, TechRxiv, `10.36227/techrxiv.24610899.v1` (2023).

[15]C. A. Mack, *Fifty years of moore's law*, IEEE Transactions on Semiconductor Manufacturing **24**, 202–207 (2011).

[16]N. d. Tyson and A. Lang, *Accessory to war: the unspoken alliance between astrophysics and the military* (W. W. Norton and Company, 2018).

[17]I. Fomenkov, D. Brandt, A. Ershov, A. Schafgans, Y. Tao, G. Vaschenko, S. Rokitski, M. Kats, M. Vargas, M. Purvis, R. Rafac, B. La Fontaine, S. De Dea, A. LaForge, J. Stewart, S. Chang, M. Graham, D. Riggs, T. Taylor, M. Abraham, and D. Brown, *Light sources for high-volume manufacturing EUV lithography: technology, performance, and power scaling*, Adv. Opt. Technol. **6**, 173–186 (2017).

[18]H. Mizoguchi, H. Nakarai, T. Abe, K. M. Nowak, Y. Kawasuji, H. Tanaka, Y. Watanabe, T. Hori, T. Kodama, Y. Shiraishi, T. Yanagida, G. Soumagne, T. Yamada, T. Yamazaki, S. Okazaki, and T. Saitou, *Performance of 100-W HVM LPP-EUV source*, Adv. Opt. Technol. **4**, 297–309 (2015).

[19]O. O. Versolato, *Physics of laser-driven tin plasma sources of EUV radiation for nanolithography*, Plasma Sources Sci. Technol. **28**, 083001 (2019).

[20]J. Hernandez-Rueda, B. Liu, D. J. Hemminga, Y. Mostafa, R. A. Meijer, D. Kurilovich, M. Basko, H. Gelderblom, J. Sheil, and O. O. Versolato, *Early-time hydrodynamic response of a tin droplet driven by laser-produced plasma*, Phys. Rev. Res. **4**, 013142 (2022).

[21]B. Liu, R. A. Meijer, W. Li, J. Hernandez-Rueda, H. Gelderblom, and O. O. Versolato, *Mass partitioning in fragmenting tin sheets*, Phys. Rev. Appl. **20**, 014048 (2023).

[22]D. Kurilovich, A. L. Klein, F. Torretti, A. Lassise, R. Hoekstra, W. Ubachs, H. Gelderblom, and O. O. Versolato, *Plasma propulsion of a metallic microdroplet and its deformation upon laser impact*, Phys. Rev. Appl. **6**, 014018 (2016).

[23]H. Gelderblom, H. Lhuissier, A. L. Klein, W. Bouwhuis, D. Lohse, E. Villermaux, and J. H. Snoeijer, *Drop deformation by laser-pulse impact*, J. Fluid Mech. **794**, 676–699 (2016).

[24]B. Liu, R. A. Meijer, J. Hernandez-Rueda, D. Kurilovich, Z. Mazzotta, S. Witte, and O. O. Versolato, *Laser-induced vaporization of a stretching sheet of liquid tin*, J. Appl. Phys. **129**, 053302 (2021).

[25]B. Liu, D. Kurilovich, H. Gelderblom, and O. O. Versolato, *Mass loss from a stretching semitransparent sheet of liquid tin*, Phys. Rev. Appl. **13**, 024035 (2020).

[26]A. L. Klein, D. Kurilovich, H. Lhuissier, O. O. Versolato, D. Lohse, E. Villermaux, and H. Gelderblom, *Drop fragmentation by laser-pulse impact*, J. Fluid Mech. **893**, A7 (2020).

[27]J. R. Freeman, S. S. Harilal, and A. Hassanein, *Enhancements of extreme ultraviolet emission using prepulsed Sn laser-produced plasmas for advanced lithography applications*, J. Appl. Phys. **110**, 083303 (2011).

[28]T. Cummins, C. O'Gorman, P. Dunne, E. Sokell, G. O'Sullivan, and P. Hayden, *Colliding laser-produced plasmas as targets for laser-generated extreme ultraviolet sources*, Appl. Phys. Lett. **105**, 044101 (2014).

[29]D. Hudgins, N. Gambino, B. Rollinger, and R. Abhari, *Neutral cluster debris dynamics in droplet-based laser-produced plasma sources*, J. Phys. D **49**, 185205 (2016).

[30] A. L. Klein, W. Bouwhuis, C. W. Visser, H. Lhuissier, C. Sun, J. H. Snoeijer, E. Villermaux, D. Lohse, and H. Gelderblom, *Drop shaping by laser-pulse impact*, Phys. Rev. Appl. **3**, 044018 (2015).

[31] D. Kurilovich, M. M. Basko, D. A. Kim, F. Torretti, R. Schupp, J. C. Visschers, J. Scheers, R. Hoekstra, W. Ubachs, and O. O. Versolato, *Power-law scaling of plasma pressure on laser-ablated tin microdroplets*, Phys. Plasmas **25**, 012709 (2018).

[32] K. Tomita, Y. Pan, A. Sunahara, K. Kouge, H. Mizoguchi, and K. Nishihara, *Observation of plasma inflows in laser-produced Sn plasma and their contribution to extreme-ultraviolet light output enhancement*, Sci. rep. **13**, 1825 (2023).

[33] D. J. Engels, R. A. Meijer, H. K. Schubert, W. J. van der Zande, W. Ubachs, and O. O. Versolato, *High-resolution spectroscopic imaging of atoms and nanoparticles in thin film vaporization*, Appl. Phys. Lett. **123**, 254102 (2023).

[34] A. Miotello and R. Kelly, *Critical assessment of thermal models for laser sputtering at high fluences*, Appl. Phys. Lett. **67**, 3535–3537 (1995).

[35] R. Kelly and A. Miotello, *Comments on explosive mechanisms of laser sputtering*, Appl. Surf. Sci. **96-98**, 205–215 (1996).

[36] A. Miotello and R. Kelly, *Laser-induced phase explosion: new physical problems when a condensed phase approaches the thermodynamic critical temperature:* Appl. Phys. A **69**, S67–S73 (1999).

[37] A. H. A. Lutey, *An improved model for nanosecond pulsed laser ablation of metals*, J. Appl. Phys. **114**, 083108 (2013).

[38] D. Kurilovich, "Laser-induced dynamics of liquid tin microdroplets", PhD thesis (Vrije Universiteit Amsterdam, 2019).

[39] E. Villermaux and B. Bossa, *Drop fragmentation on impact*, J. Fluid Mech. **668**, 412–435 (2011).

[40] Y. Wang and L. Bourouiba, *Non-galilean taylor–culick law governs sheet dynamics in unsteady fragmentation*, J. Fluid Mech. **969**, A19 (2023).

[41] R. A. Meijer, A. S. Stodolna, K. S. E. Eikema, and S. Witte, *High-energy Nd:YAG laser system with arbitrary sub-nanosecond pulse shaping capability*, Opt. Lett. **42**, 2758 (2017).

[42] G. Cisneros, J. S. Helman, and C. N. J. Wagner, *Dielectric function of liquid tin between 250 and 1100°C*, Phys. Rev. B Condens. Matter **25**, 4248–4251 (1982).

[43] C. Vernay, L. Ramos, and C. Ligoure, *Free radially expanding liquid sheet in air: time- and space-resolved measurement of the thickness field*, J. Fluid Mech. **764**, 428–444 (2015).

[44] S. J. Byrnes, *Multilayer optical calculations*, arXiv (2016).

[45] J. A. Stratton, *Electromagnetic Theory*, 2nd (McGraw-Hill Book Company, Inc., London and New York, 1941).

[46] J. Safarian and T. A. Engh, *Vacuum evaporation of pure metals*, Mettalurg. Mater. Trans. A **44**, 747–753 (2013).

[47] D. R. Stull, *Vapor Pressure of Pure Substances. Organic and Inorganic Compounds*, Ind. Eng. Chem. **39**, 517–540 (1947).

[48] N. I. of Standards and Technology, NIST Chemistry WebBook (SRD 69), [Online]. Available: `https://webbook.nist.gov/` [2023, November 08]. National Institute of Standards and Technology, Gaithersburg, MD. 2023.

[49] I. V. Savchenko, S. V. Stankus, and A. S. Agadjanov, *Measurement of liquid tin heat transfer coefficients within the temperature range of 506–1170 K*, High Temp. **49**, 506–511 (2011).

[50] D. J. Hemminga, L. Poirier, M. M. Basko, R. Hoekstra, W. Ubachs, O. O. Versolato, and J. Sheil, *High-energy ions from Nd:YAG laser ablation of tin microdroplets: comparison between experiment and a single-fluid hydrodynamic model*, Plasma Sources Sci. and Technol. **30**, 105006 (2021).

[51] L. Poirier, D. J. Hemminga, A. Lassise, L. Assink, R. Hoekstra, J. Sheil, and O. O. Versolato, *Strongly anisotropic ion emission in the expansion of Nd:YAG-laser-produced plasma*, Phys. Plasmas **29**, 123102 (2022).

[52] M. Haddadi. M, B. Das, J. Jeong, S. Kim, and D.-S. Kim, *Near-maximum microwave absorption in a thin metal film at the pseudo-free-standing limit*, Sci. Rep. **12**, 18386 (2022).

[53] Y. Wang and L. Bourouiba, *Drop impact on small surfaces: thickness and velocity profiles of the expanding sheet in the air*, J. Fluid Mech. **814**, 510–534 (2017).

[54] M. M. Stevanović, *Thermodynamic characterization of vaporization of the fourth group elements*, Int. J. Thermophys. **4**, 353–362 (1983).

[55] M. J. Assael, A. Chatzimichailidis, K. D. Antoniadis, W. A. Wakeham, M. L. Huber, and H. Fukuyama, *Reference correlations for the thermal conductivity of liquid copper, gallium, indium, iron, lead, nickel and tin*, High Temp. High Press. **46**, 391–416 (2017).

[56] M. Assael, A. Kalyva, K. Antoniadis, R. Banish, I. Egry, J. Wu, E. Kaschnitz, and W. Wakeham, *Reference Data for the Density and Viscosity of Liquid Copper and Liquid Tin*, J. Phys. Chem. Ref. Data **39**, 331051–331058 (2010).

[57] H. Heffan, *Heat capacity of liquid tin*, 8 (University of California, Berkeley, 1958).

[58] A. V. Khvan, T. Babkina, A. T. Dinsdale, I. A. Uspenskaya, I. V. Fartushna, A. I. Druzhinina, A. B. Syzdykova, M. P. Belov, and I. A. Abrikosov, *Thermodynamic properties of tin: Part I Experimental investigation, ab-initio modelling of α-, β-phase and a thermodynamic description for pure metal in solid and liquid state from 0 K*, Calphad **65**, 50–72 (2019).

[59] H.-U. Krebs, M. Weisheit, J. Faupel, E. Suske, T. Scharf, C. Fuhse, M. Störmer, K. Sturm, M. Seibt, H. Kijewski, E. Panchenko, and M. Buback, *Pulsed laser deposition (pld) - a versatile thin film technique*, Adv. Solid State Phys **43**, 101–107 (2003).

[60] S. M. Rossnagel, *Thin film deposition with physical vapor deposition and related technologies*, J. Vac. Sci. Technol. A **21**, S74–S87 (2003).

[61] D. W. Hahn. and N. Omenetto, *Laser-induced breakdown spectroscopy (LIBS), part ii: review of instrumental and methodological approaches to material analysis and applications to different fields*, Appl. Spectrosc. **66**, 347–419 (2012).

[62] L. Yongchao, F. Yao, Z. Yao, S. Yaochun, and S. Yaochun, *Emission enhancement in fs + ns dual-pulse libs of cu*, Photonics **10**, 783 (2023).

[63] S. P. M., *Artificial intelligence-driven innovations in laser processing of metallic materials*, Metals **14**, 1458 (2024).

[64] I. Fomenkov, A. Schafgans, and D. Brandt, *Laser-produced plasma sources for high-volume-manufacturing euv lithography*, Synchrotron Radiat. News **32**, 3–8 (2019).

[65] O. O. Versolato, *Physics of laser-driven tin plasma sources of EUV radiation for nanolithography*, Plasma Sources Sci. Technol. **28**, 083001 (2019).

[66] D. J. Engels, R. A. Meijer, H. K. Schubert, W. J. van der Zande, W. Ubachs, and O. O. Versolato, *High-resolution spectroscopic imaging of atoms and nanoparticles in thin film vaporization*, Appl. Phys. Lett. **123**, 254102 (2023).

[67] H. K. Schubert, D. J. Engels, R. A. Meijer, B. Liu, and O. O. Versolato, *Scaling relations in laser-induced vaporization of thin free-flying liquid metal sheets*, Phys. Rev. Res. **6**, 023182: 1–12 (2024).

[68] D. J. Engels, H. K. Schubert, M. Kharbedia, W. Ubachs, and O. O. Versolato, *Spectroscopic imaging of tin vapor near plasma threshold*, Phys. Rev. Res. **7**, 023307 (2025).

[69] R. A. Meijer, D. Kurilovich, B. Liu, Z. Mazzotta, J. Hernandez-Rueda, O. O. Versolato, and S. Witte, *Nanosecond laser ablation threshold of liquid tin microdroplets*, Appl. Phys. A **128**, 570 (2022).

[70] H. Gelderblom, H. Lhuissier, A. Klein, W. Bouwhuis, D. Lohse, E. Villermaux, and J. Snoeijer, *Drop deformation by laser-pulse impact*, J. Fluid Mech. **794**, 676–699 (2016).

[71] R. A. Meijer, R. Schupp, J. Sheil, M. M. Basko, K. S. E. Eikema, O. O. Versolato, and S. Witte, *Spall-velocity reduction in double-pulse impact on tin microdroplets*, Phys. Rev. Appl. **16**, 024026 (2021).

[72] B. Liu, R. A. Meijer, W. Li, J. Hernandez-Rueda, H. Gelderblom, and O. O. Versolato, *Mass partitioning in fragmenting tin sheets*, Phys. Rev. Appl. **20**, 014048 (2023).

[73] J. Gonzalez, D. J. Engels, D. J. Hemminga, O. O. Versolato, and J. Sheil, "Formation of a strongly radiative plasma from a Sn vapour due to the presence of nanoparticles", under review.

[74] C. V. Bindhu, S. S. Harilal, M. S. Tillack, F. Najmabadi, and A. C. Gaeris, *Energy absorption and propagation in laser-created sparks*, Appl. Spectrosc. **58**, 719–726 (2004).

[75] V. Bergeron, D. Bonn, J. Y. Martin, and L. Vovelle, *Controlling droplet deposition with polymer additives*, Nature **405**, 772–775 (2000).

[76] C. Josserand and S. Thoroddsen, *Drop impact on a solid surface*, Annu. Rev. Fluid Mech. **48**, 365–391 (2016).

[77] B. L. Scheller and D. W. Bousfield, *Newtonian drop impact with a solid surface*, AIChE J. **41**, 1357–1367 (1995).

[78] Y. Wang and L. Bourouiba, *Drop impact on small surfaces: thickness and velocity profiles of the expanding sheet in the air*, J. Fluid Mech. **814**, 510–534 (2017).

[79] E. Villermaux and B. Bossa, *Drop fragmentation on impact*, J. Fluid Mech. **668**, 412–435 (2011).

[80] A. Rozhkov, B. Prunet-Foch, and M. Vignes-Adler, *Impact of water drops on small targets*, Phys. Fluids **14**, 3485–3501 (2002).

[81] X. Huang, X. Dong, J. Li, and J. Liu, *Droplet impact induced large deflection of a cantilever*, Phys. Fluids **31**, 062106 (2019).

[82] Y. Wang, R. Dandekar, N. Bustos, S. Poulain, and L. Bourouiba, *Universal rim thickness in unsteady sheet fragmentation*, Phys. Rev. Lett. **120**, 204503 (2018).

[83] S. Kooij, R. Sijs, M. M. Denn, E. Villermaux, and D. Bonn, *What determines the drop size in sprays?*, Phys. Rev. X **8**, 031019 (2018).

[84] D. Lohse, *Fundamental fluid dynamics challenges in inkjet printing*, Annu. Rev. Fluid Mech. **54**, 349–382 (2022).

[85] B. Derby, *Inkjet printing of functional and structural materials: fluid property requirements, feature stability, and resolution*, Annu. Rev. Mater. Res. **40**, 395–414 (2010).

[86] V. Bakshi, ed., *EUV lithography*, 2nd (SPIE Press, Mar. 30, 2018), p. 758.

[87] H. Gelderblom, H. Lhuissier, A. Klein, W. Bouwhuis, D. Lohse, E. Villermaux, and J. Snoeijer, *Drop deformation by laser-pulse impact*, J. Fluid Mech. **794**, 676–699 (2016).

[88] H. Mizoguchi, T. Abe, Y. Watanabe, T. Ishihara, T. Ohta, T. Hori, A. Kurosu, H. Komori, K. Kakizaki, A. Sumitani, O. Wakabayashi, and H. Nakarai, *First generation laser-produced plasma source system for hvm euv lithography*, Proc. SPIE **7636**, 763608 (2010).

[89] I. Fomenkov, D. Brandt, A. Ershov, A. Schafgans, Y. Tao, G. Vaschenko, S. Rokitski, M. Kats, M. Vargas, M. Purvis, R. Rafac, B. La Fontaine, S. De Dea, A. LaForge, J. Stewart, S. Chang, M. Graham, D. Riggs, T. Taylor, M. Abraham, and D. Brown, *Light sources for high-volume manufacturing EUV lithography: technology, performance, and power scaling*, Adv. Opt. Technol. **6**, 173–186 (2017).

[90] T. Sizyuk and A. Hassanein, *Tuning laser wavelength and pulse duration to improve the conversion efficiency and performance of EUV sources for nanolithography*, Phys. Plasmas **27**, 103507 (2020).

[91] H. B. Squire, *Investigation of the instability of a moving liquid film*, Br. J. Appl. Phys. **4**, 167 (1953).

[92] G. Taylor, *Formation of thin flat sheets of water*, Proc. R. Soc. Lond. A **259**, 1–17 (1961).

[93] E. Villermaux and C. Clanet, *Life of a flapping liquid sheet*, J. Fluid Mech. **462**, 341–363 (2002).

[94] C. Clanet and E. Villermaux, *Life of a smooth liquid sheet*, J. Fluid Mech. **462**, 307–340 (2002).

[95] R. Li and N. Ashgriz, *Characteristics of liquid sheets formed by two impinging jets*, Phy. Fluids **18**, 087104 (2006).

[96] N. Bremond and E. Villermaux, *Bursting thin liquid films*, J. Fluid Mech. **524**, 121–130 (2005).

[97] F. P. Buff, R. A. Lovett, and F. H. Stillinger, *Interfacial density profile for fluids in the critical region*, Phys. Rev. Lett. **15**, 621–623 (1965).

[98] O. Krichevsky and J. Stavans, *Surfactant-polymer interactions in freely suspended lyotropic films*, Phys. Rev. Lett. **73**, 696–699 (1994).

[99] A. Vledouts, J. Quinard, N. Vandenberghe, and E. Villermaux, *Explosive fragmentation of liquid shells*, J. Fluid Mech. **788**, 246–273 (2016).

[100]I. P.-O. Company, *Model k2 distamax oem handbook*, Retrieved from `https://www.infinity-usa.com/wp-content/uploads/Model-K2-DistaMax-OEM-Handbook-090121.pdf` (2021).

[101]B. Liu, J. Hernandez-Rueda, H. Gelderblom, and O. O. Versolato, *Speed of fragments ejected by an expanding liquid tin sheet*, Phys. Rev. Fluids **7**, 083601 (2022).

[102]J. Hernandez-Rueda, B. Liu, D. J. Hemminga, Y. Mostafa, R. A. Meijer, D. Kurilovich, M. Basko, H. Gelderblom, J. Sheil, and O. O. Versolato, *Early-time hydrodynamic response of a tin droplet driven by laser-produced plasma*, Phys. Rev. Res. **4**, 013142 (2022).

[103]H. Xia, M. Shats, and H. Punzmann, *Modulation instability and capillary wave turbulence*, Europhys. Lett. **91**, 14002 (2010).

[104]G. Cisneros, J. S. Helman, and C. N. J. Wagner, *Dielectric function of liquid tin between 250 and 1100°c*, Phys. Rev. B **25**, 4248–4251 (1982).

[105]S. A. Reijers, D. Kurilovich, F. Torretti, H. Gelderblom, and O. O. Versolato, *Laser-to-droplet alignment sensitivity relevant for laser-produced plasma sources of extreme ultraviolet light*, J. Appl. Phys. **124**, 013102 (2018).

[106]R. Meijer, *Tailored laser-droplet interaction. for target formation in extreme ultraviolet sources*, Published on 4 October 2021 (2021).

[107]H. K. Schubert, D. J. Engels, M. Kharbedia, H. Gelderblom, and O. O. Versolato, *Observation of discrete concentric surface modulations on free-flying liquid tin sheets*, Phys. Fluids **37**, 094108 (2025).

[108]H. L. França, H. K. Schubert, O. O. Versolato, and M. Jalal, *Laser-induced droplet deformation: curvature inversion explained from instantaneous pressure impulse*, Manuscript submitted to *J. Fluid Mech.*, `10.48550/arXiv.2502.06417` (2025).

Acknowledgements

A special thanks goes to colleagues who significantly contributed to this thesis. **Oscar Versolato** - Although our start was a bit rocky, thank you for placing your trust in me and for continuously revisiting the progress and direction of my thesis. I have learned a lot from you, your guidance gave me the space to grow and motivated me to achieve results that I never would have expected of myself. We shared the blue belt level in Jiu-Jitsu for a while, and I really appreciate that you manage to pursue this alongside everything else. **Wim Ubachs** and **John Sheil** - thank you for enabling me to pursue my PhD; without your initial approval, it would never have happened. **Randy Meijer** - The tall Dutchman I met in the lab, always constructively critical and occasionally a bit stubborn, yet consistently focused on improvement. You quickly became the go-to expert for precise technical challenges, from laser beam alignment and beam profile imaging to DET025A/M photodiodes and Stanford Research DG645 delay generators. I learned a lot from you both in experimental lab work and in Python programming. **Bo Liu** - Thank you for introducing me to collapsing data plots and green shadowgraphy imaging. Your creative approach to data interpretation was a valuable asset in this work. **Dion Engels** - It was an exciting start when we were thrown into the lab with Randy and the OPO. Thank you for your valuable contributions as a Python developer on the vaporization and ray-tracing models. After four years of sharing a workplace, I can confidently say that you have earned the honorary titles of ARCNL's biggest trash talker and the lab's most notorious tin nozzle breaker. **Mikheil Kharbedia** - The fluid guy. Your support has been incredibly valuable. I learned a great deal about fluid dynamics through our work together, and it has become a truly fascinating field for me. Translating theory into measurements and uncovering insights during our experimental campaigns was both exciting and inspiring. **Hugo França** - The programmer I had the pleasure of working and the mastermind behind the curvature project. I truly appreciate your clear communication and your meticulous approach to handling numerical simulations. **Gabriela Piloni Pires** - Thank you for carrying out the Basilisk simulations, which provided valuable insights into ripple formation and became an important part of the Conclusion Chapter of my thesis. **Hanneke Gelderblom** - Thank you for validating our adaptation of the Rayleigh-Taylor instability model for the surface modulation project.

Also, thank you to my colleagues from the EUV source department: **Stan de Lange** - I appreciated our conversations about the most random topics and memes. **Diko Hemminga** - It was great sharing a workplace with you; you are a very knowledgeable guy. **Zoi Bouza** - thanks for always creating a positive and kind environment. **Lucas Poirier** - the French beer enthusiast; very laid back, I enjoyed having you around. **Lars Behnke** - The famous originator of the legendary 'Lars Essential Words (LEWs).' I enjoyed mountain biking with you. **Yahia Mostafa** - fun to share a workplace with; I will always remember our discussions about the perfect weather conditions for ordering pizza. **Javier Hernández** - thanks for your support and humor. **Edcel Salumbides** - the calm and thoughtful lab caveman (and glider pilot); I admire your meticulous way of working and your resistance to using MS Teams. **Lars de Reus** - a hustler from the south of the Netherlands, I enjoyed our conversations during lunch. **James Byers** - I enjoyed bouldering with you. I hope you are enjoying the Jiu-Jitsu journey as well now! **Adam Lassise** - the American movie expert; thanks for the great recommendations. **Jane Babenko** - I appreciate how you always stayed positive despite your difficult circumstances. **Kevin Mongey** - the funny Irish calisthenics pro; hope to catch up in Dublin sometime. **Jan Mathijsen** - the Tischkicker champion; I learned something from you about laser beam alignment. **Xyoisan Danser** - the Amsterdam ion guy and Ronnie's biggest fan; It was fun to share a desk island with you. **Mardou Bijker** - I appreciate having you around. **Klaas Bijlsma** - the proud Frisian. **Luc Assink** - the ion and beer guy from Groningen; I really enjoyed our conversations. **Emiel de Wit** - Groningen car fan with the most impressive animated PowerPoints. **Fleur Veen** - a very sporty person; thank you for your positive attitude. **Jorge Gonzalez Muñoz** - the seasoned Spanish conqueror. **Bowie Brewster** - the goofy chess hustler; I liked having you around. **Surabhi Aggrawal** - I appreciated the joy and cultural curiosity you brought to the team. **Marijn Reitsma** - laid back but also driven to work on one of the most independent topics in the department. A skilled pétanque player. I enjoyed your company. **Felix Kohlmeier** - the dedicated and Tagesschau-informed researcher. **Bas Slotema** - I appreciate your broad range of interests that fueled creative discussions. I especially enjoyed our random debates about the Fietsstraat community. **Mats Brinkman** - the laid-back guy who enjoys a beer and might one day add cigars to the mix.

Also, a special thanks goes to the rest of my ARCNL colleagues who contributed to a positive working environment; for example, **Fengling Zhang** - we started our PhD journeys together, and it was a real pleasure having you around, **Ester Pérez Penco** - I hope you manage some decent pull-ups at some point. **Luka Babic** - the party guy; maybe we will make it to a rave together someday. **Reynolds Dziobek-Garrett** - the American embassy; it's been fun having you around. **Mengqi Du** - I appreciate how you created a positive environment, especially during my early days working with Randy. **Stefan Lehmann**, **Kevin Murzyn**, **Roy van der Linden**, **Pieter van Essen**, **Zhonghui Nie**, **Barsha Bhattacharjee**, **Thomas Nieboer**, **Giona Mainardis**, **Ozan Sahin**, **Thomas Nieboer**, and many others; always great to talk with. Also, thanks to those who participated in PV events or joined me in activities outside of work. I particularly enjoyed the mountain-biking trip in Lage Vuursche with **Lars Behnke**, as well as the paintball afternoon with **Kian Goeloe** (the football pro), **Matthijs Velsink**, **Matthias Gouder**, **Maksym Illienko**, **Augustas Karpavicius** (the paintball pro), **Dennis Kang** (the cold-brew coffee pro), and **Thomas van den Hooven** (the cycling pro), and also playing football in the **ARCeNal** team.

Furthermore, I would like to thank the ARCNL technicians and the AMOLF workshop for their support of my experimental work. The results presented in this thesis were largely made possible thanks to the support of **Laurens van Buuren** - You are the backbone of the EUV Source groups' research efforts. I appreciate our conversations and shared perspectives on Germany and the Netherlands. I also acknowledge **Arend-Jan van Calcar** - the model-flight enthusiast, for his spontaneous help with vacuum-specific issues during the preparation phases of several beamtimes. My thanks also go to the chief mechanical engineer of Dalek 2: **Henk-Jan Boluijt**. Your engineering expertise has been instrumental in enabling many of the technical advances featured in this work. Special thanks to the chief software engineer: **Jorijn Kuster** - Your continuous support and rapid response to requests related to our measurement control software, Sonic Screwdriver, enabled us to have smooth and reliable beamtime operations. I would also like to thank Duncan Verheijde for his support with electronic components and readout systems, and for his insight into the ground loops that interfered with the measurement signals.

Thank you to **Marjan Fretz** for your efficient administrative support, which allowed a smooth continuation of my thesis. Finally, I would like to thank **Joost Frenken** and **Wim van der Zande** for their leadership at ARCNL.

And a big thank you to the entire **Brazilian Jiu-Jitsu Academy (BJJA) team**, who kept me motivated and driven, supported me during tournaments, and helped me stay grounded throughout my PhD. **Remo**, **Kirin**, **Rose**, **Jelle**, **Dion** (bouldering pro in the side hustle), **Luc**, **Sajil**, **Claire**, **Liza**, **Lia**, **Robin**, **Dmitris**, to name a few. I learned a lot on the mats, and I must say that progressing from blue belt to purple belt felt almost as challenging as earning a PhD. In addition, you made Amsterdam feel like home by welcoming each other off the mats and fostering a strong sense of community and friendship. I am truly grateful for that.

A special thanks to my partner **Natalie**. What a journey it has been, traveling with Jiu-Jitsu gym visits always on the schedule, moving in together, and even bringing your cat to the Netherlands. You have been my greatest support throughout, and I am excited to see where our journey takes us next.

I would like to thank my friends and family from my hometown. **Markus** and **Max**, for their fun company and the many great laughs during my visits home. I am also thankful to my parents, **Bernd** and **Andrea**, my grandmother **Irmgard**, and my brothers, **Paul** and **Kurt**, for their support and for the good times together. Thanks also to **Rainer** and **Bettina** for their nice company at gatherings around our self-built pizza oven.